

# Quantum Phase Slips in Granular Aluminum Nanowires

Zur Erlangung des akademischen Grades eines  
DOKTORS DER NATURWISSENSCHAFTEN (Dr. rer. nat.)  
von der KIT-Fakultät für Physik des  
Karlsruher Instituts für Technologie (KIT)

genehmigte  
**Dissertation**  
von

M.Sc. JAN NICOLAS VOSS

Tag der mündlichen Prüfung:	22.07.2022
Referent:	Prof. Dr. Alexey V. Ustinov
Korreferent:	Prof. Dr. Alexander Shnirman



# Contents

<b>1</b>	<b>Introduction</b>	<b>1</b>
<b>2</b>	<b>Theoretical background</b>	<b>5</b>
2.1	General introduction to superconductivity	5
2.2	Ginzburg Landau theory	6
2.3	BCS theory	8
2.4	Flux quantisation	9
2.5	The Josephson effect	10
2.6	Ambeogaokar-Baratoff and Kulik-Omel'yanchuk relations	12
2.7	Kinetic inductance	12
2.8	Aharonov-Bohm and Aharonov-Casher effect	15
2.9	Phase slips	17
2.9.1	Thermally activated phase slips	19
2.9.2	Quantum phase slips	22
2.10	Duality between Josephson junctions and quantum phase slip junctions	25
2.11	Superconducting quantum interference devices	34
2.11.1	The DC SQUID	34
2.11.2	The quantum phase slip interferometer	37
2.12	Design considerations for a quantum phase slip interferometer	45
2.12.1	Circuit schematic	45
2.12.2	Parameters	46
<b>3</b>	<b>Material and fabrication</b>	<b>49</b>
3.1	Granular aluminum	50
3.2	Film deposition	53
3.3	Lithography process	54
<b>4</b>	<b>Experimental methods</b>	<b>59</b>
4.1	Cryogenic setup	59
4.2	Chip layout and general design considerations	63
4.2.1	Single wire circuits	64

4.2.2	Double wire circuits . . . . .	67
<b>5</b>	<b>Intrinsic electromigration (IEM) . . . . .</b>	<b>69</b>
5.1	Modeling a granular aluminum nanowire . . . . .	69
5.2	Concept of IEM . . . . .	71
5.3	Modeling IEM as the formation of microscopic quantum point contacts . . . . .	72
5.4	IEM results . . . . .	74
<b>6</b>	<b>Quantum phase slip experiments with nanowires . . . . .</b>	<b>81</b>
6.1	Single wire experiments . . . . .	81
6.1.1	Reducing the normal state wire resistance with current pulses . . . . .	83
6.1.2	Insulating regime . . . . .	85
6.1.3	Dependence of the Coulomb blockade on the normal state resistance . . . . .	85
6.1.4	Metallic regime . . . . .	88
6.1.5	Superconducting regime . . . . .	89
6.1.6	Dependence of the critical current on the normal state resistance . . . . .	91
6.1.7	Phase diagram . . . . .	92
6.1.8	Temperature dependence of the nanowire resistance below 3 K . . . . .	95
6.1.9	Temperature dependence of the critical voltage . . . . .	98
6.2	Double wire circuit experiments . . . . .	99
6.2.1	Gate dependent modulation of the critical voltage . . . . .	100
6.2.2	Time stability of the Coulomb blockade . . . . .	101
6.2.3	Temperature dependence of the critical voltage . . . . .	102
6.2.4	Resistance dependence of the critical voltage and the gate modulation . . . . .	103
6.2.5	Resistance dependence of the two wire homogeneity . . . . .	105
6.2.6	Homogeneity of the two wire circuit in dependence of the current pulses . . . . .	107
6.2.7	Gate dependent transport transition from insulating to metallic . . . . .	109
6.2.8	Gate dependent transport transition from insulating to superconducting . . . . .	111
6.2.9	Resonator readout of the nanowire interference circuit . . . . .	114
6.2.10	Concluding remarks . . . . .	117
<b>7</b>	<b>Conclusion . . . . .</b>	<b>121</b>

**Bibliography** . . . . . 123

**List of publications** . . . . . 137

**Appendix** . . . . . 139

    A Fabrication parameters . . . . . 139

**Acknowledgements** . . . . . 141



# 1 Introduction

Superconductivity, itself a very fascinating phenomenon, gives rise to a variety of surprising effects: In the superconductive state the direct current resistance and the heat conductance vanish, magnetic fields are expelled and Cooper pairs can coherently tunnel through insulating barriers.

Going from bulk superconductors down to systems with reduced dimensions, new effects arise. In superconducting nanowires where the diameters are of the order of the coherence length, the response to an applied electrical field can be dramatically different: While short wires show the same superconductive behavior as bulk superconductors, long wires may show no electric transport at low applied voltages. This startling behavior seems to be counter-intuitive at first glance, but it can be explained by the strong spatial constriction of the superconducting condensate, which leads to quantized fluctuations of the order parameter. During such a quantum phase slip (QPS) event, the magnitude of the order parameter is suppressed for a short moment in time, allowing the phase to slip by  $2\pi$ . For sufficiently large amplitudes, these QPS can destroy the phase coherence across the wire, and the nature of the electrical response of the wire turns from an inductive into a capacitive one. Thus, in this case, the superconducting state does not lead to its name-giving property [Onn11], but exactly to the opposite, an insulating behavior.

The research on QPS effects in nanowires has already started in the late eighties of the 20th Century with the first experimental observation by N. Giordano [Gio88] and has been an active field of research since then [BLT00; Bez12; Bol+08; Aru+12; Lau+01; Alt+06; Mak+16; AGZ08]. A special stimulus and new direction was generated with the proposed duality between QPS junctions and Josephson junctions [MN06]. The exciting perspective of QPS junctions as a new key element for quantum circuits has triggered a variety of experimental and theoretical work [HN11; Ast+12; HZ12; Gra+18; EN21]. A particularly interesting topic for both, the fundamental understanding of QPS effects and for their utilization in quantum circuits, is the understanding of the superconductor to insulator transition, driven by the QPS rate [SFK20; Moo+15; Mak+16].

One of the major challenges and a limiting factor for the experimental works is the parameter spread of the nanowire properties. For QPS rates in the GHz range, the diameters of the wire must be of the order of the coherence length and the sheet resistance of the material should be high [Moo+15]. Thus, the natural choice are high kinetic inductance materials such as niobium nitride, molybdenum germanium or granular aluminum. In combination with the small diameters, their inner disorder leads to a large spread in the wire parameters, since local variations in the composition will no longer average out. This randomness is in particular problematic for the investigation of wires with large QPS rates where sheet resistances typically are of the order of a few kilo-Ohms and the wire lengths are much greater than the coherence length.

In this thesis, we explore QPS effects in nanowires made from granular aluminum. The material consists of pure crystalline aluminum grains which are embedded into an insulating matrix. The system forms a randomly arranged network of Josephson junctions, defining the properties of the wire. To adjust the normal state resistance of single wires and thereby the QPS rate, we developed a new technique, which utilizes this inner structure and allows to change the resistance of single wires by orders of magnitude.

We use this new degree of freedom to investigate the superconductor to insulator transition for single wires and to study the relationship between the wire resistance and other characteristic properties like Coulomb blockades or critical currents. A special emphasis will be put on the role of the characteristic energies, namely the phase slip energy and the inductive energy [Moo+15]. We address the question whether the different regimes of high and low QPS rates can be energetically separated by means of a phase diagram.

To explore the coherent character of quantum phase slips, in the second part of this work a new type of QPS interferometer has been studied. Such devices are considered to be the dual [HZ12; Gra+18] counterparts to the superconducting quantum interference device (SQUID) for Josephson junctions [Jak+64] which has become one of the most prominent and successful quantum circuits. The influence of several parameters like circuit homogeneity or wire length on the performance of the QPS device has been studied. Apart from the wide range of possible applications like transistors, detectors or the use as tunable QPS junctions, this QPS interferometer provides the opportunity to study the impact of the QPS amplitude on the transport behavior of the nanowires involved.

The thesis is organized as follows: The first chapter contains an introduction into the objective, scope and aim of this work. The main part of this thesis starts with a brief summary of important theoretical principles of superconductivity. Then, a

comprehensive introduction into basic models and concepts for the description of phase slips is given. In the last two sections of chapter two, the operating principle and the design of a quantum phase slip interferometer are discussed. In the third chapter, properties of granular aluminum as a material and the techniques used to fabricate the samples are described. The fourth chapter gives an overview of the cryogenic setup, the measurement methods and the experimental design. The new method developed in the course of this work for the stepwise reduction of the normal state resistance of nanowires made from granular aluminum is discussed in the fifth chapter. In the sixth chapter, the central results of the nanowire experiments are presented. The first section deals with QPS phenomena in single wires. In particular, the relationship between the transport behavior in the superconducting state and the normal state resistance is investigated [Vos+21]. In the second part, the measurements of the double-wire QPS interferometer are presented. Here a special focus is put on the investigation of the superconducting to insulating transition by means of the interference of QPS.



## 2 Theoretical background

### 2.1 General introduction to superconductivity

In this section, a very brief introduction to superconductivity and some of the fundamental concepts relevant for the experimental investigation of this work is given. The models and notations introduced here will be used throughout the following chapters. They are important to understand the origin and key constituents for a systematic investigation of quantum phase slips in superconducting nanowires, the main subject of this work.

With the discovery of superconductivity in 1911, Kamerlingh Onnes has opened a great field for theoretical and experimental work in condensed matter physics. Onnes named the phenomenon after his most significant observation, the sudden and dramatic increase in conductivity below a certain temperature  $T_c$  [Onn11]. Historically, the discovery fell into the time when the first steps towards quantum mechanics were made. The new and abstract concepts, which were needed to understand the macroscopic quantum phenomenon of superconductivity, possibly explain why it took almost fifty years until the first microscopic description of superconductivity was introduced by Bardeen-Cooper and Schrieffer (BCS theory) [BCS57].

The first phenomenological description of superconductivity was already published in 1935 by the London brothers [LL35], shortly after Walther Meissner and Robert Ochsenfeld had discovered perfect diamagnetism in a superconductor [MO33]. For their theory, they simply assumed a certain density  $n_s$  of electrons which can propagate in the superconductor without friction. Doing so, they derived the first London equation, describing the motion of these "superconducting" electrons under the influence of an electrical field:

$$\frac{\partial \mathbf{j}_s}{\partial t} = \frac{e^2 n_s}{m_e} \mathbf{E} \quad (2.1)$$

with current density  $\mathbf{j}_s$ , electron charge  $e$  and electron mass  $m_e$ . The second London equation describing the magnetic field inside a superconductor is [Sch+97]

$$\nabla \times (\nabla \times \mathbf{B}) = -\frac{1}{\lambda_L^2} \mathbf{B} \quad (2.2)$$

With  $\lambda_L = \sqrt{mc^2/4\pi n_s e^2}$  being defined as the London magnetic field penetration depth. Eq. 2.2 can be obtained from Eq. 2.1 by using the Maxwell equations and integrating over time.

## 2.2 Ginzburg Landau theory

Based on the work of Landau on the description of phase transitions by means of an order parameter [Lan37], V. L. Ginzburg and L. D. Landau in 1950 published a phenomenological theory for the description of superconductivity [GL55]. Although the theory does not provide a microscopic explanation for the phenomenon of superconductivity, it does provide a good description of some of the basic properties, such as the critical magnetic field and the penetration depth of the magnetic field close to the transition temperature  $T_c$ . The underlying idea was to use an effective wave function to describe the superconducting electrons, in analogy to the Bose-Einstein condensation, and to use the amplitude as the order parameter  $\Psi(\mathbf{r})$ . As  $\Psi(\mathbf{r})$  describes the additional order in the system, it should vanish above  $T_c$  and be nonzero below  $T_c$ . The natural normalization condition therefore is:  $|\Psi(\mathbf{r})|^2 = n_s$  with  $n_s$  being the superconducting electron density. Consequently, the complex order parameter can be expressed as:

$$\Psi(\mathbf{r}) = \sqrt{n_s} e^{i\phi} \quad (2.3)$$

Assuming a homogeneous superconductor, where  $\Psi(\mathbf{r})$  is constant in space ( $\Psi(\mathbf{r}) \rightarrow \Psi$ ), and there is no magnetic field, the free energy close to  $T_c$ , where  $|\Psi| \rightarrow 0$ , can be constructed as follows:

$$F_s = F_n + \alpha |\Psi|^2 + \frac{\beta}{2} |\Psi|^4 \quad (2.4)$$

Here,  $F_n$  is the free energy in the normal state,  $\alpha$  and  $\beta$  are coefficients that can be derived from the properties of the superconductor. For a state of equilibrium, one can minimize the free energy of the superconductor with respect to the order parameter ( $dF_s/d|\Psi|^2 = 0$ ) and arrives at the solution:

$$|\Psi_0|^2 = -\frac{\alpha}{\beta} \quad (2.5)$$

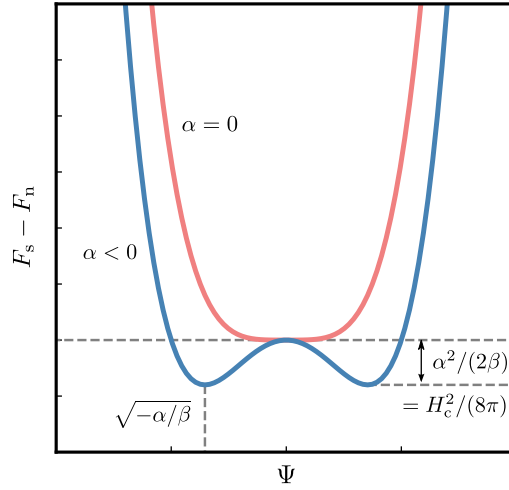


**Figure 2.1:** Free energy for  $\alpha = 0$  and  $\alpha < 0$  as a function of  $|\Psi|$ . The phase transition occurs at  $\alpha = 0$ . For values  $\geq 0$ , the free energy has a single minimum (at  $\Psi = 0$ ), which means that  $n_s = 0$ . For  $\alpha < 0$ , the minima are at  $|\Psi| = \sqrt{-\alpha/\beta}$ . The energy difference between the normal and the superconducting phase is described by the critical magnetic field.

Inserting the result into Eq. 2.4 allows to express the energy difference between the normal and the superconducting state by means of the coefficients  $\alpha$  and  $\beta$ :  $F_n - F_s = \alpha^2/(2\beta)$ . Now one can use the fact that the energy difference is also described by the critical field  $H_c$ :

$$\frac{\alpha^2}{2\beta} = \frac{H_c^2}{8\pi} \quad (2.6)$$

The change of the free energy at the phase transition is shown in Fig. 2.1. From Eq. 2.6, it follows immediately that  $\beta > 0$ . We also know from the temperature dependence that for  $T = T_c$ ,  $|\Psi|^2 = 0$  ( $\alpha = 0$ ) and for  $T < T_c$ ,  $|\Psi|^2 > 0$  ( $\alpha < 0$ ). Hence,

$$\alpha = \alpha'(T - T_c) \quad (\text{with } \alpha' > 0); \quad \beta = \text{const.}, \quad (2.7)$$

which with Eq. 2.6 gives the characteristic scaling  $H_c^2 \propto \alpha^2 \propto (T - T_c)^2$ . If we now go to the more general case of an inhomogeneous superconductor ( $\Psi \rightarrow \Psi(\mathbf{r})$ ) in a magnetic field  $\mathbf{H}_a$ , the Gibbs free energy density can be expressed in the form:

$$G_s = G_n + \alpha|\Psi|^2 + \frac{\beta}{2}|\Psi|^4 + \underbrace{\frac{1}{2m} \left| \left( -i\hbar\nabla - \frac{2e\mathbf{A}}{c} \right) \right|^2}_{(*)} + \underbrace{\frac{1}{8\pi} |\mathbf{H} - \mathbf{H}_a|^2}_{(**)} \quad (2.8)$$

[Cyr73]. Here  $G_n$  is the Gibbs free energy density in the normal state, (\*) accounts for spatial variations of  $\Psi$  where the second part ( $(2e\mathbf{A}/c)$ ) ensures gauge

invariance.  $(\mathbf{H} = \mathbf{H}(\mathbf{r}))$  is the field of the superconductor at point  $\mathbf{r}$ ). The Gibbs energy is then given by the integral over the volume of the superconductor. To derive the two Ginzburg-Landau equations, one has to minimize the Gibbs energy with respect to the order parameter  $\Psi$  and the magnetic vector potential  $\mathbf{A}$ . The first Ginzburg Landau equation is:

$$\alpha\Psi + \beta|\Psi|^2 + \frac{1}{2m} \left( -i\hbar\nabla - \frac{2e\mathbf{A}}{c} \right)^2 \psi = 0 \quad (2.9)$$

and the second equation:

$$\mathbf{j}_s = -\frac{ie\hbar}{2m} [\Psi^*\nabla\Psi - \Psi\nabla\Psi^*] - \frac{e^2}{mc} |\Psi|^2 \mathbf{A} = \frac{c}{4\pi} \nabla \times \mathbf{H} \quad (2.10)$$

Solving these equations allows to analyse the current and magnetic field distribution for different boundary conditions. From a normalization, one can also find the Ginzburg Landau expressions for the coherence length  $\xi_{\text{GL}} = (\hbar^2/(4m|\alpha|))^{1/2}$  and the penetration depth  $\lambda_{\text{GL}} = ((mc^2\beta)/(8\pi e^2|\alpha|))^{1/2}$  (see e.g. [Bez12]).

## 2.3 BCS theory

The first microscopic theory of superconductivity was provided by John Bardeen, Leon Cooper and John Schrieffer and is named BCS theory after its inventors [BCS57]. In the previous sections, we already have seen some phenomenological approaches which were able to cover some of the fundamental observations made for superconductors. However, an understanding of the underlying mechanism, allowing ‘superconducting’ electrons to travel without friction, was missing so far. A first indication that lattice vibrations may be involved in the formation of the superconducting state came with the observation of the isotope effect for mercury by Emanuel Maxwell in 1950 [Sch+97; Max50]. He was the first to observe that the transition temperature depends on the nuclear mass ( $T_c M^\alpha = \text{const.}$  with  $M$  being the mass of the isotope and  $\alpha \sim 0.5$  for most superconductors) [Sch+97]. The key idea of the BCS theory is that the electrons condense into a new lower ground state of paired electrons, the so-called Cooper pairs (named after Leon Cooper). This is possible due to a weak attractive interaction mediated by the phonons and the bosonic nature of the resulting Cooper pairs, having a total momentum and a spin of zero. An important result of the BCS theory is the prediction of an energy gap  $\Delta(T)$  in the quasi-particle energy spectrum. It arises from the energy difference between the Cooper pair bound state and the quasi-particle excitation spectrum. The energy gap is given by:

$$\Delta(T=0) = 1.765 k_B T_c \quad (2.11)$$

with the Boltzmann constant  $k_B$  and the critical temperature  $T_c$ . For temperatures close to  $T_c$ , the BCS gap holds:

$$\Delta(T \rightarrow T_c) = 3.06 k_B T_c \sqrt{1 - T/T_c} \quad (2.12)$$

The energy gap is responsible for the lack of scattering and, therefore, for the lossless current transport. The energy required to break a Cooper pair is at least  $2\Delta$ , which is intuitive since two electrons together form one Cooper pair.

## 2.4 Flux quantisation

One of the unique properties of a superconductor is the flux quantization. It is a consequence of the macroscopic wave function  $\Psi(\mathbf{r}, t)$  (with phase  $\Theta(\mathbf{r}, t)$ ), describing the superconducting condensate. If we consider a superconducting ring, which is cooled in an external magnetic field from  $T > T_c$  to  $T < T_c$ , the magnetic field gets expelled from the inside of the ring by screening currents as soon as  $T_c$  is reached (Meißner-Ochsenfeld effect). Inside the enclosed area, a portion of the magnetic field freezes out and will remain, even after turning off the external magnetic field. If we now consider a closed path around the superconducting loop, the wave function must be single-valued. Therefore, the change of phase needs to be zero or an integer multiple of  $2\pi$  [Tin04]

$$\oint_L \nabla \theta d\mathbf{l} = 2\pi n \quad (2.13)$$

The canonical momentum of a Cooper pair within an applied magnetic field is given by the sum of the kinetic part and the part from the magnetic vector potential  $\mathbf{A}$ :

$$\mathbf{P} = m\mathbf{v} + q\mathbf{A} \quad (2.14)$$

Here,  $q$  is the charge,  $m$  is the mass and  $\mathbf{v}$  is the velocity. Inserting Eq. 2.14 into Eq. 2.13 by using the De Broglie relation  $\mathbf{P} = \hbar\mathbf{k}$  gives:

$$\oint_L \hbar\mathbf{k} = \hbar 2\pi n = \oint_L (m\mathbf{v} + q\mathbf{A}) d\mathbf{l} \quad (2.15)$$

with the velocity  $\mathbf{v} = (\mathbf{j}_s/qn_s)$ . Now one can apply Stoke's theorem to convert the contour integral over  $\mathbf{A}$  into a closed surface integral over the curl of  $\mathbf{A}$ . Consequently, we can write  $\nabla \times \mathbf{A} = \mathbf{B}$ . Thus, Eq. 2.15 can be rewritten as:

$$\hbar 2\pi n = m \oint_L \frac{\mathbf{j}_s}{qn_s} d\mathbf{l} + q \oint\!\!\!\oint_S \mathbf{B} ds \quad (2.16)$$

For a contour far enough away from the surface (distance  $d \gg \lambda_{\text{London}}$ ), the magnetic field can be assumed to be zero. Thus, the supercurrent is zero and the integral over the supercurrent density  $\mathbf{j}_s$  vanishes:

$$\frac{h}{q}n = \frac{h}{2e}n = \oint_S \mathbf{B}d\mathbf{s} = \Phi \quad (2.17)$$

with the flux quantum:

$$\Phi_0 = \frac{h}{2e} \quad (2.18)$$

From Eq. 2.17 we see that the enclosed magnetic flux can only take values that are integer multiples of the magnetic flux quantum.

## 2.5 The Josephson effect

One of the most prominent effects in superconductivity is the Josephson effect, predicted by Brian Josephson in 1962 [Jos62] and verified one year later by Anderson and Rowell [AR63]. In essence, it describes the tunneling of Cooper pairs between two superconductors that are separated by a weak link (e.g. a thin insulating barrier). In the superconducting electrodes, the condensate can be described by means of the Ginzburg Landau approach by macroscopic wave functions  $\Psi_{1,2} = \sqrt{n_{1,2}} \exp(i\Phi_{1,2})$  (see Sec. 2.2). Here  $n_{1,2}$  are the charge carrier densities. In the weak link, the two wave functions will exponentially decay. For sufficiently thin barriers, there can be a finite overlap, leading to a coupling between both functions [Fey82]. Introducing a coupling constant  $k$  and the chemical potential  $E_{1,2}$ , the time dependent Schrödinger equations of the coupled superconductors can be expressed as [BK12]:

$$i\hbar \frac{\partial \Psi_{1,2}}{\partial t} = E_{1,2} \Psi_{1,2} + k \Psi_{2,1} \quad (2.19)$$

Building the time derivative of the order parameter and separating real and imaginary parts leads to:

$$\dot{n}_1 = \frac{2k}{\hbar} \sqrt{n_1 n_2} \sin(\Phi_2 - \Phi_1) ; \dot{n}_2 = -\frac{2k}{\hbar} \sqrt{n_1 n_2} \sin(\Phi_1 - \Phi_2) \quad (2.20)$$

$$\dot{\Phi}_1 = \frac{k}{\hbar} \sqrt{\frac{n_2}{n_1}} \cos(\Phi_2 - \Phi_1) - \frac{eV}{\hbar} ; \dot{\Phi}_2 = \frac{k}{\hbar} \sqrt{\frac{n_1}{n_2}} \cos(\Phi_1 - \Phi_2) + \frac{eV}{\hbar} \quad (2.21)$$

Here, we also have introduced a voltage across the junction  $V$ , which leads to different electrical potentials for the two electrodes ( $\Delta E = 2eV \rightarrow E_{1,2} = \pm eV/\hbar$ ). The phase difference  $\Phi_2 - \Phi_1$  between the two wave functions is defined as the

Josephson phase  $\varphi$ . For simplification, we consider two equal charge carrier densities ( $n_1 = n_2 = n$ ). With this approximation, we arrive at the first Josephson equation, describing the current of Cooper pairs flowing through the junction (DC Josephson effect):

$$I = \frac{2k}{\hbar} n \sin(\varphi) = I_c \sin(\varphi) \quad (2.22)$$

$I_c$  is the critical current of the junction. It depends on the geometry of the junction and characteristic material properties like the energy gap  $\Delta$  and the normal state resistance  $R_n$  of the barrier. From Eq. 2.22, we find that a constant phase difference  $\varphi$  leads to a supercurrent through the junction. The second Josephson equation, describing the AC Josephson effect, can be found by reducing Eq. 2.21:

$$\frac{d\varphi}{dt} = \frac{2eV(t)}{\hbar} = \frac{\Phi_0}{2\pi} V(t) \quad (2.23)$$

From Eq. 2.23 we find that a voltage drop across the junction is linked with a phase change. According to the first Josephson equation (Eq. 2.22), this results in an alternating current (with  $\omega = 2eV/\hbar$ ).

Using the two Josephson equations (Eq. 2.22, 2.23) and Faradays law  $V = -L_j \dot{I}$ , the Josephson inductance  $L_j$  of a junction holds:

$$L_j = -\frac{V}{\dot{I}} = \frac{\hbar}{2eI_c \cos(\varphi)} \quad (2.24)$$

Here we see a remarkable property of a Josephson junction: It has a nonlinear inductance that depends on the Josephson phase  $\varphi$ . This is what makes it a suitable element for applications like qubits.

For a Josephson junction that carries a supercurrent, the stored energy can be calculated from the power, defined by the first and second Josephson equation (Eq. 2.22, 2.23):

$$E(\Phi) = \int_0^t IV dt = \int_0^t \frac{\Phi_0}{2\pi} I_c \frac{d\varphi}{dt} dt = \frac{\Phi_0 I_c}{2\pi} (1 - \cos(\varphi)) \quad (2.25)$$

where  $E_j = \Phi_0 I_c / 2\pi$  can be identified as the characteristic Josephson energy [BP82].

## 2.6 Ambeogaokar-Baratoff and Kulik-Omel'yanchuk relations

In the previous derivation of the Josephson effect, we have not cared much about the prefactor in the first Josephson equation (Eq.2.22), which was identified to be the critical current of the junction. Naturally, the critical current of a certain junction will highly depend on various parameters, such as geometry, material, transport channels, and so on. Shortly after the discovery of the Josephson effect, Vinay Ambegaokar and Alexis Baratoff used thermodynamic Greens functions to recalculate Josephson's results and found a general relation between the normal state resistance  $R_n$  and the critical current  $I_c$  of the junction [AB63a; AB63b]. Their calculation assumes S-I-S (superconductor-insulator-superconductor) junctions and the same BCS gap for both superconducting electrodes. The resulting relation reads

$$I_c = \frac{\pi \Delta(T)}{2eR_n} \tanh\left(\frac{\Delta(T)}{2k_B T}\right) \quad (2.26)$$

with the BCS energy gap  $\Delta(T)$ , the Boltzmann constant  $k_B$  and the electron charge  $e$ . For temperatures close to  $T = 0$  we can approximate  $I_c \approx (\pi \Delta(T = 0))/(2eR_n)$  ( $\tanh(x) \approx 1$ ).

In 1975, Kulik and Omelyanchuk proposed a model to describe the critical current for short weak links in the dirty limit (length of the constriction  $\gg$  mean free path) as a function of  $R_n$ . Short here means in relation to the coherence length  $\zeta$  of the superconductor  $L_{wl} < \zeta$ . For  $T \rightarrow 0$ , the average critical current can be expressed as [GKI04]:

$$I_c \approx 1.32 \frac{\pi \Delta(T = 0)}{2eR_n} \quad (2.27)$$

Except for the prefactor, we have the same result as from Ambeogaokar-Baratoff relation. Average critical current means that, in general,  $I_c$  depends on the phase difference across the weak link, and therefore one would need to maximize the full expression from Ref. [GKI04] with respect to the phase to get a more exact result.

## 2.7 Kinetic inductance

A very special and important property of superconductors is their possible high kinetic inductance. Every electrical conductor, whether normal or superconducting, has a geometric and a kinetic inductance. The geometric inductance  $L_g$  can be defined by the energy stored in the magnetic field of the conductor. The kinetic

inductance  $L_k$ , on the other hand, is caused by the inertia of the charge carriers and describes their kinetic energy. For normal conductors, the contribution of kinetic inductance usually is very small and can be neglected, except for very high frequencies [Sch+97]. However, for thin film superconductors, this can be extremely different. We also will see that, in contrast to the geometric inductance, the kinetic inductance depends on the microscopic properties of the material.

For temperatures close to  $T_c$  a simple expression for  $L_k$  can be derived from Ginzburg Landau theory. The kinetic energy of a superconductor with volume  $V = (d \cdot l \cdot w)$  can be expressed by the total kinetic energy of the Cooper pairs:

$$F_k = \int n_s \frac{mv^2}{2} dV = \frac{1}{2} mv^2 n_s (dlw) = \frac{1}{2} L_k I_s^2 \quad (2.28)$$

where  $n_s$  is the Cooper pair density,  $m$  is the mass,  $v$  is the velocity and  $I_s$  is the supercurrent, flowing in  $l$  direction of the superconductor. Using Eq. 2.28 and rewriting the supercurrent as  $I_s = n_s(dw)2ev$  (with Cooper pair charge  $2e$  and cross section area  $dw$ ), the kinetic inductance is:

$$L_k = \frac{ml}{dw2n_s^2} \quad (2.29)$$

For temperatures close to  $T_c$  one can now use the Ginzburg Landau expression for the temperature dependent current carrier density  $n_s(T) = n_s(0)(1 - T/T_c)^{1/2}$  to write Eq. 2.29 in the form:

$$L_k(T) = \frac{ml}{dw2e^2} \frac{1}{n_s(0)(1 - T/T_c)} \quad (2.30)$$

with the London penetration depth  $\lambda_L(T) = \sqrt{m/\mu_0 n_s(T)2e^2}$ , the kinetic inductance can be written as:

$$L_k(T) = \frac{\mu_0 \lambda_L^2(T)l}{wd} = N_{\square} \frac{\mu_0 \lambda_L^2(T)}{d} \quad (2.31)$$

Here,  $N_{\square}$  is the number of squares over a length  $l$ . Alternatively to the temperature dependence introduced in Eq. 2.30, one can also use an empirical formula for the entire temperature range, scaling with  $(1 - T/T_c)^{1/4}$  instead of  $(1 - T/T_c)^{1/2}$  [Sch+97].

For temperatures close to  $T = 0$ , a direct relation between the kinetic inductance and the normal state resistance of a wire can be derived from the electrical conductivity. The response of a superconductor to an alternating electrical field (with frequency  $\omega$ ) can be expressed with the complex conductivity and the Drude model [Tin04]:

$$\mathbf{j} = (\sigma_{1,i} - i\sigma_{2,i}) \mathbf{E} = \left( \frac{n_i e^2 \tau_i}{m(1 + \omega^2 \tau_i^2)} - i\omega \frac{n_i e^2 \tau_i^2}{m(1 + \omega^2 \tau_i^2)} \right) \mathbf{E}, \quad (2.32)$$

where  $m$  is the mass,  $e$  is the electron charge,  $n_i$  is the density of charge carriers and  $\tau$  is the mean time between collisions. The index  $i$  stems from the two-fluid model and accounts for the fact that a current can be either carried by Cooper pairs ( $i = s$ ) or quasiparticles ( $i = n$ ). For the superconducting part ( $i = s$ ), the time between collisions of charge carriers goes to infinity. Therefore the imaginary part is dominated by superconducting charge carriers. For frequencies  $\omega > 0$ , the real part, which accounts for dissipation, is dominated by the quasiparticle contribution ( $i = n$ ). Therefore, the conductivity can be expressed as  $\sigma(\omega) = \sigma_{1,n} - i\sigma_{2,s}$  with ( $\sigma_{2,s} \gg \sigma_{1,n}$ ). The impedance of a thin film superconductor with thickness  $d$  strongly depends on the kinetic inductance and can be expressed as [Tin04; Mau18]:

$$Z = \frac{1}{(\sigma_{1,n} - i\sigma_{2,s})d} \simeq \frac{\sigma_{1,n} + i\sigma_{2,s}}{d\sigma_{2,s}^2} = R + i\omega L_k \quad (2.33)$$

From the separation into an imaginary and a real part, we can identify  $R = \sigma_{1,n}/(d\sigma_{2,s}^2)$  and  $L_k = 1/(d\omega\sigma_{2,s})$ . In the low frequency limit ( $\hbar\omega \ll k_B T$ ) and for  $T \ll T_c$ , the relation between the normal state conductivity  $\sigma_n$  and the complex conductivity of a superconductor can be expressed by the Mattis-Bardeen formula [MB58]

$$\frac{\sigma_{2,s}}{\sigma_n} = \frac{\pi \Delta(T)}{\hbar\omega} \tanh\left(\frac{\Delta(T)}{2k_B T}\right) \quad (2.34)$$

where  $\Delta(T)$  is the superconducting energy gap. Inserting the resulting expression for  $\sigma_{2,s}$  into the kinetic inductance gives:

$$L_k = \frac{1}{d\omega\sigma_{2,s}} = \frac{\hbar}{d\pi \Delta(T) \tanh\left(\frac{\Delta(T)}{2k_B T}\right) \sigma_n} \quad (2.35)$$

Now one can use the definition for the normal state conductivity  $\sigma_n^{-1} = \rho = R_n A/l = R_\square d$ , with the normal state resistance  $R_n$  of a specimen with a cross section of  $A$  ( $d\omega$ ) and a length of  $l$ . For temperatures close to  $T = 0$  we can use the BCS energy gap  $\Delta(T = 0) = 1.76 k_B T_c$  and approximate  $\tanh(\Delta(T)/(2k_B T)) \approx 1$ . Thus, Eq. 2.35 takes the form

$$L_k = \frac{\hbar R_\square}{1.76 \pi k_B T_c} = 0.18 \frac{\hbar R_\square}{k_B T_c} \quad (2.36)$$

From Eq. 2.36 we see that the kinetic inductance can be directly controlled by the sheet resistance of the film. In our experiments, we use granular aluminum, which allows for resistances up to a few kilo-Ohms, leading to kinetic inductances of a few nH per square.

## 2.8 Aharonov-Bohm and Aharonov-Casher effect

The Aharonov-Bohm effect (AB) is named after the discoverers Yakir Aharonov and David Bohm [AB59]. It is a phenomenon in quantum mechanics and describes the influence of a magnetic vector potential on the phase of the wave function of a charged particle when traveling through the field. The effect is even present in the case that the magnetic field and the electric field at the trajectory of the charged particle are zero. Thus, the AB effect simply describes the coupling between the complex phase of the wave function and the vector potential. For example, let's assume a solenoid in the middle and electrons passing on both sides, as illustrated in Fig. 2.2. Even if the magnetic field would be perfectly shielded, the accumulated phase shift would lead to interference between the particles with wave functions  $\Psi_{1,2} = \Psi_{1,2}^0 \exp(-i\varphi_{1,2})$ , depending on the relative phase shift [AB59]:

$$\Delta\varphi = \varphi_1 - \varphi_2 = \frac{q}{\hbar} \left( \int_{C_1} \mathbf{A} d\mathbf{r} - \int_{C_2} \mathbf{A} d\mathbf{r} \right) \quad (2.37)$$

$$= \frac{q}{\hbar} \oint \mathbf{A} d\mathbf{r} = q \int \mathbf{B} d\mathbf{s} = q\Phi_B \quad (2.38)$$

Here, the indices 1,2 are corresponding to the different trajectories/sides of the solenoid,  $q$  is the charge of the particle,  $C_{1,2}$  are the contours along the paths,  $\mathbf{A}$  is the vector potential,  $\mathbf{B}$  is the magnetic field of the solenoid and  $\Phi_B$  is the magnetic flux enclosed between the two different trajectories. Consequently, the probability of the superposition function of  $\Psi = \Psi_1 + \Psi_2$  behind the solenoid will periodically depend on the enclosed magnetic field:

$$P(\Psi) = |\Psi|^2 = |\Psi_1^0|^2 + |\Psi_2^0|^2 + 2\Psi_1^0\Psi_2^0 \cos(\Delta\varphi) \quad (2.39)$$

Almost thirty years after the proposal of the Aharonov-Bohm effect, Yakir Aharonov and Aharon Casher published a work in which they derived the effective Lagrangian, describing the interaction between a neutral particle with a magnetic momentum  $\mu$  and a charged particle with charge  $q$  and showed that the neutral particle will exhibit an effect dual to the AB effect [AC84]. The non-relativistic Lagrangian can be expressed in the form:

$$L = \frac{1}{2}m\mathbf{v}^2 + \frac{1}{2}M\mathbf{V}^2 + q\mathbf{A}(\mathbf{r} - \mathbf{R})(\mathbf{v} - \mathbf{V}) \quad (2.40)$$

$M/m$ ,  $\mathbf{R}/\mathbf{r}$ ,  $\mathbf{V}/\mathbf{v}$  denote the mass, position and velocity of the neutral particle and the particle with charge  $q$ , respectively. As  $L$  is invariant under interchanging of the position and velocity of the particles, it is the same whether the neutral

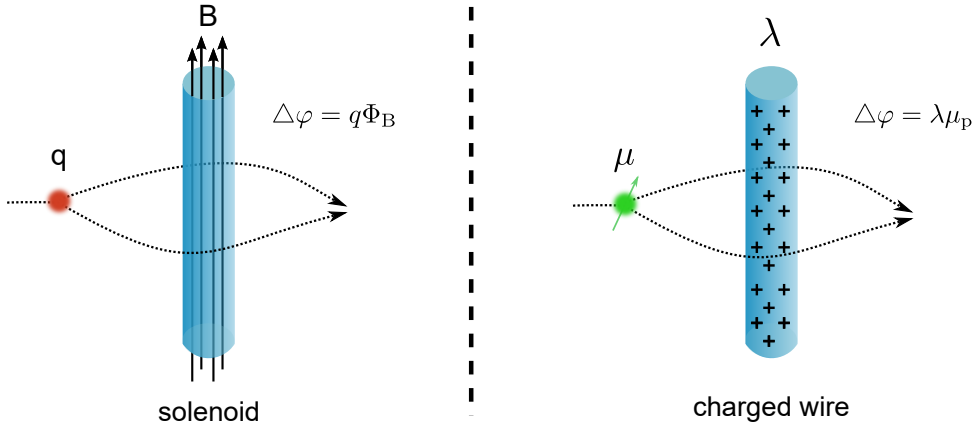


**Figure 2.2:** Illustration of the Aharonov-Bohm effect (AB, left) and the Aharonov-Casher effect (AC, right). For the former, the quantum charged particles collect a relative phase shift due to the encircled magnetic flux. This is still true if the magnetic field at the wave packets is zero since the AB effect describes the coupling of the phase to the vector potential. For the dual AC effect, the interferometer encloses, instead of magnetic flux, a charged wire (with charge per unit length  $\lambda$ ). Here quantum particles with magnetic moment  $\mu$  accumulate a relative phase that depends on the encircled charge ( $\lambda$ ).

particle interacts with the charged particle or vice versa. This means that a particle with a magnetic moment, when traveling through the field of an electric charge, will collect a phase, just dual to the previously discussed AB effect. If we now assume the dual case to the previously discussed situation, where two charged particles were traveling around a solenoid, we may now imagine two particles with magnetic moment  $\mu$  moving around a charged line (or a narrow cylinder). This case is illustrated in the right panel of Fig. 2.2. For the Aharonov-Casher effect, the accumulated phase difference is given by

$$\Delta\varphi = \frac{1}{\hbar} \oint (\mathbf{E} \times \boldsymbol{\mu}) d\mathbf{R} = \frac{q}{\hbar} \oint \mathbf{A}(\mathbf{r} - \mathbf{R}) d\mathbf{R} = \lambda\mu_p \quad (2.41)$$

[AC84]. Here  $\mu_p$  is the projection of the magnetic moment on the charge cylinder axis.  $\lambda$  is the charge per unit length of the line. If we compare this result with the AB phase in Eq. 2.37, we find the exact dual and consequently reach the conclusion that the interference between two particles with magnetic moment  $\mu$  can be controlled by the charge of the area enclosed by their paths.

## 2.9 Phase slips

Along with the advancements in technology during the last decades, it has become possible to define structures in the nanometer range. This is in particular interesting for the investigation of superconductivity as it allows to probe the effect of extreme spacial restrictions on different properties of superconductors. The dimensionality of a superconductor can be defined with respect to the coherence length, which is a measure of the size of a Cooper pair and thus the smallest meaningful unit. Reducing the dimension of a superconductor by shrinking the diameter to the order of the coherence length  $\xi$ , the system may be regarded as one-dimensional. Therefore, fluctuation effects become more relevant. Theoretically, the question of whether superconductivity can exist at all in such systems was already addressed in an early work by Hohenberg from 1966 [Hoh67]. He pointed out that generally the concepts applied involving long-range order break down when going from 3D to 2D or even to 1D systems. However, his studies didn't allow for predictions about a possible phase transition or physical effects. In the same year, William A. Little predicted that thermodynamic fluctuations of the order parameter in thin wires, close to  $T_c$ , can lead to a broadened phase transition at  $T_c$  and that the dissipation accompanying the fluctuations can cause the decay of a persistent current in ring-shaped conductors [Lit67]. In the framework of these studies, he introduced the concept of phase slips based on the Ginzburg-Landau model. Below the critical temperature, the superconducting condensate of a quasi one dimensional superconductor can be described by the complex order parameter  $\Psi(x) = |\Phi(x)|e^{i\phi(x)}$ , with the real amplitude  $|\Phi(x)|$  and the phase factor  $e^{i\phi(x)}$ . Here,  $x$  describes the wire axis. The dependency along the cross section is neglected, assuming that the diameters are of the order of  $\xi$ . In order to be single-valued and continuous, the order parameter describes a helix along the wire axis in the complex plane. Each winding has a phase of  $2\pi$ , and the total number of windings depends on the supercurrent in the wire (see Fig. 2.3). The phase of the order parameter is not uniquely defined. Therefore, adding or subtracting multiple integers of  $2\pi$  does not change the value of the order parameter.

Within a phase slip event, the order parameter gets suppressed at a certain point of the wire within a coherence length and for a time period  $\sim \hbar/\Delta$  ( $\sim 10^{-12}$  s). As illustrated in Fig. 2.3 with Argand diagrams, during this event, the number of phase windings along the wire axis can change. According to the second Josephson equation  $\dot{\phi} = 2\pi/\Phi_0 V$ , the loss of phase causes a voltage drop. Consequently, such phase slips can lead to a non-vanishing resistance, even well below  $T_c$ . Generally, without a current bias, the probability of adding or removing a phase winding is equal, and the overall voltage is zero. For a bias greater than zero, the potential

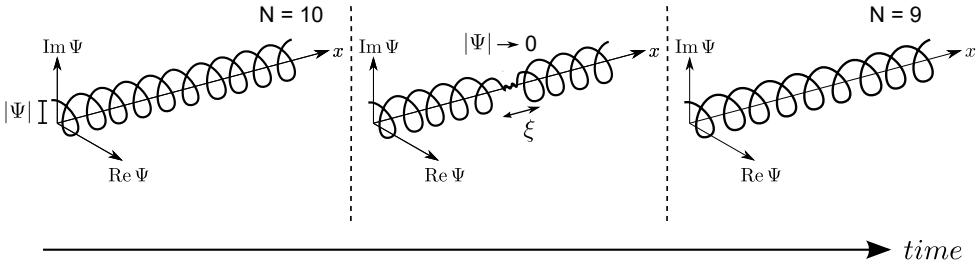


**Figure 2.3:** Illustration of a phase slip: For a thin (diameters  $d \sim \xi$ ) supercurrent carrying wire, the order parameter describes a helix along the wire axis in the complex plane (steady-state). Before the phase slip takes place (left panel), the total number of phase windings is 10. Once a phase slip occurs, for a short moment in time ( $\sim \hbar/\Delta$ ), the modulus of the superconducting order parameter gets suppressed (middle). After it is restored to its initial value, the number of phase windings has changed.

gets tilted, and adding  $2\pi$  becomes more likely than subtracting  $2\pi$ . The rate of these phase slips highly depends on the exact geometry of the wire and on the temperature. So far, the appearance of phase slips was motivated by thermal fluctuations close to  $T_c$ . Thus, approaching  $T = 0$  K, these thermally activated phase slips (TAPS) are highly suppressed, and no measurable resistance should be expected. However, already in 1988, Giordano and co-workers observed that thin wires can exhibit a non-vanishing resistance even well below  $T_c$  [Gio88]. Fig. 2.4 shows the resistance versus temperature dependence they received from their measurements. One can clearly identify two branches (marked with red and blue). For temperatures close to  $T_c$ , the thermal energy is high ( $k_B T \approx I\Phi_0$ ). Therefore, the potential barrier for a change of the phase of the superconducting order parameter by  $2\pi$  can be overcome by thermal activation. This observation was in good agreement with the phenomenon of thermally activated phase slips (TAPS), as they explain the non-vanishing resistance close to  $T_c$  and the exponential decay of  $R$  with  $1/T$  [LA67; MH70]. The second branch, however, was somehow surprising and needed a different explanation. As the thermal energy in this region is too small for TAPS, Giordano attributed the resistance to quantum-mechanical tunneling of the order parameter through the free-energy barrier (see Fig 2.4, right panel). These phase slips are therefore called quantum phase slips (QPS). In the course of time, Giordanos results were confirmed in many experiments on very narrow nanowires [BLT00; Lau+01; Zgi+05; Alt+06; Gio94; Web+13], and quite a number of theories were developed to describe QPS and the consequences for the electrical properties of such a wire [Gio94; GZ01; Zai+97; AGZ08; MN06]. In the following sections, we will discuss some commonly used concepts and models which are used to describe the rate of TAPS and QPS and which will be compared with our experimental results.

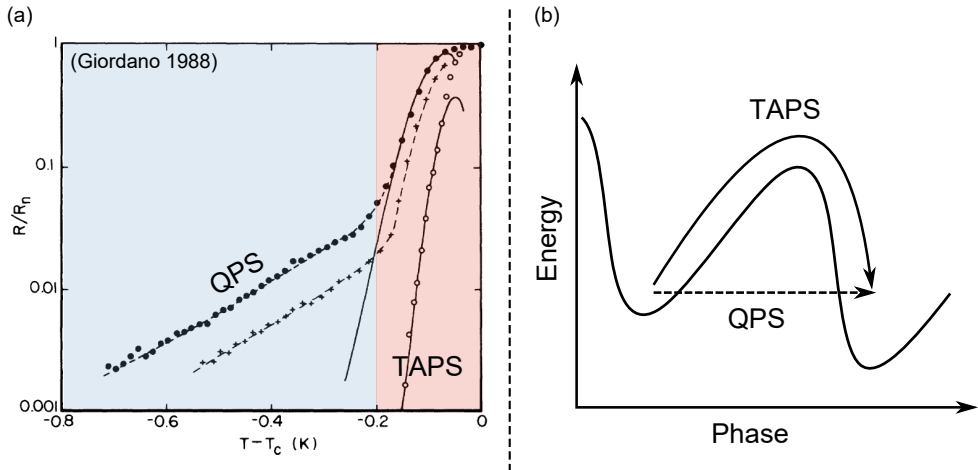


**Figure 2.4:** (a) First evidence of quantum phase slips (QPS), Giordano 1988 [Gio88]: The graph shows the normalized resistance vs. the temperature difference to  $T_c$  for three In wires with different lengths and diameters. For two of the wires, there is a non-vanishing resistance even well below the critical temperature, which can be attributed to quantum phase slips. (b) Illustration of the processes describing thermally activated phase slips (TAPS) and quantum phase slips (QPS). For the former, the energy barrier is overcome by thermal activation. In the case of QPS, the phase tunnels through the barrier.

## 2.9.1 Thermally activated phase slips

First, the regime close to  $T_c$ , where thermal energy in the system is high and thermally activated phase slips are dominating, will be discussed. As mentioned before, the concept of phase slips was introduced by William Little in 1967 [Lit67]. As part of his work, he also developed a first, very simple phenomenological theory to describe the resistance caused by thermally activated phase slips. This model is known as Little's fit and is based on the following assumptions: For the instant in which a phase slip happens, the order parameter is suppressed for a short moment in time, and the wire is in a normal conductive state in this region of length  $x_{\xi}$ . Since the time span for an event is much shorter than the time scales in DC measurements, only the average value is measured. Thus,  $R_{\text{TAPS}}(T)$  can be described by purely statistical considerations as  $R_{\text{TAPS}}(T) = P_n R_n$ , where  $P_n$  is the probability for a phase slip event and  $R_n$  is the normal state resistance of the wire. For the time when no phase slip occurs, the resistance is assumed to be zero. The probability  $P_n$  can be described by the law of Arrhenius as  $P_n = \exp(-\Delta F/k_B T)$ .

Here  $\Delta F$  is the minimum energy required for a phase slip and  $k_B$  is the Boltzmann constant. Thus, one obtains:

$$R_{\text{LP}}(T) = R_n \exp\left(\frac{-\Delta F}{k_B T}\right) \quad (2.42)$$

The model is generally applicable over a wide temperature range as the Arrhenius law is also valid for the lowest temperatures (in contrast to the LAHM model discussed below). However, there are also some weaknesses due to its simplicity. For example, no interactions between TAPS (e.g. by a modification of the potential barrier) are considered, which in particular becomes problematic when the temperature is close to  $T_c$  where the rate of TAPS is high. Also, other contributing factors to the conductance, like quasiparticles, are ignored.

A more sophisticated approach to calculate  $R_{\text{TAPS}}$  is by making use of the fact that each phase slip is accompanied by (at least) a  $2\pi$  phase change and to therefore use the Gor'kov phase evolution equation  $\hbar \frac{d\phi}{dt} = 2eV$  to calculate the resulting voltage, which then can be translated into a resistance. Langer, Ambegaokar [LA67], McCumber and Halperin [MH70] have further developed Little's model and provided the first quantitative description of thermally activated phase slips, which is named after its inventors LAHM theory. Based on the Ginzburg Landau equation, Langer and Ambegaokar calculated the lowest free energy barrier between two uniform solutions with different numbers of phase turns for temperatures close to  $T_c$ :

$$\Delta F = \frac{\sqrt{2}}{3} (H_c(T)^2 / \pi) A \xi(T) = \frac{\sqrt{2} A \xi_0 H_c(0)^2}{3\pi} \left(1 - \frac{T}{T_c}\right)^{3/2} \quad (2.43)$$

with the critical field  $H_c$ , the cross section area of the wire  $A$  and the coherence length  $\xi_0$ . In essence, Eq. 2.43 is the volume at which the wire becomes normally conductive times the condensation energy density. Consequently, the needed activation energy scales with the wire cross section, which means that for smaller diameters, the probability of TAPS will increase. For zero supercurrent  $I_s = 0$ , the probability of adding or subtracting  $2\pi$  phase is equal and therefore also the rates  $\Gamma_+(T) = \Gamma_-(T) = \Gamma(T)$  are equal. The rate itself can be expressed as the product of an attempt frequency  $\Omega(T)$  and the probability function:

$$\Gamma(T) = \Omega(T) \exp\left(-\frac{\Delta F(T)}{k_B T}\right) \quad (2.44)$$

An expression for the attempt frequency was derived by McCumber and Halperin, using the time dependent Ginzburg Landau equation [MH70]:

$$\Omega(T) = \frac{l(T)\sqrt{3}}{2\pi^{3/2}\tau_r} \sqrt{\frac{\Delta F(T)}{k_B T}} \quad (2.45)$$

with  $l(T)$  being the length of the wire in units of the coherence length ( $l = L/\xi(T)$ ) and  $\tau_r$  being the relaxation time of the order parameter ( $\tau_r = \pi\hbar/8k_B(T - T_c)$ ). Because  $\tau_r$  approaches zero for  $T \rightarrow T_c$  a weakness of the LAHM theory becomes evident. It predicts that for  $T \rightarrow T_c$ , the rate of thermally activated phase slips is suppressed, which does not make sense as the thermal energy is high at this point. This mismatch can be understood since the origin of this expression lies in the time dependent Ginzburg Landau theory, which is only valid in a small temperature range below  $T_c$ .

For finite supercurrents, the energy barrier  $\Delta F$  for  $+2\pi$  and  $-2\pi$  phase change differs by  $(\pi\hbar I_s)/(2e)$  [AD64]. In the picture of a tilted washboard potential, this can be interpreted as a reduced probability to role upwards. The resulting net rate is:

$$\Gamma_{\pm}(T) = \Omega(T) \exp\left(-\frac{\Delta F(T)}{k_B T}\right) \left[ \exp\left(-\frac{\pi\hbar I_s}{2ek_B T}\right) - \exp\left(\frac{\pi\hbar I_s}{2ek_B T}\right) \right] \quad (2.46)$$

Rewriting the exponential functions inside the brackets as a hyperbolic sine function and performing a Taylor approximation for small currents ( $\sinh(x) \approx x$ ), one receives

$$\Gamma_{\pm}(T) = -\Omega(T) \exp\left(-\frac{\Delta F(T)}{k_B T}\right) \left(\frac{\pi\hbar I_s}{ek_B T}\right). \quad (2.47)$$

For the steady state, where the phase windings added by the bias in average are equal to the loss of phase by TAPS, the voltage is given by  $V = -(\pi/e)\hbar\Gamma_{\pm}$ . Combing this condition with Ohm's law ( $R = V/I_s$ ) allows to write the TAPS resistance as follows:

$$R_{\text{TAPS}} = R_q \frac{\hbar\Gamma(T)}{k_B T} = \sqrt{\frac{3}{\pi}} \frac{\hbar^2 \pi}{2\tau_r e^2 k_B T} l(T) \sqrt{\frac{\Delta F}{k_B T}} \exp\left(-\frac{\Delta F}{k_B T}\right) \quad (2.48)$$

Here, the attempt frequency from Eq. 2.45 was inserted.  $R_q$  is the quantum resistance ( $h/(4e^2)$ ). Interestingly, this result does not (directly) depend on the normal state resistance of the wire. Due to the approximation done during derivation, the result is only valid for  $|I_s| < |e|k_B T/(\pi\hbar)$ .

Almost thirty years later, the problem was reanalyzed by Golubev and Zaikin (GZ) ([GZ99]). To do so, they used an effective action approach to calculate the TAPS rate and received a prefactor that exceeded the one found by McCumber and Halperin (see Eq. 2.45) by a factor  $\sim (1 - T/T_c)^{-1}$ . For small currents ( $I_s \ll I_c$ ), the resulting TAPS resistance from GZ theory reads:

$$R_{\text{TAPS,GZ}} = 17 \frac{T_c}{T} R_q l(T) \sqrt{\frac{\Delta F}{k_B T}} \exp\left(-\frac{\Delta F}{k_B T}\right) \quad (2.49)$$

In the full GZ expression of the attempt frequency a current dependent function  $k(I_s)$  (values between 5.53 and 8.74) and a constant  $a = T_{\text{QPS}}/T_c$ , where  $T_{\text{QPS}}$  is the temperature below which QPS are dominating, are included. However, here it is assumed that  $a \approx 1/2$  and  $k(I_s) \approx 5.53$ . From an experimental point of view, the prefactor plays a minor role when comparing theory to measurements. Thus, small differences can be neglected. More importantly, the attempt frequency and with this also  $R_{\text{TAPS,GZ}}$  does not converge to zero for  $T \rightarrow T_c$ , which is more reasonable when comparing it with the LAHM model.

## 2.9.2 Quantum phase slips

Apart from thermally activated phase slips, in which the potential barrier for a phase slip is overcome by thermal activation, it is also possible that the phase tunnels through the barrier. These phase fluctuations have their origin in the quantum nature of charge and phase. In the quantum regime phase and charge are canonically conjugated variables with the associated quantum operators  $\hat{\Phi}$  and  $\hat{q}$ , obeying the commutation relation  $[\hat{q}, \hat{\Phi}] = -i$ . As a consequence, every charge localization in the wire leads to fluctuations of the phase. In comparison to the TAPS, the quantum phase slips (QPS) do not freeze out for  $T \rightarrow 0$  and can cause a non-vanishing resistance or even a Coulomb blockade well below  $T_c$ .

Besides his experimental results (Fig. 2.4), Giordano also worked out a first phenomenological description for the QPS rate. It is based on the analogy to the well-developed theory of macroscopic quantum tunneling (MQT) in Josephson junctions [Was+85]. For the latter, the tunneling rate can be expressed as:

$$\Gamma_{\text{MQT}} = \Omega \exp(-S/\hbar) \quad (2.50)$$

with the quantum action  $S \propto \Delta U/E_z z^J$ , describing the ratio between the potential barrier and the zero point energy of the junction. The zero point energy of the junction is determined by the plasma frequency  $E_z^J = \hbar\omega_p$ . To map the QPS problem onto the MQT rate, one needs to find the analog for the zero point energy. Giordano's approach was based on the LAHM theory and assumes that the rate depends on the characteristic time of the tunneling process  $\tau$  instead of the thermal energy  $k_B T$ . Therefore, he used the TDGL relaxation time  $\tau_r$  as a time scale characterizing the tunneling process and to define the zero point energy for the QPS wire:

$$E_z = \hbar(1/\tau_r) = 8k_B(T_c - T)/\pi. \quad (2.51)$$

Taking into account that the energy barrier for a phase slip is  $\Delta F$ , the rate can be expressed analog to the MQT rate (Eq. 2.50) as:

$$\Gamma_{\text{QPS}} = \Omega_{\text{QPS}} \exp\left(\beta \frac{\Delta F}{\hbar(1/\tau_r)}\right). \quad (2.52)$$

Here,  $\beta$  is introduced as a fitting parameter. For the attempt frequency  $\Omega_{\text{QPS}}$ , Giordano used the expression from McCumber and Halperin (Eq. 2.45) but replaced the thermal energy  $k_B T$  by the zero point energy  $E_z$ . Thus, Eq. 2.52 becomes:

$$\Gamma_{\text{QPS}} = \frac{l(T)\sqrt{3}}{2\pi^{3/2}} \sqrt{\frac{\Delta F(T)}{\hbar\tau_r}} \exp\left(\alpha \frac{\Delta F}{\hbar(1/\tau_r)}\right). \quad (2.53)$$

For small currents  $|I_s| < |e|E_z/(\pi\hbar)$ , the QPS resistance can be derived analog to the one for TAPS (see Sec. 2.9.1):

$$R_{\text{QPS}} = \alpha R_q l(T) \sqrt{\frac{\Delta F}{\hbar(1/\tau_r)}} \exp\left(-\beta \frac{\Delta F}{\hbar(1/\tau_r)}\right) \quad (2.54)$$

with  $\alpha$  being a second fitting parameter to account for the uncertainty of the attempt frequency. The potential barrier can be assumed to be the same as for TAPS (Eq. 2.43). With respect to the measurements performed in the framework of the present work, where we study gradual changes in the normal state resistance and their effect on the transport behavior of the wire, it is more convenient to express  $\Delta F$  as a function of the wires normal state resistance  $R_n$ . Following Ref. [Bez12], for low temperatures  $T \ll T_c$  equation 2.43 can be rewritten in the form:

$$\Delta F(T) = a 0.83 \frac{R_q L}{R_n \xi} k_B T_c \left(1 - \frac{T^2}{T_c^2}\right)^{3/2}. \quad (2.55)$$

with the fitting parameter  $a$ . To obtain this result, expressions from Ginzburg Landau theory for  $H_c$  and  $I_c$  were used and combined with BCS expressions for the penetration depth and coherence length at zero temperature.

The first macroscopic theory of quantum phase slips was developed by Zaikin and Golubev [Zai+97]. In their work, they stressed that the model from Giordano underestimates the actual phase slip rate by orders of magnitude [Gio94] and therefore is not in agreement with experimental results. In particular, it is pointed out that the expression used for the QPS action  $S_{\text{QPS}}$  ( $\Delta F/E_z$ ) is approximately given by the number of transverse channels ( $N_{\text{ch}} \sim k_F^2 A$ ) which typically has values between hundred and thousand, assuming diameters in the range of twenty nanometers. Thus, the QPS rate  $\Gamma_{\text{QPS}} \propto \exp(-S_{\text{QPS}})$  becomes extremely small. Also, dissipation, caused by the normal conducting core, field effects, and the

non-applicability of the time dependent Ginzburg Landau model for temperatures far below  $T_c$  are not taken into account [Zai+97; GZ01].

As a starting point for their model, Zaikin and Golubev used an effective action approach for BCS superconductors and assumed that in most cases, the mean free path of the nanowire is very small and therefore falling into the dirty limit ( $l^m \ll \xi$ ). Thus,  $\xi \sim \sqrt{l^m \xi_0}$ , which has the effect of reducing the actual size of a QPS and, with this, the energy barrier. From their calculations, they found that the role of the electromagnetic field in a previous work by Duan had been overestimated [Dua95], and that dissipative currents have a minor influence on the phase slip rate. In detail, the calculations are rather complex and intensive. However, in the following, a few important results from Refs. [Zai+97], [GZ01] and [AGZ08] will be summarized.

Characteristic for each phase slip is the suppression of the order parameter in its core and that it is accompanied by a phase winding around the core. Therefore it is reasonable to separate the action into two parts. A core part and an outer part  $S_{\text{QPS}} = S_{\text{core}} + S_{\text{out}}$ . The core action accounts for the condensation energy (essentially defining the potential barrier) and for dissipation caused by its normal conductive core. On the other hand,  $S_{\text{out}}$  is the hydrodynamic part, which depends on the propagating fields. Here only the fluctuations of the phase are important. For the outer part, the resulting action can be expressed as

$$S_{\text{out}} = \mu \ln \left( \frac{\min(c_0 \beta, L_w)}{\max(c_0 \tau_0, x_0)} \right) \quad (2.56)$$

with the Mooij-Schön mode velocity  $c_0 = 1/(C'L')^{1/2}$  [MS85],  $\beta = 1/T$ .  $L_w$  is the wire length,  $x_0$  is the typical size and  $\tau_0$  the time scale of a phase slip.  $C'$ ,  $L'$  are the capacitance and kinetic inductance per unit length. The prefactor is defined as  $\mu \simeq \pi/(4\alpha)(C'/L')^{1/2}$ . For extremely long wires and at temperatures close to  $T = 0$ , Eq. 2.56 diverges logarithmically. Thus, the outer part, describing the interaction with other phase slips, becomes large in this limit.

The core action  $S_{\text{core}}$  is calculated by means of a variational method with trial functions from the effective action. To relax this task, a numerical prefactor  $\beta$  (of the order of one) is introduced. The resulting core action then can be written in the following form:

$$S_{\text{core}} = \pi \beta N_0 A \sqrt{D \Delta_0} = \beta \frac{R_q L_w}{R_n \xi}, \quad (2.57)$$

where  $N_0 = m_e^2 v_F / (2\pi^2 \hbar^3)$  is the charge carrier density,  $A$  is the cross section area of the wire,  $\Delta_0$  is the superconducting gap,  $D$  is the diffusion constant,  $R_n$  is the normal state resistance and  $\xi = \sqrt{D/\Delta_0}$  is the coherence length. This result is only

valid for wire lengths  $L_w \ll \xi(e^2 N_0 A)/C'$  (satisfied for lengths up to  $\sim 10 \mu\text{m}$ ). For longer wires, capacitive effects become important and the core action takes the form:

$$S_{\text{core}}^* = \beta^* \left( \frac{R_q}{R_n \xi} \right)^{3/2} \sqrt{C'/(e^2 N_0 A)}. \quad (2.58)$$

For the purposes of this work, the long wire limit is not so important as typical wire lengths are between 100 nm and 1000 nm. To derive an expression for the attempt frequency  $\Omega_{\text{QPS}}$ , Zaikin and Golubev used instanton technique and introduced a second fitting parameter  $\alpha$ . Doing so, the pre-exponential factor can be expressed in terms of the QPS action:

$$\Omega_{\text{QPS}} = \alpha \frac{S_{\text{QPS}} L_w}{\tau_0 x_0} \Big|_{S_{\text{core}} \gg \mu} = \alpha \frac{\Delta_0 R_q L_w^2}{R_n \xi^2} \quad (2.59)$$

where it is assumed that  $x_0 \sim \xi$  and  $\tau_0 \sim 1/\Delta_0$ . For sufficiently short wires and for  $T \rightarrow 0$ , one can use the BCS relation for the gap  $\Delta_0 = 1.764 k_B T_c$  and express the QPS rate as:

$$\Gamma_{\text{QPS}} = \alpha' \frac{k_B T_c R_q L_w^2}{h R_n \xi^2} \exp\left(-\beta \frac{R_q L_w}{R_n \xi}\right) \quad (2.60)$$

This expression for the phase slip rate at zero current and temperatures close to  $T_c$  was later used by Mooij and co-workers to describe the phase slip energy  $E_s$ , when they investigated the superconductor-insulator transition in nanowires and in nanowire arrays [Moo+15]. Throughout this work, we will also follow this model for design considerations and the comparison with the experimental results.

For finite currents, the Golubev and Zaikin expression for the temperature dependent QPS resistance below  $T_c$  can be written in the form:

$$R_{\text{QPS,GZ}}(T) = \frac{\alpha \beta R_q^2 L_w^2}{R_n \xi(T)^2} \exp\left(-\beta \frac{R_q L_w}{R_n \xi(T)}\right) \quad (2.61)$$

with  $\xi(T) = 0.907 \xi_0 (1 + (1 - 0.25 t \xi_0 / t))^{-1/2} (1 - t^2)^{-1/2}$  ( $t = T/T_c$ ) [Del+12].

## 2.10 Duality between Josephson junctions and quantum phase slip junctions

In the previous sections, the concept of phase slips and some prominent models describing the probability of their occurrence were discussed. The considerations made referred to single, statistically occurring phase slips, which can be described by means of rates. The possible existence of coherent phase slips was first suggested

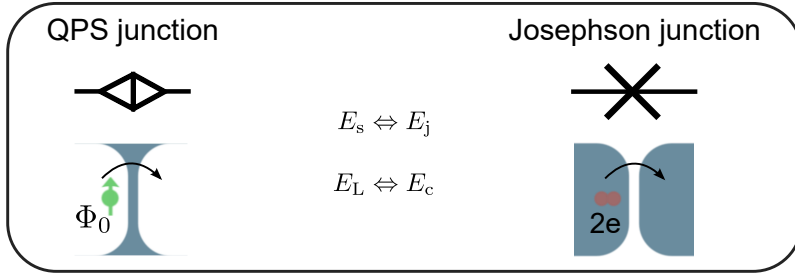


**Figure 2.5:** Comparison of a quantum phase slip junction and a Josephson junction: The dual to the tunneling of Cooper pairs at the Josephson junction is the tunneling of flux quanta across the wire (described by the energy  $E_s$ , each phase slip is linked with the tunneling of one  $\Phi_0$ ). The dual counterpart to the charging energy  $E_c$  is the inductive energy  $E_L$ .

by H. P. Büchler et al. in 2004 [BGB04]. Two years later, J. E. Mooji and Y. V. Nazarov took up this idea and proposed a duality between the well-known Josephson junctions and what they so-called quantum phase slip (QPS) junctions. Here, dual means that the dynamics of the phase slip junction can be mapped onto that of the Josephson junction by exchanging the conjugated variables charge and phase [MN06]. In the following, the main consequences of this dual approach will be explained. Then some examples for circuits and their dual counterpart are given. In Sec. 2.11.2, this duality will be used to derive the essential equations describing the behavior of a QPS interferometer. Since coherent QPS are assumed in the following, we will speak of phase slip amplitudes instead of rates.

A Josephson junction is typically formed by two superconductors separated by a thin insulating barrier (S-I-S). The strength of the coupling between the wave functions of the two superconductors is defined by the Josephson energy  $E_j$ . It is a measure for the amount of Cooper pairs that can tunnel through the junction. Naturally, such a geometry also comes along with a characteristic charging energy  $E_c = (2e)^2/2C$ . The ratio of these two energies is crucial for the properties of the junction. In contrast to the Josephson junction, in the case of a phase slip junction, the two superconductors are connected by a thin superconducting wire (much longer than the typical size of a phase slip,  $\sim \xi$ ). Here, the dual to the Josephson energy is the Phase slip energy  $E_s$ , which is proportional to the phase slip amplitude (rate). Since each phase slip event can be associated with a fluxon tunneling across the wire, the tunneling of fluxons can be seen as the dual to the tunneling of Cooper pairs. The dual to the charging energy  $E_c$  is the inductive energy  $E_L = \Phi_0^2/2L$ , which intuitively makes sense when comparing the geometries. Just as for the Josephson junction, the behavior of the QPS junction strongly depends on the ratio

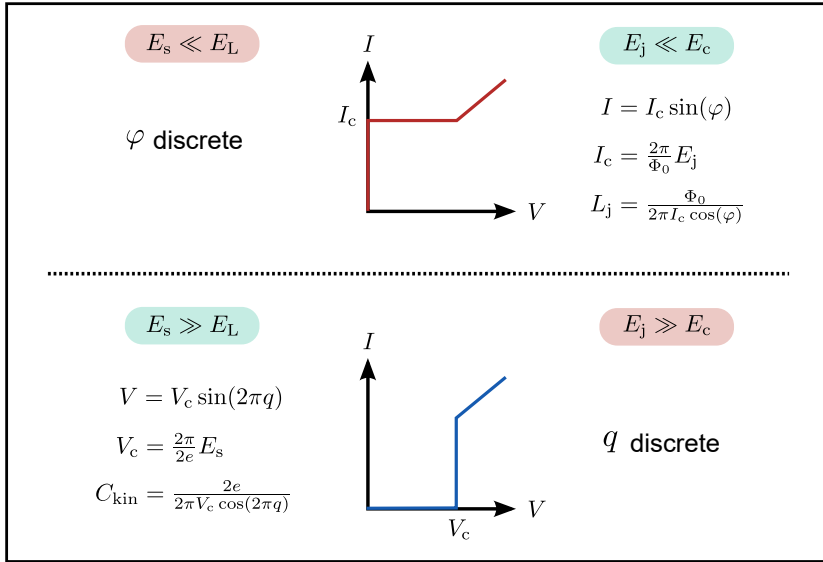


**Figure 2.6:** Energetic regimes for the Josephson junction and the QPS junction. The upper part shows the phase regime, the lower part the charge regime. The  $I - V$  curves in the middle show the respective characteristic transport behavior. Dual regimes are marked in the same color.

between  $E_s$  and  $E_L$ . An illustrative comparison of the two junction types is shown in Fig. 2.5.

Let us now consider the different energetic regimes (see Fig. 2.6): For a Josephson junction, in the limit  $E_j \gg E_c$ , the phase  $\varphi$  is a well-defined variable, and one can apply a current without dissipation up to a critical value  $I_c$ . This critical current is a measure for the Josephson energy  $I_c = 2\pi E_j / \Phi_0$ . Dual to this is a QPS junction in the regime  $E_s \gg E_L$  (later also called phase slip regime), where due to the strong fluctuation of the phase, no coherent charge transport through the wire is possible up to a critical voltage  $V_c$ . In this case, the charge  $q$  is a well-defined variable, and the critical voltage provides a measure for the phase slip energy  $V_c = 2\pi E_s / 2e$ . The inverse regime for the Josephson junction is  $E_j \ll E_c$  and for the QPS junction  $E_s \ll E_L$ . For the former, a Josephson junction reveals a Coulomb blockade, and the charge is well defined. For the latter, a supercurrent can flow through a QPS junction up to a critical value, and the phase is the well-defined variable. In Fig. 2.6, the corresponding dual regimes are marked with the same color.

For a Josephson junction, the supercurrent through the junction is given by the first Josephson equation and is a function of the phase difference of the wave functions

$\varphi$ :  $I = I_c \sin(\varphi)$  (see also Sec. 2.5). The associated nonlinear kinetic (or Josephson) inductance of the junction, resulting from the Josephson equations, is given by:

$$L_j = \frac{\Phi_0}{2\pi I_c \cos(\varphi)}. \quad (2.62)$$

Let us compare this with the dual equation for the QPS junction, resulting from the transformation made in Ref. [MN06]. Instead of a phase-dependent supercurrent, the QPS junction exhibits a threshold voltage  $V = V_c \sin(2\pi q)$ , which depends on the injected charge  $q$  (in units of  $2e$ ). Accordingly, the dual to  $L_j$  is a kinetic, nonlinear capacitance:

$$C_{\text{kin}} = \frac{2e}{2\pi V_c \cos(2\pi q)}. \quad (2.63)$$

The duality between Josephson junctions and QPS junctions, but also the transformation which allows transforming circuits with Josephson junctions into their dual circuit for QPS junctions, can be easily demonstrated by comparing the dynamics of two systems with each other [MN06]: The first system is the well known Josephson junction based Cooper pair box (CPB) ( $E_j \ll E_c$ ) [Bou+98]. Here the number of Cooper pairs on an island is quantized, and the energy spectrum is dominated by the quadratic capacitive energy  $E = E_c(N - n_g)^2$ . The left panel in Fig. 2.7 shows the CPB energy spectrum. The different parabolas correspond to a certain number  $N$  of Cooper pairs on the charge island. At half-integer values of  $n_g$ , Cooper pair tunneling through the junction removes the degeneracy. The energy splitting at these points is  $E_j$ . The Hamiltonian can be expressed as

$$H_{\text{CPB}} = E_c(N - n_g)^2 - \left( \frac{E_j}{2} \sum_n |N+1\rangle \langle N| + h.c. \right). \quad (2.64)$$

Here,  $n_g = CV/2e$  is the number of charges induced on the island.

The second (dual) system is the quantum phase slip flux qubit (QPSFQ), introduced by Mooij and Harmans in 2005 (operating in the regime  $E_s \ll E_L$ ) [MH05; MN06]. This qubit consists of a superconducting loop with an inductance  $L$  that is interrupted by a QPS junction. Instead of a certain number of Cooper pairs, we now find a discrete number  $N$  of flux quanta in the loop. Accordingly, the energy spectrum is now dominated by the parabolas from the inductive energy  $E = E_L(N - \Phi/\Phi_0)^2$  (see the right panel in Fig. 2.7). Dual to the CPB, the degeneracy at half integer flux quanta is now lifted by the tunneling of fluxons across the QPS junction, and the splitting equals  $E_s$ . The corresponding Hamiltonian now is

$$H_{\text{QPS}} = E_L(N - f)^2 - \left( \frac{E_s}{2} \sum_n |N+1\rangle \langle N| + h.c. \right) \quad (2.65)$$

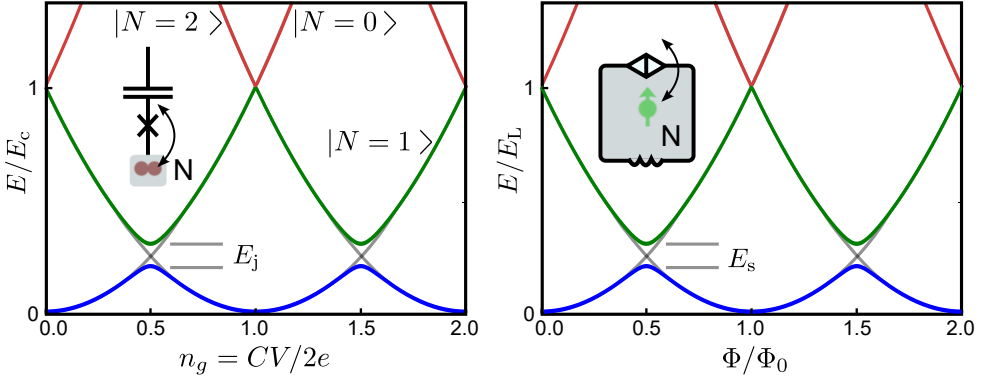


**Figure 2.7:** Energy spectra of the Cooper pair box (left) and the dual quantum phase slip flux qubit (right). The parabolas correspond to the different numbers ( $N$ ) of Cooper pairs/fluxoids. For half-integer values of  $n_g$  resp.  $\Phi/\Phi_0$ , the degeneracy is lifted by  $E_j$  resp.  $E_s$ .

with the frustration  $f = \Phi/\Phi_0$  and the number of flux quanta  $N$ . If we now compare the Hamiltonian of the Cooper pair box (Eq. 2.64) with that of the phase slip qubit (Eq. 2.65), we see that both have the same structure, but the following variables are interchanged:

$$E_c \Leftrightarrow E_L ; E_j \Leftrightarrow E_s ; n_g \Leftrightarrow f \quad (2.66)$$

In fact, any Josephson Hamiltonian can be mapped to the corresponding QPS Hamiltonian using the transformation proposed by Mooij and Nazarov [MN06]. Therefore, the following parameters need to be exchanged:

$$E_j \rightarrow E_s ; E_c \rightarrow E_L ; R_q^{-1}V \leftrightarrow I ; R_q^{-2}Z(\omega) \leftrightarrow Y(\omega) \quad (2.67)$$

with the conductance quantum  $1/R_q = 4e^2/h$ , the impedance  $Z$  and the admittance  $Y$ . For the double sided arrows, current and voltage bias are exchanged and parallel resistors turn into serial ones and vice versa.

For example, the dual to a current biased Josephson junction in the phase regime will become a voltage biased QPS junction in the charge regime with a serial resistor. The Josephson junction can be modeled with the well known resistively and capacitively shunted junction (RCSJ) model as an ideal junction which is shunted by a resistor  $R$  and a capacitance  $C$  [McC68; Ste68]. Following the transformation from Eq. 2.67, the ideal Josephson junction is replaced by the QPS junction, the parallel resistor turns into a serial resistor, and instead of a capacitance, we have an inductance. Consequently, the dynamics can be described in analogy to the

RCSJ model by a differential equation for the injected charge  $q$ . The two differential equations are [MN06]:

$$I(t) = I_c \sin(\varphi) + \frac{\Phi_0}{2\pi} \left( C \frac{d^2\varphi}{dt^2} + \frac{1}{R} \frac{d\varphi}{dt} \right) \quad (2.68)$$

$$V(t) = V_c \sin(2\pi q) + 2e \left( L \frac{d^2q}{dt^2} + R \frac{dq}{dt} \right). \quad (2.69)$$

We already can identify that both equations have the familiar form of the differential equation for a mechanical pendulum. Equations 2.68 and 2.69 can be rewritten in dimensionless variables after introducing the following two characteristic parameters. First the plasma frequency  $\omega_p$ , which defines the characteristic resonance of the junction. For the Josephson junction, this resonance stems from the capacitance  $C$  and Josephson inductance  $L_j$  of the junction. For the dual QPS junction, we have, instead of the normal capacitance, a kinetic capacitance  $C_{\text{kin}}$  and the inductance of the wire. Thus, we can write:

$$\omega_p^j = \frac{1}{\sqrt{L_j' C}} = \sqrt{\frac{2E_j E_C}{\hbar^2}} \quad \text{and} \quad \omega_p^{\text{QPS}} = \frac{1}{\sqrt{L C_{\text{kin}}'}} = \sqrt{\frac{2E_s E_L}{\hbar^2}} \quad (2.70)$$

With  $L_j' = \Phi_0/2\pi I_c$  and  $C_{\text{kin}}' = e/\pi V_c$ . The second parameter is the so called McCumber parameter  $\beta_c$  and its dual counterpart, describing the damping in the running state [McC68; MN06]:

$$\beta_c^j = \frac{2\pi R^2 C I_c}{\Phi_0} \quad \text{and} \quad \beta_c^{\text{QPS}} = \frac{2\pi L V_c}{2e R^2} \quad (2.71)$$

With these parameters and after introducing the normalized time  $t' = \omega_p^{j,\text{QPS}} t$ , Eq. 2.68 and 2.69 can be rewritten as:

$$\frac{I(t')}{I_c} = \sin(\varphi) + \frac{d^2\varphi}{dt'^2} + \frac{1}{\sqrt{\beta_c^j}} \frac{d\varphi}{dt'} \quad (2.72)$$

$$\frac{V(t')}{V_c} = \sin(2\pi q) + \frac{d^2q}{dt'^2} + \frac{1}{\sqrt{\beta_c^{\text{QPS}}}} \frac{dq}{dt'} \quad (2.73)$$

These differential equations can be treated as phase resp. charge particles with mass ( $m_j = C(\Phi_0/2\pi)^2$  and  $m_{\text{QPS}} = L(2\pi/2e)^2$ ) moving in a washboard potential (see Fig. 2.8). Thus the corresponding effective potentials take the form:

$$U_j(\varphi) = -E_j \left( \frac{I}{I_c} \varphi + \cos(\varphi) \right) \quad \text{and} \quad U_{\text{QPS}}(q) = -E_s \left( \frac{V}{V_c} 2\pi q + \cos(2\pi q) \right) \quad (2.74)$$

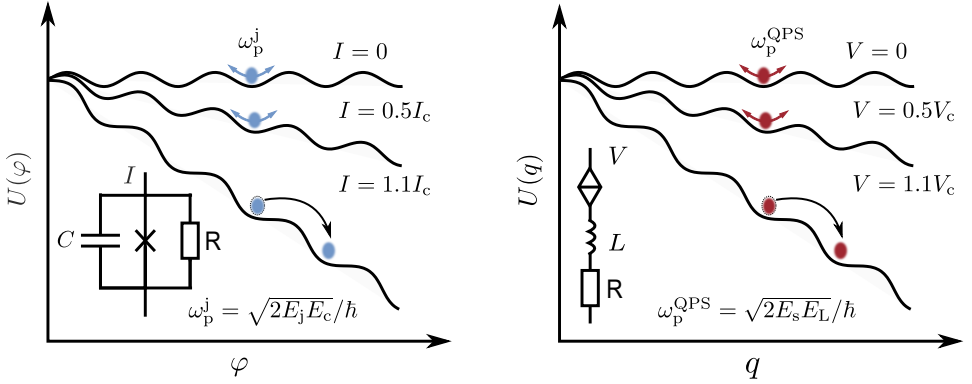


**Figure 2.8:** Tilted washboard potential for a Josephson junction (JJ) ( $E_j \gg E_c$ , left) and a QPS junction (QJ) ( $E_s \gg E_L$ , right). The dynamics can be described by a phase particle (JJ) or a charge particle (QJ). For bias values below  $I_c$  resp.  $V_c$ , the particle is trapped in a minimum, where it oscillates with the plasma frequency  $\omega_p^j$  resp.  $\omega_p^{\text{QPS}}$ . With increasing bias values, the potential gets more and more tilted until the barrier height ( $E_j$  resp.  $E_s$ ) is overcome, and the particle is in the running state. For the Josephson junctions, the change in phase ( $\dot{\varphi}$ ) results in a voltage across the junction, while for the QPS junction, the change of the charge ( $\dot{q}$ ) leads to a current through the wire. The friction/damping of the particles is then described by  $\beta_c^j$  resp.  $\beta_c^{\text{QPS}}$ . The equivalent circuits from the RCSJ model (JJ) and the dual for the phase slip model are illustrated in the insets.

Fig. 2.8 shows the two washboard potentials for different bias values together with the corresponding circuits. In Sec. 2.11.2 it will be shown that the differential equation for two strongly coupled wires with serial resistors has the same form as Eq. 2.72 for a single wire.

## Superconductor-insulator transition

So far we have only discussed the phase slip junction in the extreme regimes ( $E_s \ll E_L$  or  $E_s \gg E_L$ ). Thus, the question naturally arises when the transition from a superconducting behavior (phase regime) to an insulating behavior (phase slip regime) occurs. In a paper by Mooji and co-workers, published in 2015, this question of when the transition from an inductive to a capacitive response occurs, is explored for nanowires as QPS junctions [Moo+15]. The transition is assumed to be a non-dissipative one and to be only driven by the interplay between the characteristic energies  $E_s$  and  $E_L$ .

This approach differs from the Chakravarty-Schmid-Bulgadaev (CSB) theory, which assumes a dissipative environment and predicts a transition at a critical resistance  $R_n = R_q = 6.45 \text{ k}\Omega$ . While it was reported that the CSB theory fits for some wires

(e.g. in Ref [MOR07] for MoGe wires with  $L_w < 200$  nm), it fails for others (e.g. MoGe wires in Ref. [Bol+08] or NbTiN wires in Ref. [Mak+16]). These observations fit with the considerations of Mooji and co-workers that the ratio of the energies is decisive and not an upper bound for the normal state resistance.

In order to find a reasonable boundary for the transition from one regime to the other, a suitable description for the link between the wire parameters and the phase slip energy  $E_s$  resp. the inductive energy  $E_L$  must be found. Since for wires with a high phase slip rate/amplitude, the kinetic inductance is typically very high, it can be assumed that  $L = L_{\text{geometric}} + L_{\text{kin}} \approx L_{\text{kin}}$  [Moo+15]. Thus, for temperatures close to  $T = 0$ , the inductive energy can be represented as:

$$E_L = \frac{\Phi_0^2}{2L} = \frac{\Phi_0^2 k_B T_c}{0.36 \hbar R_n} = 17.4 k_B T_c \frac{R_q}{R_n} \quad (2.75)$$

where we have used the expression for  $L_{\text{kin}}$ , derived in Sec. 2.7 (Eq. 2.36).  $R_q = h/4e^2$  is the quantum resistance,  $k_B$  the Boltzmann constant and  $T_c$  is the critical temperature. To describe the phase slip energy  $E_s$ , Mooji and co-workers were following the expression from Zaikin and Golubev for the QPS rate in the short wire limit and at temperatures close to  $T = 0$  (discussed in details in Sec. 2.9.2):

$$E_s = \alpha \left( \frac{L_w}{\xi} \right)^2 k_B T_c \frac{R_q}{R_n} \exp \left( -\beta \frac{R_q L_w}{\xi R_n} \right) \quad (2.76)$$

with the wire length  $L_w$  and the coherence length  $\xi$ ;  $\alpha$  and  $\beta$  are empirical constants that are of the order of 1 [Moo+15]. Please note that Eq. 2.76 is just the phase slip rate from Eq. 2.60 expressed as energy.

For Josephson junctions, the transition from superconducting to insulating behavior happens at  $E_c/E_j \sim 1$  and not in a sharp manner. In the transition region, a phase diffusion behavior is observed with a non-vanishing differential resistance, even for smallest bias values. In the previously discussed washboard potential, this can be understood by macroscopic quantum tunneling through the potential barrier or by a thermally activated overcoming of the potential barrier, leading to phase slips (see also Sec. 2.9.2). Which process is dominant in each case depends on the respective energies  $E_j$ ,  $E_c$  and  $k_B T$ . Based on this knowledge, a sharp transition at a certain value of  $E_s/E_L = \alpha_0$  would not necessarily be expected for QPS junctions. However, it can also be assumed that the crossover should be somewhere around  $E_s/E_L \sim 1$  [Moo+15]. From Eq. 2.75 and Eq. 2.76 one already can see that two driving parameters for the phase transition are the normal state resistance and the length of the wire. Dividing both equations, one obtains:

$$\frac{E_s}{E_L} = \alpha \left( \frac{L_w}{\xi} \right)^2 \frac{0.18}{\pi} \exp \left( -\beta \frac{R_q L_w}{\xi R_n} \right) = \alpha_0. \quad (2.77)$$

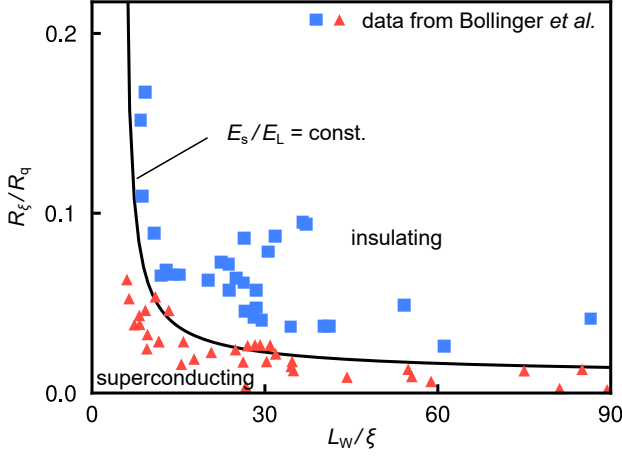


**Figure 2.9:** Phase diagram for MoGe nanowires: The two regimes, insulating and superconducting, are associated with  $E_s/E_L \gg 1$  and  $E_s/E_L \ll 1$ . Blue squares correspond to wires with non-vanishing resistances below  $T_c$ , red triangles correspond to wires with clear superconducting behavior below  $T_c$ . The solid black line follows Eq. 2.78. The diagram is reconstructed after Ref. [Moo+15]. The data are from Bollinger *et al.* [Bol+08].

Thus, for the relation between wire resistance  $R_n$  and wire length  $L_w$  for a fixed ratio between  $E_s$  and  $E_L$  one can write:

$$\frac{R_n \xi}{R_q L_w} = \frac{R_\xi}{R_q} = \frac{\beta}{\ln \left( \frac{\alpha (L_w/\xi)^2}{17.4 \alpha_0} \right)} \quad (2.78)$$

with the resistance per coherence length  $R_\xi = R_n \xi / L_w$ . To investigate whether there is a constant ratio  $\alpha_0$  for which the transition from the phase regime to the charge (or phase slip) regime occurs Mooji and co-workers have used Eq. 2.78 to probe if the experimental data, obtained in Ref. [Bol+08] for MoGe nanowires, allow for a phase separation at a certain  $\alpha_0$ . Fig. 2.9 shows the resulting phase diagram [MN06]. The blue squares correspond to wires which showed a strongly increased or a non vanishing resistance below  $T_c$  (classified as insulating). The red triangles represent wires with fully vanishing resistances below  $T_c$  (classified as superconducting). For the separation line, Eq. 2.78 is used with  $\alpha \approx 0.2$ ,  $\beta \approx 0.11$  and  $\alpha_0 \approx 0.3$ .

The fact that the data can be clearly separated for a specific  $\alpha_0$  confirms that the ratio  $E_s/E_L$  determines the superconductor to insulator transition. Also the value of  $\alpha_0 \approx 0.3$  fits the expected one of  $\sim 1$ . However, similarly good results can be obtained for other combinations of parameters [Moo+15]. This uncertainty comes

from the indeterminacy of the empirical parameters  $\alpha$  and  $\beta$ . In Fig. 2.9, samples which did not show a clear Coulomb blockade but a non-vanishing resistance or a pronounced zero bias anomaly (ZBA) below  $T_c$ , also fall into the insulating range. Bollinger *et al.* attributed this behavior to a dynamical weak Coulomb blockade, caused by coherent scattering [Naz99; BRB06].

This means that no precise statement can be made about a possible intermediate regime, such as the phase diffusion regime for Josephson junctions. Nevertheless, the data and the theory fit very well. In fact, using the same approach, it was shown that the SIT transition of NbTiN nanowires can also be described with such a phase diagram and similarly chosen parameters [Mak+16].

## 2.11 Superconducting quantum interference devices

### 2.11.1 The DC SQUID

The direct current SQUID is one of the most prominent superconducting quantum circuits. It was already invented two years after the discovery of the Josephson effect and essentially comprises a superconducting loop in which two Josephson junctions are embedded (see Fig. 2.10). The working principle is based on phase coherence and flux quantization. An externally applied magnetic flux allows for controlling the phase differences at both junctions and, therefore, controlling the maximum supercurrent across the SQUID. Using the first Josephson equation and Kirchhoff's law, the current can be expressed as:

$$I_m = I_1 + I_2 = I_c \sin(\varphi_2 - \varphi_1) + I_c \sin(\varphi_4 - \varphi_3) \quad (2.79)$$

$$= I_c \sin(\delta_1) + I_c \sin(\delta_2) \quad (2.80)$$

$I_{1,2}$  denote the supercurrent through each junction,  $\delta_{1,2}$  are the phase differences across the junctions. For simplicity it is now assumed that both junctions share the same critical current  $I_c$ , and that the circuit is homogeneous. Using an addition theorem, we find:

$$I_m = 2I_c \sin\left(\frac{\delta_1 + \delta_2}{2}\right) \cos\left(\frac{\delta_2 - \delta_1}{2}\right) \quad (2.81)$$

To find the gauge invariant relation between the phase differences and the magnetic field enclosed in the loop one can integrate along the contour (see Fig. 2.10). From the flux quantization, we know that  $\oint_c \nabla \varphi d\mathbf{l} = 2\pi n$ . Rewriting the phase gradient

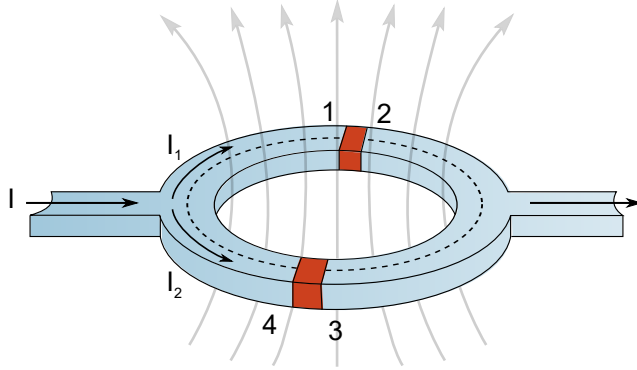


**Figure 2.10:** Sketch of a direct current superconducting quantum interference device: The current  $I$  enters on the left side and splits into two paths ( $I_1$ ,  $I_2$ ). The two Josephson junctions are marked with red. The numbers 1 to 4 mark the different sections of the contour for the integration of the phase gradient. Inside the loop, a magnetic flux is enclosed.

$\nabla\varphi = (2\pi/\Phi_0)(\mu_0\lambda_L^2\mathbf{j} + \mathbf{A})$  ( $\mathbf{j}$  is the supercurrent density,  $\mathbf{A}$  the vector potential and  $\lambda_L$  the London penetration depth), one can find that (see e.g. Ref. [BK12]):

$$\oint_c \nabla\varphi d\mathbf{l} = \delta_1 - \delta_2 + \underbrace{\frac{2\pi}{\Phi_0} \oint_c \mathbf{A} d\mathbf{l}}_{(*)} + \underbrace{\frac{2\pi\mu_0\lambda_L^2}{\Phi_0} \left( \int_1^4 \mathbf{j} d\mathbf{l} - \frac{2\pi}{\Phi_0} \int_3^2 \mathbf{j} d\mathbf{l} \right)}_{(**)} = 2\pi n \quad (2.82)$$

where (\*) defines the magnetic flux in the ring and is the crucial part for the flux dependent modulation of  $I_m$  ( $\oint \mathbf{A} d\mathbf{l} = \oint \mathbf{B} ds$ ). The external magnetic field will also induce a circulating screening current  $I_{sc} = (I_1 - I_2)/2$ , therefore, the total flux from (\*) is  $\Phi^* = \Phi_{ex} + \Phi_{i1} = SB + L_g I_{sc}$  ( $S$  is the effective enclosed area of the SQUID,  $L_g$  is the geometric inductance). The second part (\*\*) gives the contribution from the kinetic inductance of the loop ( $\Phi^{**} = \Phi_{i2} = L_k I_{sc}$ ). Consequently, the total flux is given by  $\Phi_t = \Phi_{ex} + LI_{sc}$ , where  $L$  is the total inductance. Using Eq. 2.82, the phase differences can be expressed as

$$\delta_2 - \delta_1 + 2\pi n = \frac{2\pi\Phi_t}{\Phi_0} \quad (2.83)$$

which now can be inserted into Eq. 2.79 to yield the current across the SQUID as a function of the magnetic flux:

$$I_m = 2I_c \sin\left(\frac{\pi\Phi_t}{\Phi_0} + \delta_1\right) \cos\left(\frac{\pi\Phi_t}{\Phi_0} n\right) \quad (2.84)$$

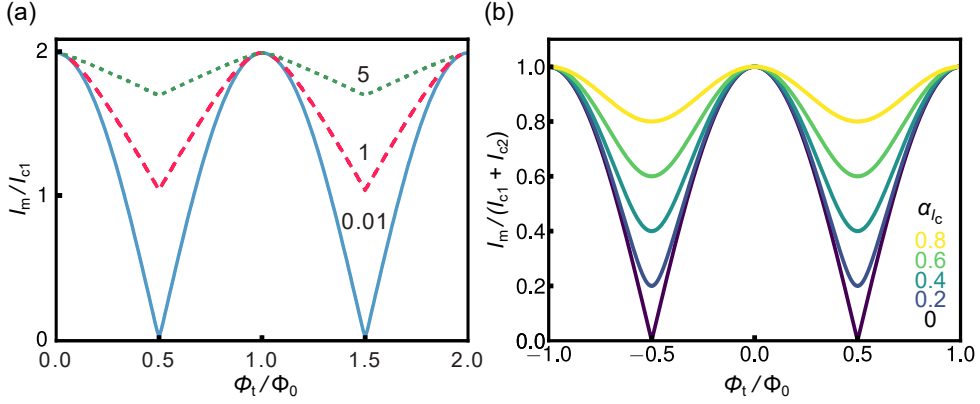


**Figure 2.11:** (a) Simulated critical current as a function of the applied flux for different screening parameters ( $\beta_L = 0.01, 1, 5$ ). It is assumed that both junctions share the same  $I_c$ . For large screening parameters, the possible interference is suppressed. Adapted from Ref. [CB04] (b) Modulation of the critical current as a function of the applied flux for different asymmetries (and  $\beta_L \ll 1$ ). The parameter  $\alpha_{I_c}$  determines the symmetry between the critical currents:  $I_{c1} = I_{c2}(1 - \alpha_{I_c})/(1 + \alpha_{I_c})$ .

Assuming that the flux  $\Phi_t$  is fully dominated by the external flux and is constant (which means screening effects can be neglected,  $\Phi_t = \Phi_{ex}$ ), Eq. 2.84 can be maximized by finding the solution for  $\partial I_m/\partial \delta_1 = 0$ . The maximal critical current of the SQUID therefore holds:

$$I_m^* = 2I_c \left| \cos \left( \frac{\pi \Phi_{ex}}{\Phi_0} \right) \right| \quad (2.85)$$

In this case the maximum possible modulation ranges from  $I_m^* = 0$  for  $\Phi_{ex} = n\Phi_0/2$  ( $n \in \mathbb{N}$ ) up to  $I_m^* = 2I_c$  for  $\Phi_{ex} = n\Phi_0$  ( $n \in \mathbb{N}_0$ ). For significant loop inductances, this approximation is not valid anymore, and screening effects become important. To distinguish between different regimes, the screening parameter  $\beta_L$  may be introduced. It essentially describes the ratio between the loop inductance and the Josephson inductances of the two junctions:

$$\beta_L = \frac{2I_c L}{\Phi_0} \quad (2.86)$$

For Eq. 2.85, it was assumed that  $\beta_L \ll 1$ . In the opposite regime of  $\beta_L \gg 1$  the phase of the order parameter will mainly drop over the loop inductance, and the circulating current  $I_{sc}$  has only a poor effect on the phase drops across the junctions. Thus, the modulation with applied flux gets highly suppressed (by a factor  $1/\beta_L$ ) and only slightly modulates around  $2I_c$ . Fig. 2.11 (a) shows the modulation of the critical current with applied field for different  $\beta_L$  parameters.

So far, we have assumed that both junctions have the same critical current. In reality, this is most likely not the case and has to be taken into consideration. Following Ref. [Lik86], the general form for the critical current (low inductance limit  $\beta_L \ll 1$ ) can be expressed as:

$$I_m = \sqrt{I_{c1}^2 + I_{c2}^2 + 2I_{c1}I_{c2} \cos(\Phi_{ex})} \quad (2.87)$$

For identical critical currents, we find the same modulation as before (2.85). However, if we now assume extremely different critical currents (e.g  $I_{c2} \ll I_{c1}$ ), Eq 2.87 can be approximated to

$$I_m \approx I_{c1} \left( 1 + \frac{I_{c2}}{I_{c1}} \cos(\Phi_{ex}) \right), \quad (2.88)$$

where the strength of the modulation is given by the ratio  $I_{c2}/I_{c1}$  and the critical current modulates just slightly around  $I_{c1}$ . Fig. 2.11 (b) shows how the modulation of the critical current develops for different assumed asymmetries between  $I_{c1}$  and  $I_{c2}$ . We have seen that both, the symmetry and the ratio between loop inductance and junction inductances, define the maximum possible modulation of  $I_m$ .

## 2.11.2 The quantum phase slip interferometer

In the previous section, we have discussed the DC SQUID, probably the most prominent example of a quantum interferometer. The principle of operation was based on the phase shift of the wave function describing the Cooper pair condensate. In this section, the underlying idea and the most important properties of a quantum phase slip interferometer will be presented. In the course of the discussion, it will turn out that many of the considerations made for the SQUID can be applied analogously. In the context of the present work, a central goal was the realization and investigation of such a circuit.

For the QPS interferometer, the interference is caused by the Aharonov-Casher effect (AC), describing the acquired phase shift for a particle with magnetic momentum when traveling through the electric field of a charge [AC84]. The charge flux dual to the tunneling of Cooper pairs through a Josephson junction is the tunneling of flux quanta across a phase slip junction (see Sec. 2.10). Each phase slip is linked with the tunneling of a flux quantum.

If we now imagine a charged island with charge  $q$ , around which coherent fluxons move in different directions, they can accumulate a relative phase to each other according to the AC effect. Depending on the phase factor, the resulting interference

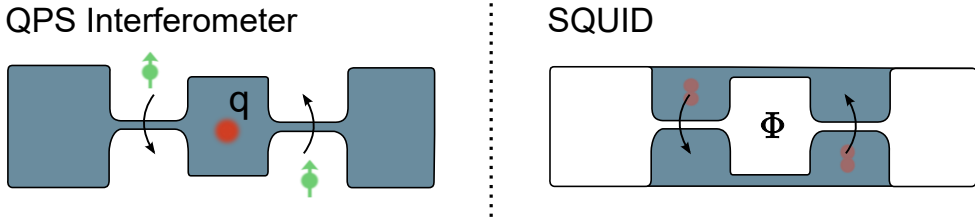


**Figure 2.12:** Illustration of a QPS interferometer and its dual counterpart, the SQUID for Josephson junctions: At the SQUID, Cooper pairs flow around a magnetic flux, which manifests as field dependent oscillations of the critical current. For the QPS interferometer, fluxons move around a charge, leading to a charge dependent critical voltage. Note that also the respective structures correspond to the inverse of each other. The drawing is made after Ref. [Gra+18].

can be constructive or destructive. Combining this idea with the connection between a phase slip and the tunneling of a fluxon, one arrives at the basic idea of a phase slip interferometer. It should be noted at this point that in the following, instead of phase slip rates, we speak of phase slip amplitudes. The reason for this is the necessity of coherent phase slips for interference.

The simplest possible arrangement for such a device is to have two phase slip junctions in series, separated by a small charge island. The two phase slip junctions can be represented by a characteristic function with the phase slip amplitudes  $V_{1,2}$  and the corresponding phase factors  $\varphi_{1,2}$ :  $A_{1,2} = V_{1,2}e^{i\varphi_{1,2}}$ . Thus, the effective phase slip amplitude of the double junction system is given by  $A_e = A_1 + A_2$ . If we now take into consideration that the phase slips are associated with fluxons, tunneling across the wire, and include the Aharonov-Casher effect, we find that the phase factor  $\varphi_{1,2}$  will depend on the charge on the island. In this spirit, the QPS interferometer can be seen as dual to a DC SQUID for Josephson junctions, where the encircled flux causes the interference between the Cooper pair wave functions. Fig. 2.12 shows an illustrative comparison between a DC SQUID and a QPS interferometer. The former can be seen as an implementation of the Aharonov-Bohm effect and the second as an implementation of the dual Aharonov-Casher effect [Gra+18]. Both effects are explained in Sec. 2.8.

To have a well-defined charge on the island, it must be isolated from the environment. For sufficiently large phase slip amplitudes, the phase coherence between the ends of a wire can be destroyed, resulting in Coulomb blockades with associated capacitances [MN06]. This case is given when the phase slip energy of the wires is significantly larger than their inductive energy ( $E_s \gg E_L$ ). In this case, the induced charge on the island and thus also the interference of the phase slips can be precisely controlled by means of a gate electrode.

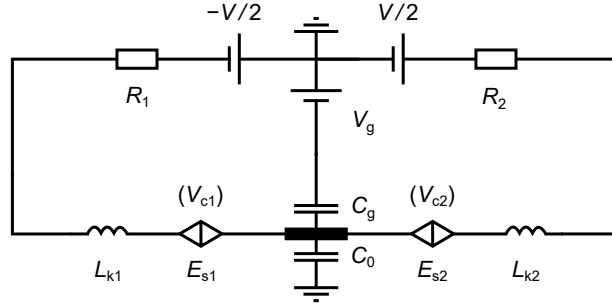


**Figure 2.13:** Circuit diagram of the phase slip interferometer, proposed in Ref. [HZ12].  $L_{k1,2}$  and  $E_{s1,2}$  are the kinetic inductance and phase slip energy of the wires.  $C_0, C_g$  are the self capacitance of the island and the gate capacitance.  $R_{1,2}$  are the high ohmic resistors for decoupling and damping.

In 2012, Zorin and Hongisto presented a circuit that should be the exact dual to that of a DC SQUID for Josephson junctions but for QPS junctions, acting as a single charge transistor [HZ12]. It is based on the proposed duality, discussed in Sec. 2.10. To briefly repeat the main features: Instead of a periodic supercurrent  $I = I_c \sin(\varphi)$ , depending on the phase difference  $\varphi$  between the two separated superconductors, a QPS junction (for  $E_s \gg E_L$ ) should have a periodic voltage  $V_{\text{QPS}} = V_c \sin(2\pi q/e)$ , which depends on the injected charge  $q$  and the phase slip energy ( $V_c = 2\pi E_s/2e$ ). The dual to the Josephson inductance is a nonlinear,  $2e$  periodic, kinetic capacitance  $C_{\text{QPS}}^{-1} = dV_{\text{QPS}}/dq = (\pi V_c/e) \cos(\pi q/e)$ , which is sensitive to the injected charge.

The proposed device essentially comprises two high ohmic resistors to decouple the interferometer from its environment, two nanowires as QPS junctions, a wider segment in between (serving as the charge island), and a capacitively coupled DC gate. Fig. 2.13 shows a simplified circuit diagram of the device. Here, the resistors are represented by  $R_{1,2}$ , the kinetic inductances of the wires are  $L_{k1,2}$ , and the phase slip amplitudes are represented by the diamond symbols.  $C_g, C_0$  are the gate capacitance and self capacitance of the island. Using the relation between the injected charge and the voltage on the QPS junction from the duality, Kirchhoff's equation for each branch can be expressed as:

$$V_{1,2} = L_{k1,2}\ddot{q}_{1,2} + R_{1,2}\dot{q}_{1,2} + V_{c1,2} \sin(2\pi q_{1,2}/e) \quad (2.89)$$

[HZ12]. The voltage across the device then is  $V = V_1 + V_2$ . Since it is assumed that both wires have a Coulomb blockade, one can use the charge conservation relation for the island (illustrated in Fig. 2.14) to express the injected charges  $q_{1,2}$  in terms of the applied gate voltage:

$$q_1 - q_2 = -C_g V_g - (C_g + C_0)(V_1 + V_2) = 0. \quad (2.90)$$

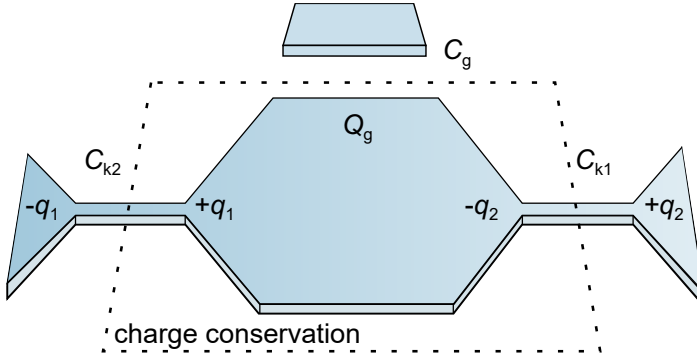


**Figure 2.14:** Illustration of the QPS interferometer: The wider section is isolated by the kinetic capacitances of the nanowires. Consequently, charge conservation holds on the island.  $Q_g$  is the polarization charge from the gate,  $q_{1,2}$  are the injected charges on the wires. For  $C_{k1,2} \gg C_g$ , both wires are strongly coupled. The self capacitance of the island  $C_0$  is neglected. .

The distribution of the charges will strongly depend on the different capacitances. The wire capacitances scale with  $e/V_{c1,2}$  which means that in the limit  $C_g, C_0 \ll e/V_{c1,2}$ , the charges  $q_1$  and  $q_2$  will be fully controlled by the applied gate voltage and Eq. 2.90 can be approximated to:

$$q_1 - q_2 = -C_g V_g. \quad (2.91)$$

This condition is just the same as the low impedance limit for the DC SQUID. If we compare Eq. 2.91 with Eq. 2.83 we can identify that the phase differences are replaced by the charges and that the previously made approximation is just the same as the neglecting of the screening current contribution to the total flux. Instead of the Josephson inductances, which scale with  $1/I_c$ , we now have the wire capacitances scaling with  $1/V_c$ . The dynamic contributions in Eq. 2.89 are the equivalent to the shunting resistor and capacitance of the Josephson junctions and are important to describe the current state. For now, we stick to the limit  $C_g, C_0 \ll e/V_{c1,2}$  and the steady state.

To describe the common voltage of both wires  $V = V_{c1} \sin(2\pi q_1/e) + V_{c2} \sin(2\pi q_2/e)$ , Zorin and Hongisto followed the derivation from Ref. [Lik86] for the steady state of the DC SQUID and analogously introduced an average charge  $Q$  to rewrite the voltage as:

$$V = V_c(Q_g) \sin(\pi Q/e) \quad (2.92)$$

with the gate induced charge  $Q_g$  and the effective critical voltage:

$$V_c = \sqrt{V_{c1}^2 + V_{c2}^2 + 2V_{c1}V_{c2} \cos(\pi Q_g/e)}. \quad (2.93)$$

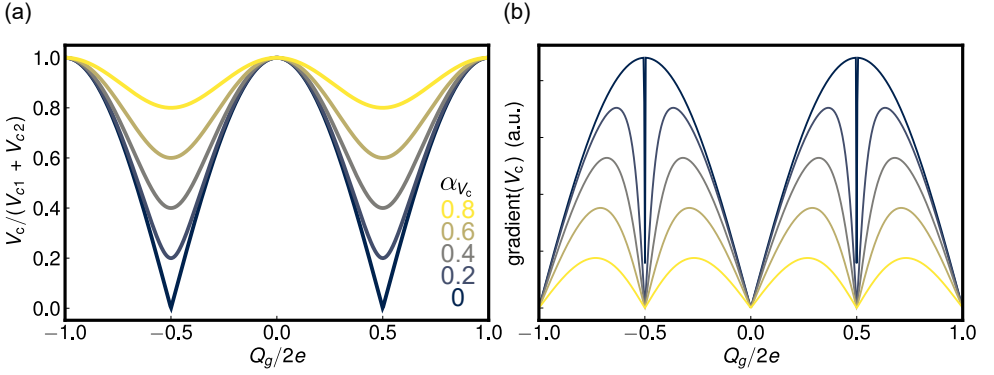


**Figure 2.15:** (a) Threshold voltage of the circuits vs. induced charge for different asymmetries between the phase slip amplitudes ( $V_{c1,2}$ ) and a strong coupling between the nanowires. The symmetry parameter is given by  $V_{c1} = V_{c2}(1 - \alpha_{V_c}) / (1 + \alpha_{V_c})$ . (b) Gradient of the modulation. For small asymmetry and close to  $V_c^{min}$ , the modulation becomes very sensitive to small charge fluctuations in  $Q_g$ .

From Eq. 2.92, we see that for the situation of strong coupling, both wires together behave like a single wire with an average charge and a critical voltage that depends on the gate induced charge. Eq. 2.93 is the dual to Eq. 2.87 for the SQUID, just with exchanged variables  $I_{c1,2} \leftrightarrow V_{c1,2}$ . Consequently, we find the same limits when assuming a highly symmetrical or asymmetrical circuit. For the former case, when  $V_{c1} = V_{c2}$ , the average charge  $Q = q_{1,2} \pm Q_g/2$  and the maximum modulation of the circuit's critical voltage is described by

$$V_c = 2V_{c1} |\cos(\pi Q_g/e)|. \quad (2.94)$$

In the asymmetrical limit, one of the wires will fully dominate the critical voltage and the modulation is only weak (e.g.  $V_{c1} \gg V_{c2} \rightarrow Q \approx q_1$ ). Thus, the maximum modulation of the blockade is:

$$V_c = V_{c1} [1 + V_{c2}/V_{c1} \cos(\pi Q_g/e)]. \quad (2.95)$$

The parameter  $a = V_{c2}/V_{c1}$  describes the strength of the modulation but might not be a good measure to describe the homogeneity of the circuit, as will be discussed later. From Eq. 2.94, we see that for the strong coupling limit and equal phase slip amplitudes on both wires, it might be possible to suppress the critical voltage fully. If we assume that the phase slip amplitudes from both sides neutralize each other completely by destructive interference, this is obvious. However, even at a rest net amplitude, the blockade could vanish, since the exact point at which the transition from blockade to no blockade takes place will depend on the cross over

from the regime  $E_s \gg E_L$  to the regime  $E_s \ll E_L$  [Vos+21]. Here,  $E_s$  and  $E_L$  are the common phase slip energy and inductive energy of both wires. Fig. 2.15 (a) shows the modulation of the threshold voltage for different asymmetries. For devices with almost equal amplitudes on both wires, the threshold voltage modulation becomes extremely sensitive to small charge fluctuations around maximal destructive interference (see Fig. 2.15 (b)).

Since the double wire system behaves like a single wire for strong coupling, correspondingly the dynamics can also be represented by the differential equation for a single wire with resistance  $R = R_1 + R_2$  and total inductance  $L = L_{k1} + L_{k2}$  [HZ12]. Using Eq. 2.92, the voltage is [MN06; HZ12]:

$$V = L\ddot{Q} + R\dot{Q} + V_c(Q_g) \sin(\pi Q/e) \quad (2.96)$$

In analogy to the resistively shunted junction model for Josephson junctions the dual McCumber parameter  $\beta_c^{\text{QPS}} = 2\pi^2(E_s(Q_g)/E_L)(R_q/R)^2 = \omega_p \frac{L}{R}$  with the plasma frequency  $\omega_p = \sqrt{2E_s(Q_g)E_L}$  can be introduced to describe the damping of the system [MN06]. These equations are just the same as the ones for a single wire (see Sec. 2.10), but now with a gate dependent phase slip energy  $E_s(Q_g)$ .

For some applications (e.g. the synchronization of charge oscillations), a sufficiently large damping might be necessary. However, an increase of the resistances can also cause overheating of the circuit [EN21]. This is particularly problematic for small phase slip amplitudes/blockades as will be discussed in Sec. 2.12.2.

So far, we have considered only the case of strongly coupled wires (Eq. 2.92). To distinguish between the different coupling regimes, it makes sense to introduce a parameter that is the analogous counterpart of the screening parameter  $\beta_L$  in SQUIDs, describing the ratio between the island capacitance and the kinetic capacitances of the wires [EN21]:

$$\beta_s = \frac{C_{isl}}{C_{kin}} = \frac{\pi(C_g + C_0)}{2e}(V_{c1} + V_{c2}). \quad (2.97)$$

For the kinetic capacitance, the mean value of both wires is used. For sufficiently small islands, the self capacitance  $C_0$  can be neglected. The strong coupling is reached for  $\beta_s \ll 1$ , the weak coupling for  $\beta_s \gg 1$  and the intermediate regime regime for  $\beta_s \approx 1$ .

In the weak coupling regime ( $\beta_s \gg 1$ ), both wires effectively get decoupled by the large capacitance, and the possible interference gets limited. The maximal threshold voltage in this limit can be expressed as:

$$V_c = \left(1 - \frac{\bar{q}_g}{2\beta_s}\right) (V_{c1} + V_{c2}) \quad (2.98)$$

with  $\bar{q}_g = (\pi C_g V_{c2}/e - \pi C_g V_g/e) \bmod 2\pi$  [EN21]. In this regime, the possible modulation is only weak even when assuming the same phase slip amplitudes for both wires ( $V_{c1} = V_{c2}$ ). From Eq. 2.98 we find that with increasing coupling parameters, the modulation will be more and more suppressed (roughly with  $1/\beta_s$ ), just as we have seen at the SQUID for large screening. While for  $\beta \approx 3$ , the minimal voltage  $V_c^{\min}$  is still  $\approx 0.5(2V_{c1})$ , for  $\beta \approx 50$  the modulation is below ten percent of the maximum threshold voltage. For the intermediate regime  $\beta_s \approx 1$  and  $V_{c1} = V_{c2}$  the minimal blockade is  $V_c^{\min} \approx 0.2(2V_{c1})$ .

Experimentally and for possible applications, the most interesting regime is the one of strong coupling. For moderate critical voltages  $V_{c1,2} < 1$  mV this can be easily obtained by an island capacitance  $C_g + C_0 \approx 10$  aF. To prevent a strong effect from ground and gate noise, it can be advantageous to keep the island as small as possible and the coupling to the gate not too strong.

Finally, we briefly want to discuss the effect of finite temperatures. For  $T > 0$  the two relevant energies are the thermal energy  $k_B T$  and the Coulomb energy  $e(V_{c1} + V_{c2})$ . Thus, at least when the thermal energy approaches the Coulomb energy, the transition from blockade to the conductive state will become more smooth, or the blockade will even fully vanish. In a recent study by Erdmanis and Nazarov, the gradual temperature effects on the shape of the  $I - V$  curves of a QPS interferometer were investigated within a semiclassical model [EN21]. In their model, a stochastic term is introduced to account for the white noise coming from the high ohmic resistors. Fig. 2.16 shows simulated  $I - V$  characteristics for a device with  $\beta_s = 0.1$  (a) and  $\beta_s = 50$  (b) [EN21]. For increasing temperatures, the blockade smears out, and the transition to the current state appears at smaller voltages. An intuitive but also interesting finding is that when comparing the smoothing of strongly and weakly coupled wires, caused by the temperature, the thermal energy needed is  $e(V_{c1} + V_{c2})$  in the case of strongly coupled wires while it is only  $eV_{c1,2}$  for weakly coupled ones. This is easily understood because for strong coupling, one can simply consider the system as one wire with a larger blockade to which the thermal energy compares.

Another interesting result is the limitation towards very small blockades for too large resistors. For  $V_c < 0.1$  mV, the equivalent temperature is already below 1 K, and therefore, the impact of finite temperature and accompanying voltage noise from the large resistors can become very crucial in the experiment. For example, let us assume a strongly coupled system with a common threshold voltage of  $\approx 50$   $\mu$ V ( $V_{c1} = V_{c2}$ ,  $eV_c/k_B \approx 600$  mK) at zero gate voltage and serial resistors with  $R_1 = R_2 \approx 0.5$  M $\Omega$  (like in Ref. [HZ12]) and compare the resulting values with the simulations, shown in Fig. 2.16. Even at  $T \approx 5$  mK (equals  $T' = 0.2$  for this example), a measured  $V_c$  would be significantly reduced, and the transition to

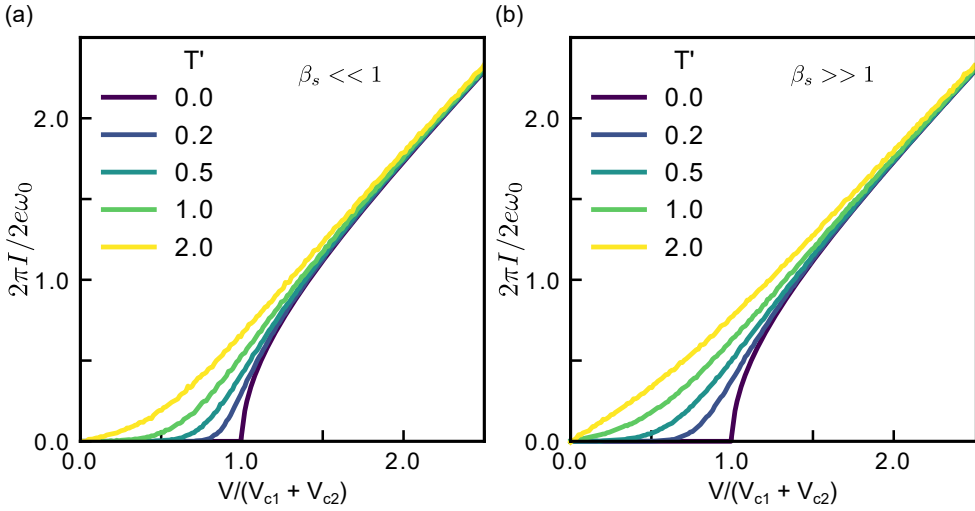


**Figure 2.16:** Simulated effect of finite temperatures on the  $I - V$  characteristics of a device with strongly (a) and weakly (b) coupled wires. The gate charge is set to zero ( $V_c^{\max}$ ) and it is assumed that both wires share the same critical voltage. The dimensionless temperature  $T'$  is defined as  $T' = 8\pi k_B T / e(V_{c1} + V_{c2})$ . The current is measured in units of  $\omega_0 = \pi(V_{c1} + V_{c2}) / e(R_1 + R_2)$ . For the same set of parameters, the strongly coupled system is less sensitive against voltage noise coming from the serial resistors. The simulations are taken from Ref. [EN21].

the current state would be smooth (for the present example, a value of 1 on the current axis would equal 50 pA). At  $T \approx 45$  mK ( $T' = 2$ ), the blockade has fully vanished. Consequently, too large resistors could be problematic when aiming for very small blockades/phase slip amplitudes. At this point, it should be noted that the question up to which temperature one can still expect coherent phase slips and how exactly the temperature dependence of the amplitude looks like must be considered independently of the considerations made before.

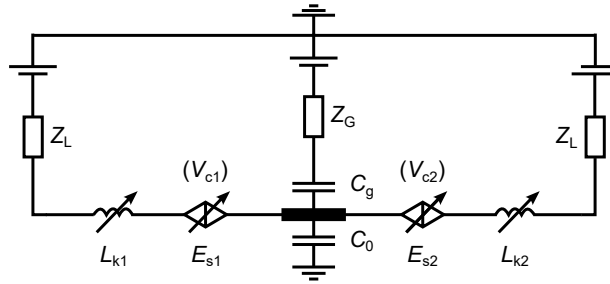


**Figure 2.17:** Simplified circuit representation of the interferometer:  $Z_L$ ,  $Z_G$  are the lead and gate impedances.  $L_{k1,2}$  and  $E_{s1,2}$  represent the kinetic inductances and the phase slip energies of the nanowires.  $C_0$  and  $C_g$  are the self-capacitance of the island and the gate capacitance.

## 2.12 Design considerations for a quantum phase slip interferometer

### 2.12.1 Circuit schematic

The key components for the interferometer design are two long ( $L_W \gg$  coherence length) granular aluminum nanowires which serve as QPS junctions and are strongly coupled by a small charge island. To decouple the device from its environment we use two high impedance on chip leads, made from the same layer of granular aluminum as the rest of the circuit (typically  $Z_L \approx 8 \text{ k}\Omega$ ). The decision not to use high resistors in the supply lines (as used for example in Refs. [APF21] and [HZ12]) leads, on the one hand, to very low damping in the system, but on the other hand, it prevents against thermal noise from the resistors and against overheating. This is important for the limit of small blockades and, therefore, for the investigation of the phase transition from insulating behavior to superconducting behavior by the interference of QPS, which is an important objective of this work.

Neglecting the parasitic capacitances and assuming perfect symmetry, except for the wires, the simplified circuit can be represented as shown in Fig. 2.17. Each wire ( $i = 1, 2$ ) is described by its phase slip energy  $E_{si}$  and its kinetic inductance  $L_{ki}$ .  $C_0$  and  $C_g$  are the self capacitance of the charge island and the gate capacitance. The arrows indicate the possible reduction of the phase slip amplitudes and inductances by using IEM to reduce the common normal state resistance of both wires [Vos+21]. Following Ref. [Moo+15], the characteristic phase slip energy  $E_{si}$  of each wires is

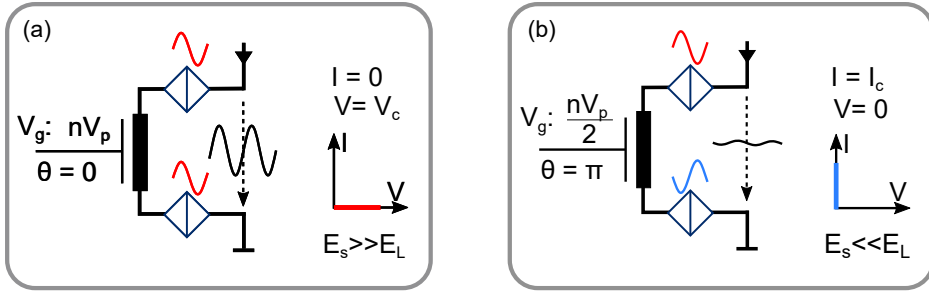


**Figure 2.18:** (a) Constructive interference: The induced charge equals  $n$  times  $2e$  ( $n \in \mathbb{N}_0$ ).  $V_g$  is the applied gate voltage,  $V_p$  the required voltage to induce a charge of  $2e$  and  $\theta$  the relative phase shift between the phase slips. (b) Destructive interference: The induced charge equals  $n$  times  $e$  ( $n \in \mathbb{N}$ ).

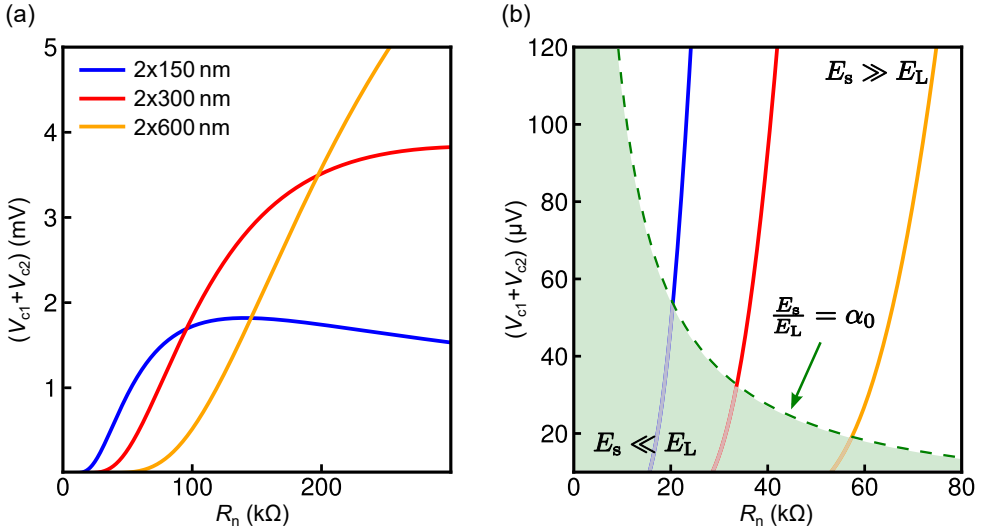
given by Eq. 2.76 and the inductance of the nanowire is fully dominated by the kinetic inductance and therefore given by Eq. 2.36.

Fig. 2.18 illustrates the gate controlled phase shift between both phase slip amplitudes  $A_i = V_{c_i} e^{iq_i \pi / e}$ . For  $Q_g = 2ne$  ( $n \in \mathbb{N}_0$ ),  $V_c$  becomes maximal, which corresponds to zero phase shift and therefore constructive interference (Fig. 2.18 (a)). The other extreme of maximal destructive interference is reached when  $Q_g = ne$  ( $n \in \mathbb{N}$ ). Here, the relative phase shift between the phase slip amplitudes  $A_i$  is  $\pi$ , leading to a reduced effective phase slip energy (Fig. 2.18 (b)).

For the following considerations we use the results of single wire experiments, presented in Sec. 6.1.7. For suitable parameters, the interferometer can be used to probe the insulating to metallic to superconducting transitions.

## 2.12.2 Parameters

Now we will discuss some important design parameters that are crucial for the behavior of the interferometer and its adjustability. The most important components are the nanowires. On the one hand, they define the possible phase slip amplitudes, and on the other hand, the available statistics for the  $R_n$  reduction with the IEM method (see Sec. 5.2). To get a feel for the influence of the wire length, we first assume a homogeneous circuit and strongly coupled wires ( $\beta_s \ll 1$ ). Thus, both wires have the same phase slip amplitude and the same kinetic inductance. For each wire, the phase slip energy is given by Eq. 2.76. It follows, that the common threshold voltage of two wires in series is  $V_{c1} + V_{c2} = 2\pi / e E_{s1} (R_{n1})$  with  $R_{n1} = R_{n2}$ . Fig. 2.19 shows the common threshold voltage as a function of the common normal state resistance for three different wire lengths. Fig. 2.19 (a) shows a larger resistance



**Figure 2.19:** (a) Threshold voltage vs. normal state resistance for different wire lengths.  $R_n = R_{n1} + R_{n2}$  is the common normal state resistance of both wires. For the calculation, it is assumed that both wires have the same resistance  $R_{n1} = R_{n2}$ . The accessible voltage range strongly depends on the wire length. Also the slopes for certain values of the threshold voltage are rather different. (b) Zoom in for small threshold voltages. The dashed green line marks a constant ratio between phase slip energy and inductive energy  $E_s/E_L = \alpha_0 = 0.02$ . For the various wire lengths, the same ratio is reached at different voltages/resistances.

range, while (b) is a zoom-in for small values. By comparing the different curves, we see that the choice of the wire length sets an upper but also a lower limit for the accessible blockades. The lower limit is defined by the transition between the different energetic regimes (from  $E_s \gg E_L$  to  $E_s \ll E_L$ ). The dashed green line in the right plot represents a constant ratio  $E_s/E_L \approx 0.02$ . It is that ratio, where we see the transition from insulating to metallic behavior for single wires. The slopes of the different curves are important for the adjustability through gradual resistance changes. In reality, of course, it can be assumed that both nanowires do not have exactly the same resistance. We, therefore, take a look at the effect of small inhomogeneities. The right panel of Fig. 2.20 shows the modulation strength ( $a = E_{s1}/E_{s2}$ ) as a function of the common normal state resistance  $R_n$  for different wire lengths, assuming inhomogeneities of ten and twenty percent. For larger resistances, the sensitivity to resistance differences is not so strong, but it highly increases when going to smaller  $R_n$  (resp.  $V_c$ ) values. Shortly before leaving the phase slip regime at  $E_s/E_L \approx \alpha_0$ , a difference of 10 percent in  $R_{ni}$  can reduce  $a$  by a factor of  $\approx 0.5$ . Apart from the energetic operating point, the sensitivity for certain  $R_n$  values also depends on the wire length. The crossings with the green curves

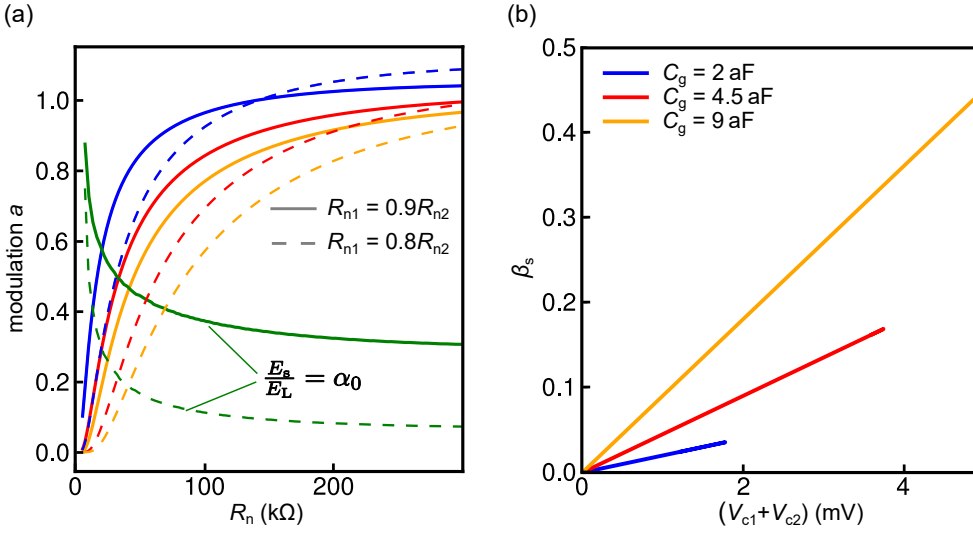


**Figure 2.20:** (a) Modulation strength  $a = E_{s1}/E_{s2}$  as a function of the common normal state resistance  $R_n$ . Here, a strong coupling  $\beta_s \ll 1$  and slightly different normal state resistances for both wires are assumed ( $R_{n1}/R_{n2} = 0.9$  (solid lines) and  $R_{n1}/R_{n2} = 0.8$  for the dashed lines). The green lines show a constant ratio for  $E_s/E_L$ . (b) Coupling parameter  $\beta_s$  as a function of the maximum threshold voltage. Here, the same resistance for both wires is assumed. The self capacitance  $C_0$  of the island is neglected. The different curves correspond to different wire lengths and different gate capacitances (2 aF, 4.5 aF and 9 aF).

indicate the resistances at which the transition ratio  $E_s/E_L \approx 0.02$  is reached. Here, we also find a significant change for different degrees of homogeneity.

Finally, we take a closer look at the coupling of the wires. For strong interference, the device should operate in the strong coupling regime ( $\beta_s \ll 1$ ). Since the coupling parameter describes the ratio between the island capacitances ( $C_0, C_g$ ) and the kinetic capacitances  $C_{ki}$  of the wires (scale with  $1/V_{ci}$ ), a change in resistance will also affect the coupling. The right panel in Fig. 2.20 shows  $\beta_s$  as a function of the common threshold voltage for different gate capacitances. For the calculation it is assumed that  $C_0 \ll C_g$ . Over the possible tuning range with the IEM method, from millivolts to microvolts,  $\beta_s$  can decrease by more than one order of magnitude.

### 3 Material and fabrication

Finding a suitable material for the investigation of quantum phase slip effects in superconducting nanowires is not trivial and, indeed, turned out to be a rather challenging task. In the phase slip model discussed in the previous section, it was shown that the quantum phase slip (QPS) amplitude highly depends on the material parameters (e.g. coherence length or normal state resistance) and on the wire geometry. Therefore, apart from finding a suitable material, also the fabrication process is very important as the required degrees of film homogeneity, reproducibility and lithography resolution are extremely high. This becomes even more crucial when dealing with systems in which more QPS junctions than one are involved. To address these important topics, the choice of material and the utilized fabrication techniques will be discussed in this chapter.

An important outcome of the quantum phase slip model is the exponential dependence of the phase slip rate on the normal state resistance of the wire. Hence, the material of choice should have a high sheet resistance  $R_{\square}$  in order to gain a substantial phase slip energy  $E_s$  which translates into the phase slip rate. Consequently, high kinetic inductance materials, such as niobium nitride (NbN), molybdenum germanium (MoGe) or indium oxide ( $\text{InO}_x$ ) turned out to be promising candidates for QPS experiments [Web+13; Ast+12; Gra+18; BLT00; Aru+12]. A specialty of these highly disordered superconductors is that they comprise two components and reveal a superconductor to insulator phase transition when going from low to highly resistive films. The specific properties of a film are extremely dependent on parameters like the ratio of compounds or the growth conditions. On the one hand, this allows one to vary the film parameters over a wide range, simply by adjusting the fabrication parameters (e.g. the partial pressure of the process gases), and therefore to fabricate films with sheet resistances up to a few kilo-Ohms, which still become superconducting below  $T_c$ . On the other hand the sensitivity of  $R_{\square}$  to fabrication parameters leads to unwanted effects such as a large resistance spread for different fabrication runs, pronounced  $R_{\square}$  drifts in time (aging effects) and strong fluctuations of  $R_{\square}$  for single films. Since the requirements to reach the phase slip regime ( $E_s \gg E_L$ ) are that the diameters of the wire should be of the order of the coherence length  $\xi$  and that the wire length  $L_w$  is much greater than  $\xi$ , these drawbacks become even more crucial. Thus, a precise control of the phase

slip energy is rather difficult and therefore was a limiting factor in the systematic exploration of phase slip phenomena in nanowires so far.

A possible strategy to get around these limitations to some extent, is by reshaping a single wire multiple times in order to change its phase slip rate. Prominent approaches are ion beam milling or classical electromigration [Zgi+08; Bau+16]. An ion beam milling application mainly reduces the wire thickness by physical sputtering. The major drawbacks of this approach are the need for sufficient protection for the surrounding structures during milling, and the fact that it can not be easily performed in-situ at low temperatures. However, it was demonstrated that it allows to significantly increase the phase slip rate for single devices stepwise [Leh+12]. In comparison to milling, the second example of controlled classical electromigration comes with the advantage that it can be performed in-situ at cryogenic temperatures. The idea behind this method is to treat a wire with a relatively high current (few mA) in order to create a narrow spot caused by the current ablation of material. As the current density in this spot increases extremely fast when reducing its dimensions, a fast feedback loop is required [Bau+16]. Therefore the controllability is rather low, and the exact shape of the narrow spot is undefined. Overall, both techniques allow to increase the phase slip rate of a wire or small segment in a more or less controlled manner, but due to the reshaping, effectively a new wire or, in case of electromigration, a new weak link is formed. Therefore these approaches are limited when investigating the dependency of phase slips on intrinsic parameters like coherence length or the specific resistance  $\sigma$ . To circumvent these restrictions we developed a new method for the modification of the intrinsic structure of granular aluminum nanowires, presented in chapter 5.

### 3.1 Granular aluminum

The superconducting properties of granular aluminum ( $\text{AlO}_x$ ) films are already a subject of research since the 1960s. In an early work by B. Abels and co-workers, it was found that the critical temperature of many superconductors, including  $\text{AlO}_x$ , can be increased by reducing the crystallite size [ACC66]. Practically, this was done by adding small amounts of oxygen to the chamber during the evaporation of various metals. By comparing electron diffraction patterns of pure and oxidized samples, a strong reduction of the average crystallite size was observed. Later, the relation between preparation conditions and superconducting properties of  $\text{AlO}_x$  thin films was studied in detail [CA68]. Surprisingly, it was found that  $T_c$  can reach values up to  $\approx 3.7\text{K}$  for highly oxidized films with grain sizes below 4nm and high normal state resistivities (compared to  $\approx 1.2\text{K}$  for pure

aluminum samples). However, a detailed understanding of this behavior and how it is related to the intrinsic structure of the films was missing so far. This changed with the experimental and theoretical work of G. Deutscher and co-workers in 1973 [Deu+73]. In their experimental studies, they observed a dome-like dependency between  $T_c$  and the normal state resistivity  $\rho$ . For highly resistive films, also a broadening of the superconducting transition together with the decrease in  $T_c$  was observed. Instead of simply assuming a homogeneous material, they introduced a model, where the inner structure is considered as a collection of weakly coupled grains. With an increased oxygen portion, the insulating barriers between the grains grow, leading to more and more decoupled grains. Following this approach, it is reasonable to describe the inter-grain matrix of such films at very low temperatures, where the aluminum is in the superconducting state, as a random network of Josephson weak links. The charge transport between the grains and thus the normal-state resistance are therefore strongly dependent on the thickness and distribution of the insulating barriers. Due to the nonlinear Josephson inductances of the coupled grains, the transport properties of granular aluminum films are inherently nonlinear. For larger structures with a large number of parallel grains, this non-linearity gets washed out and therefore is only visible at large electrical currents.

The  $\text{AlO}_x$  films studied in this work were prepared by reactive pulsed magnetron sputter deposition at room temperature (technical details are given in section 3.2). From transmission electron microscopy, the grain size for such films was determined to be between 3 nm and 4 nm, see Fig. 3.1 (a). The thicknesses of the films were  $\approx 20$  nm and typical values for the sheet resistance were several kilo-Ohms. Reported transition temperatures for such parameters are between 1.4 K and 2 K [Rot+16]. This stands in good agreement with a  $T_c$  of about 1.8 K observed in our experiments. The relatively high  $T_c$  comes with the advantage that the devices can be easily operated far below the transition to the superconducting state and therefore helps to avoid thermally activated phase slips and quasi-particle poisoning.

Due to the high sheet resistance of a few kilo-Ohms, the kinetic inductance  $L_k$  of a nanowire made of such a film may exceed the geometric inductance by orders of magnitude. Using Eq. 2.36 from Sec. 2.7, one finds typical values for the kinetic inductance per square of a few nH. The high kinetic inductance in combination with low intrinsic microwave losses [Rot+16; Grü+18], make granular aluminum thin films a versatile material for high impedance superconducting quantum circuits, such as kinetic inductance detectors [Val+19; Mal+18] or qubits [Sch+20; Grü+19].

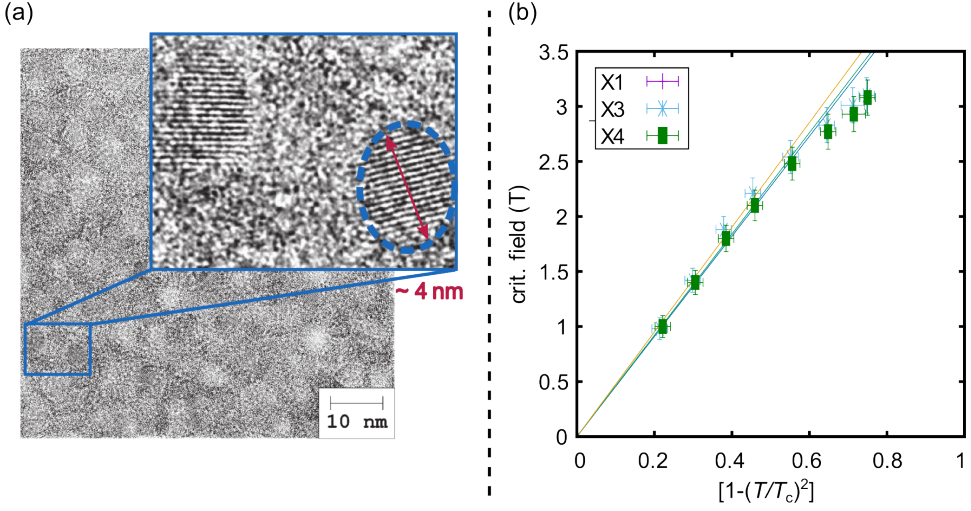


**Figure 3.1:** (a) Transmission electron microscope picture of a  $\sim 20$  nm thick granular aluminum film with  $R_{\square} \sim 2$  k $\Omega$ . The film consists of pure, crystalline aluminum grains (dashed oval in the inset), which are separated by thin oxide barriers (for more details see Ref. [Rot+16]). (b) Critical field  $H_{c2}$  vs. the reduced temperature  $1 - (T/T_c)^2$ . X1, X3 and X4 denote three 1  $\mu$ m wide  $\text{AlO}_x$  wires. The samples are made from films with different sheet resistances. Sample X1 has a sheet resistance of  $R_{\square}^{\text{X1}} = 2.0$  k $\Omega$ , X3 of  $R_{\square}^{\text{X3}} = 5.1$  k $\Omega$  and X4 of  $R_{\square}^{\text{X4}} = 4.5$  k $\Omega$ . The critical field  $H_{c2}$  is approximately the same for all samples at a certain temperature. Adopted from Ref. [Vos+21].

## Coherence length

To determine the coherence length of the films used, we have measured the critical field  $H_{c2}(T)$  for three 1  $\mu$ m wide  $\text{AlO}_x$  stripes with sheet resistances ranging from 2.0 k $\Omega$  to 5.1 k $\Omega$  (see Fig. 3.1 (b)). We found a constant  $H_{c2}(T = 0) = (4.5 \pm 0.2) \text{ T}/\mu_0$ , which is consistent with Ref. [DES80]. For a type 2 superconductor like the granular aluminum thin films studied here, the relation between  $H_{c2}(T)$  and the Ginzburg Landau coherence length  $\xi_{\text{GL}}$  is given by:

$$H_{c2}(T) = \Phi_0 / (2\pi\xi_{\text{GL}}(T)^2) \quad (3.1)$$

[Tin04]. Therefore  $\xi_{\text{GL}}(T = 0)$  is directly related to  $H_{c2}(T = 0)$ . With the universal relation:  $H_{c2}(0) = 0.69 T_c (dH_{c2}/dT)_{T=T_c}$  for a one-gap superconductor in the dirty limit (Werthammer et al., [WHH66]),  $H_{c2}(0)$  can be extracted from the slope of  $H_{c2}(T)$  at  $T = T_c$ . The critical temperatures were approximately 2 K for all samples. From the linear fits to the  $H_{c2}(T)$  measurements (see Fig. 3.1 (b)), together with the measured  $T_c$  values, we receive a coherence length  $\xi = 8 \pm 0.4$  nm. This result is in good accordance with the 10 nm value quoted in Refs. [Bac+15; Són+19].

## 3.2 Film deposition

The granular aluminum films studied in this work were deposited using reactive magnetron sputtering. In essence, pure aluminum is sputtered in a slight oxygen atmosphere, and the amount of incorporated oxide can be controlled by the oxygen partial pressure [Rot+16]. Compared to a simple thermal evaporation [Kun+87; CA68; Deu+80], this method comes with the advantage that the aluminum target can be cooled during evaporation, preventing it from deep contamination with oxygen. As tool, an in-house made deposition machine was used. It comprises two chambers, the load lock and the main chamber, which are separated by a gate valve. Therefore it allows to change a sample without breaking the vacuum of the main chamber. Apart from the sputter gun, the main chamber features a quartz oscillator to measure the evaporation rate, a shutter to protect the sample during conditioning (pre-sputtering of  $\sim 2$  min), and an electrode for plasma cleaning of the substrate surface (see Ref. [Vos17]). The pre-sputtering is performed not only for the conditioning of the chamber but also to remove the oxide layer that builds on the target surface after a previous sputter run. As sputter gas, we used argon. The sputtering process itself works as follows: A high voltage (of about 400 V) is applied between the target cathode (pure aluminum) and the ring anode of the sputter gun. In combination with the argon atmosphere in the chamber, this leads to the ignition of a plasma between anode and cathode ( $\sim 170$  W). Due to the electric field, ionized argon atoms are accelerated towards the aluminum target while electrons move to the anode. To increase the ionization probability for the argon atoms, permanent magnets are placed circularly underneath the aluminum target to force the electrons onto cycloid trajectories by a magnetic field. When the accelerated atoms hit the target surface, clusters of aluminum atoms are ejected by the transferred momentum. When these aluminum atoms are on their way to the substrate and condensate on its surface, oxygen from the chamber atmosphere is implemented into the growing film.

As explained in section 3.1, the properties of granular aluminum films are very sensitive to small variations in deposition parameters and the amount of implemented oxygen. Fig. 3.2 (a) shows the dependence of the sheet resistance on the argon partial pressure. By increasing the amount of argon in the atmosphere, the plasma density increases, resulting in a decreased sputter rate. Thus, more oxygen can be implemented, which leads to increased  $R_{\square}$ .

To enhance the controllability of the amount of oxygen in the chamber, an argon/oxygen mixture with a ratio of 9/1 was used and handled with a separate mass flow controller. The dilution of the oxygen with argon shifts the flow of the gas to higher values for the same amount of oxygen in the chamber. Additionally,

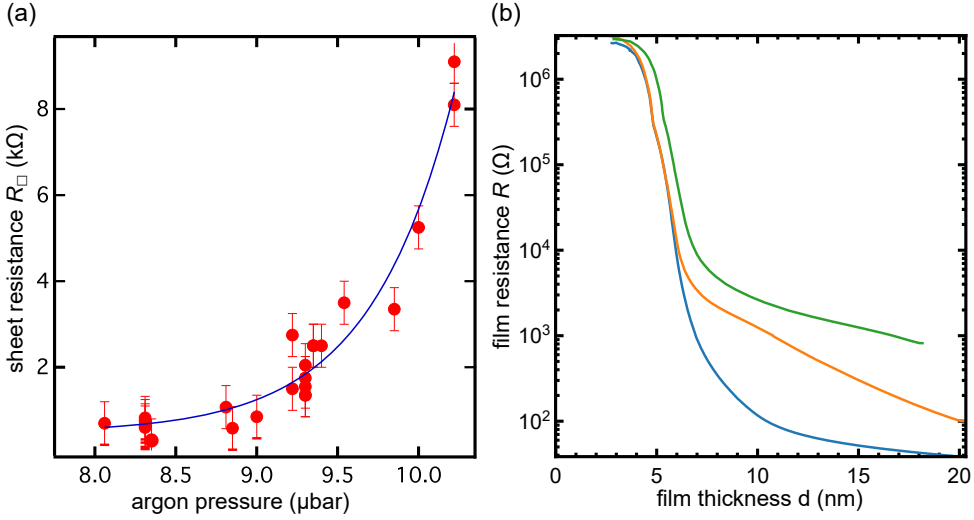


**Figure 3.2:** (a) Sheet resistance vs. argon partial pressure (from [Rot+16]). Instead of the argon flow, we varied the oxygen partial pressure. (b) Examples for the in-situ measurement of the film resistance during deposition (adopted from [Wil+22]). The monitoring allows for adjustment of the oxygen partial pressure in order to adjust the film sheet resistance in-situ.

the films were grown at low sputter rates ( $\sim 0.02$  nm/s) and the sheet resistance was measured in-situ, which allowed one to adjust the film sheet resistance by tuning the gas flow (see Fig. 3.2 (b)). For such monitoring, the  $20\text{ mm} \times 20\text{ mm}$  sapphire substrates were equipped with wedge-shaped silver stripes beforehand (for more details see Refs. [Wil+22; Sch21]).

### 3.3 Lithography process

For the experiments conducted in the framework of this thesis, we had several requirements for the fabrication processes. In order to study quantum phase slip effects in granular aluminum nanowires, the achievable resolution should be of the order of the coherence length to reach sufficiently high phase slip energies  $E_s$ . As discussed in section 3.1, the coherence length for the films we used is  $\approx 8$  nm. Therefore, the needed resolution is a few ten nanometers. Using granular aluminum as base material, it is also important that the process temperatures should be below  $200^\circ\text{C}$  in order to avoid unwanted changes in the film sheet resistance [Rot+16]. With respect to transport measurements, another requirement is to have low ohmic contacts with the structures. Thus, no dielectrics (like e.g. resist) that can cause

problems for bonding or lead to high ohmic contacts should remain on the circuits after fabrication.

To meet these requirements, we used two in-house developed electron beam based fabrication processes. For both approaches, we first grow the granular aluminum layer on top of a  $20\text{ mm} \times 20\text{ mm}$  ( $\approx 400\text{ }\mu\text{m}$  thick) sapphire substrate by reactive magnetron sputtering (as described in detail in Sec. 3.2). In both cases, Hydrogen silsesquioxane (HSQ) is used as negative e-beam resist, and the structures are transferred using anisotropic dry etch processes. The use of HSQ has the advantages that it allows for a high resolution and that it is very robust. After e-beam exposure, it forms a hard and glassy  $\text{SiO}_2$  layer, which serves as a hard mask during the etching processes. Its stability, indeed, is also its main disadvantage, as the resist can not be removed by an organic solvent after e-beam exposure. A chemical remover would also damage the underlying structures. Therefore different strategies are needed. A possible approach is to use a double layer stack containing a sacrificial layer to lift the HSQ after etching. For stacks made from poly-methyl-methacrylate (PMMA) and HSQ it has already been successfully demonstrated that this method achieves resolutions below  $20\text{ nm}$  [Rom+13; MT11]. The first process used for fabricating the samples followed this approach. To increase the reliability and yield, a second process was established, which uses, instead of a sacrificial resist layer, a thin metal layer for protection and as an etch stop [Sch21]. Both processes are explained below. Details about the process parameters can be found in the appendix A.

### First process (Fig. 3.3 (a)):

Before the sputter deposition of the metal film (details in Sec. 3.2), the  $20\text{ mm} \times 20\text{ mm}$  sapphire substrates were cleaned with piranha solution. In a next step an about  $30\text{ nm}$  thick layer of PMMA is spin coated on top of the granular aluminum film (bake-out temperature  $\approx 160\text{ C}$ ). To prevent intermixing between the HSQ and the PMMA, a  $\sim 3\text{ nm}$  thick layer of oxidized aluminum is added by thermal evaporation. Then, the about  $50\text{ nm}$  thick layer of HSQ is spun on (bake-out temperature  $\approx 200\text{ C}$ ). For electron beam exposure, a  $50\text{ keV}$  JEOL JBX-5500ZD machine from the Nanostructure Service Laboratory at KIT was used. The next step is to develop the HSQ, using MIF 726. In this step, also the thin aluminum oxide protection layer is removed by the TMAH in the developer, except for the areas which are protected by the exposed HSQ. To remove the PMMA everywhere besides the written structures, an argon/oxygen ( $15\text{ sccm}/15\text{ sccm}$ ) based dry etch process is carried out (using an inductively coupled plasma etching tool Oxford ICP180). The great etch selectivity between the HSQ and the PMMA ensures that in this

step, mainly the PMMA is removed. This process is followed by an argon/chlorine (12 sccm/12 sccm) process in which the imprint of the imaging mask is transferred into the granular aluminum layer (etch rate  $\approx 0.3$  nm/s). During this process, the PMMA layer experiences quite some stress which can reduce the yield (for details, see [Sch21]). In the last step, the HSQ is lifted by removing the PMMA with NEP.

### **Second process (Fig. 3.3b):**

For the second process, a different strategy is used to remove the HSQ after defining the structures. In essence, the idea is to etch the HSQ away once the structuring is completed. Instead of PMMA and a thin protection layer of oxidized aluminum, in this process, only a thin ( $\sim 3$  nm) layer of high ohmic niobium is evaporated on top of the granular aluminum film. The HSQ is then directly spun onto the niobium layer (bake-out temperature  $\approx 200$  C). After e-beam exposure, the resist is developed using MIF 726. Here, the niobium layer protects the granular aluminum film against the TMAH in the developer. The structure is then directly transferred by an argon/chlorine (12 sccm/12 sccm) dry etch process (the same as in the first process). Finally, the remaining HSQ and the niobium layer are removed using a CF<sub>4</sub> plasma (used device: Sentech SI 220 Plasma Etcher). Oxidized aluminum has a high resistance towards fluorine and therefore is only barely affected by this last step (for more details about this process, see Ref. [Sch21]).

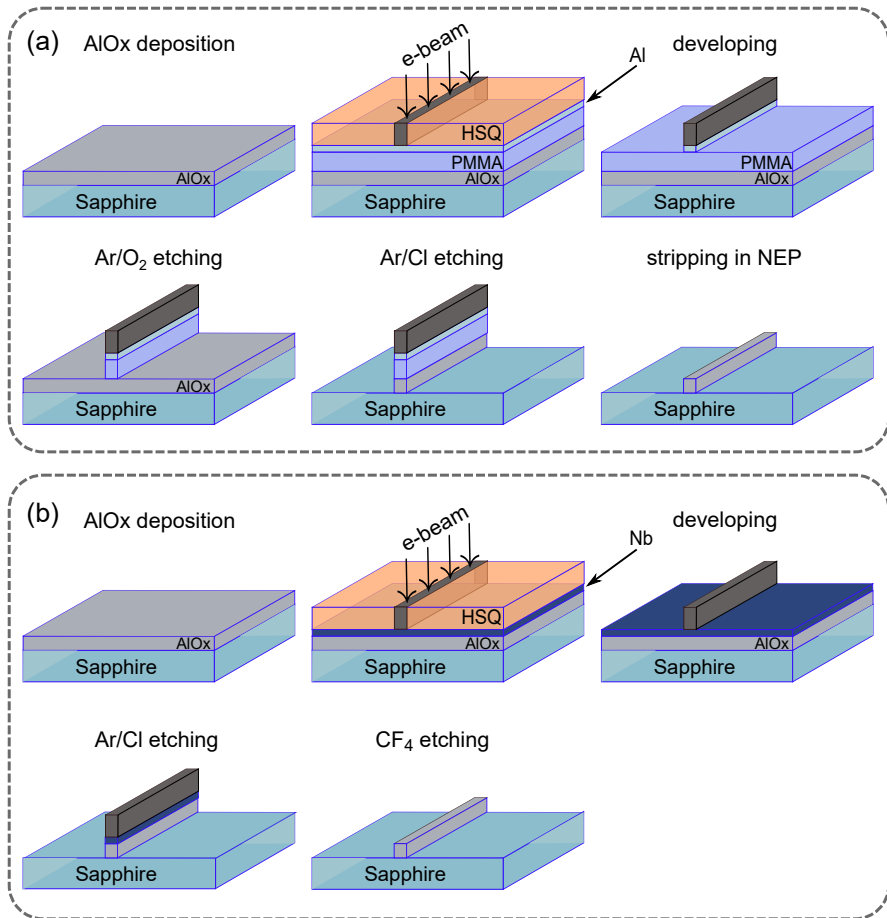


**Figure 3.3:** Illustration of the electron beam based fabrication processes, used to fabricate the nanowire circuits. **(a)** Three-layer stack approach: First, the granular aluminum layer is deposited by sputter deposition. Next, layers of PMMA, pure aluminum and HSQ are added. After e-beam exposure, the HSQ is developed using MIF 726. In this step, also the Al layer is removed by the TMAH. In a first etch step, the uncovered PMMA is etched away using an Ar/O<sub>2</sub> based dry etch process. To transfer the structures into the AlO<sub>x</sub> film, an Ar/Cl based process is used. Finally, the remaining stack on top of the structures is removed using an organic solvent (like NEP) **(b)** Double layer stack approach: After the deposition of the metal film, a thin layer of niobium is added by thermal evaporation (serves as protective layer for the granular aluminum during the development of the HSQ with TMAH developer). Then, a layer of HSQ is applied and developed after e-beam exposure. In the next step, the structure is transferred into the Ar/O<sub>2</sub> film using an Ar/Cl process. The remaining HSQ and niobium layer is then removed using a fluorine plasma.



## 4 Experimental methods

This chapter first gives an overview of the setups and measurement methods used. Then, some general considerations about the design for the various experiments and an overview of the chip layouts are presented. Essentially, the experiments carried out within the framework of this thesis can be subdivided as follows. First, single wire experiments were performed to investigate the relationship between the transport properties of granular aluminum nanowires and quantum phase slips. In particular, gradual resistance effects were studied. In a further step, the influence of temperature changes on wires with a pronounced phase slip rate was studied. The knowledge gained in these single wire experiments was then used to build a quantum phase slip interferometer. The experimental results will be explained in detail in chapter 6. However, in the course of the following explanations, some more technical details for the various experiments will be presented.

### 4.1 Cryogenic setup

For the investigation of quantum phase slips, it is important to work at temperatures far below the critical temperature. This is especially crucial when the characteristic energies ( $E_s$  and  $E_L$ ) are rather small and become comparable to the thermal energy. For example, a Coulomb blockade of  $20 \mu\text{V}$  corresponds to a temperature of  $\sim 200 \text{ mK}$  only. To account for these circumstances, special care was taken for the filtering and the cryogenic setup. In the following, the cryogenic setup, the measurement schemes, and the sample boxes used will be presented.

To reach low temperatures, we employed a commercial BlueForce Cryogenics BF-LD-250 dilution refrigerator, allowing for base temperatures below  $20 \text{ mK}$ . A schematic illustration of the basic operation principle is shown in Fig. 4.1. For pre-cooling, a two-stage pulse cooler is used. The operation principle can be seen as inverse to the Stirling engine. Inside a tube, heat exchangers and a regenerator (gas permeable material with a high heat capacity and large surface) are placed. With an external compressor,  $4\text{He}$  is periodically moved forward and backward. The cooling power is generated from the periodic expansion and compression of

the gas. During the expansion, the gas passes through the regenerator and absorbs heat. To transfer the heat, a heat exchanger is placed next to the regenerator. An important feature of the pulse tube is that it does not have any moving components at the cold part. Therefore, it introduces only very little vibrations to the rest of the cryostat. The achievable temperature limit for this pre-cooling unit is  $\sim 4$  K. The cooling mechanism of the actual cryostat is based on the  $^3\text{He}/^4\text{He}$  mixture phase transition and allows to reach temperatures below 20 mK. A sketch of the closed cooling cycle is shown in Fig. 4.1 (clockwise circulation). After pre-cooling, the mixture flows through the Joule-Thomson valve, where it is cooled due to isenthalpic expansion. Below  $\approx 0.8$  K, the condensed mixture then separates into two phases: A  $^3\text{He}$  rich phase and a  $^3\text{He}$  poor phase. For lowest temperatures, the  $^3\text{He}$  rich, concentrated phase almost exclusively consists of  $^3\text{He}$ , while in the  $^3\text{He}$  poor, diluted phase, only a share of about 6.5 percent of  $^3\text{He}$  remains. The difference in density between the rich and the poor phase leads to a horizontal separation of both phases. On the other side of the cycle, a reservoir pot is placed at the still stage ( $\sim 700$  mK) and connected via a tube with the dilution phase in the mixing chamber. In the still chamber, the temperature is increased by heating, and the pressure is lowered by pumping. Due to its lower vapor pressure compared to  $^4\text{He}$ , mainly  $^3\text{He}$  is vaporized. The outflow of  $^3\text{He}$  from the diluted phase is compensated by  $^3\text{He}$  diffusion from the rich phase into the mixed phase. The required mixing enthalpy is extracted from the environment as heat.

For the temperature sweeps, we used an in-house made temperature stage which is mounted to the base plate of the cryostat (see right panel of Fig. 4.2). To thermally decouple the stage, the sample plate is connected via hole tubes made from stainless steel with the base plate. To enhance the cooling power slightly, the tubes are covered with copper band. The thermometer is placed right next to the sample. With this configuration, it is possible to increase the sample temperature above  $\sim 3$  K, while the base temperature only goes up to  $\approx 80$  mK.

## DC setup

A crucial part of transport measurements is careful filtering of the DC lines. To ensure a low noise impact on the samples, several noise-reducing devices are installed for all DC leads, going down from room temperature to the sample at  $\approx 25$  mK. An illustrative drawing of the filtering scheme, described below, is presented in Fig. 4.1. In total, the cryostat hosts 3 DC measurement lines, with each having 24 DC cables. The filter scheme is as follows: First, the signals are filtered by  $\pi$ -filters (cut-off frequency  $\sim 10$  kHz) at room temperature, then followed by RCR-low pass filters at the 4K stage of the refrigerator. As material for the

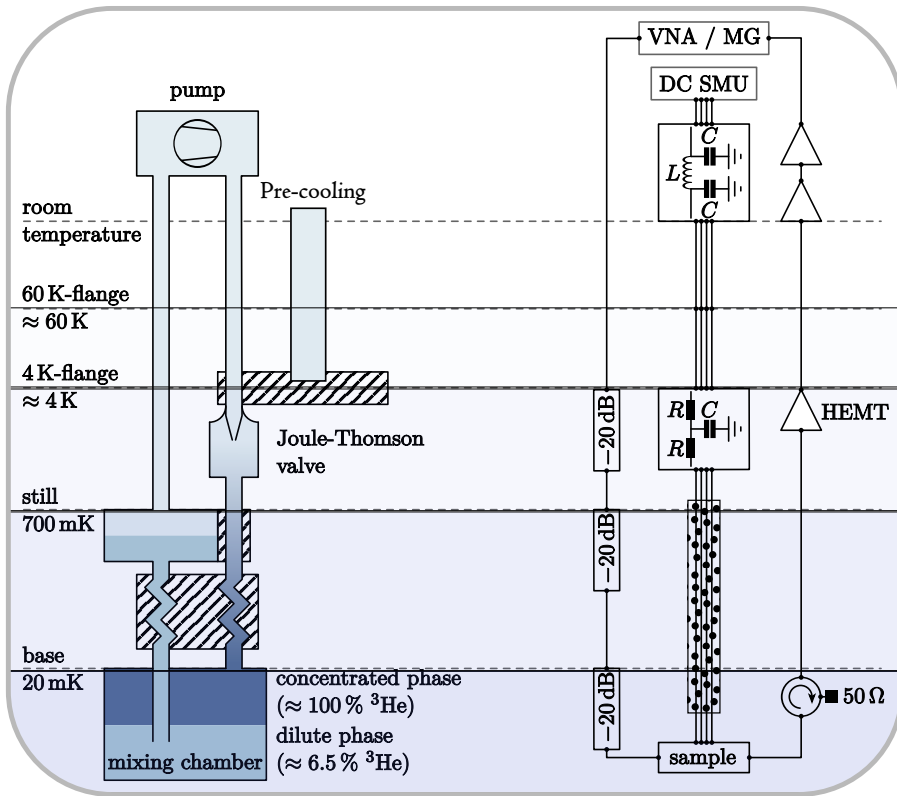


**Figure 4.1: Measurement setup:** On the left side of the sketch, the main elements and temperature stages of the dilution refrigerator are illustrated. For pre-cooling, a pulse tube is used (not included in the drawing). The working principle of the cryostat is explained in the main text. The wiring and the filtering scheme are presented on the right side. The dotted area around the leads represents the copper powder filters. The drawing is taken with permission from Ref. [Wil22] and modified.

cables, we first use high ohmic CuNi (as twisted pairs from 300 K to 4 K) and then superconducting niobium-titanium ribbon cable (from 4 K to sample holder). The resulting measurement bandwidth is  $\sim 5$  kHz. In the insulating regime, however, the  $I - V$  characteristics are measured for a better signal to noise ratio with a minimal sampling time of about 0.02 s. Additionally, to suppress high frequency noise, copper powder filters of a length of several meters are installed. Since the currents required for a resistance change by intrinsic electromigration are relatively small (usually between  $\sim$  nA and  $\sim 100$   $\mu$ A) we can use the described leads also for the in-situ tuning of the wire resistances.

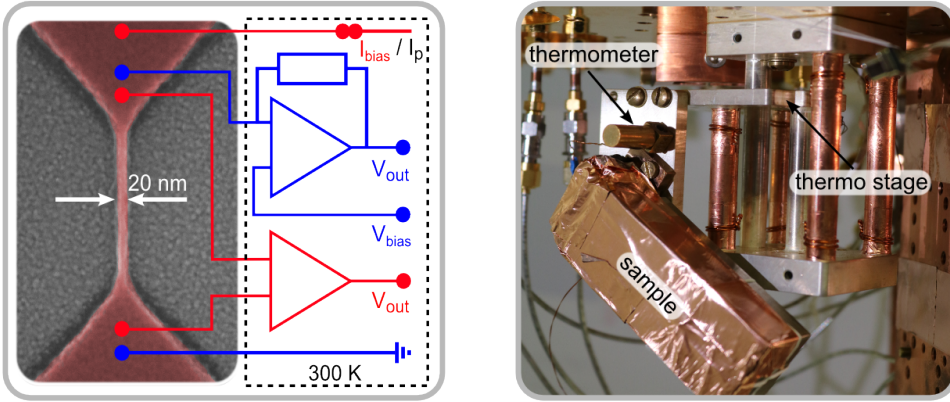


**Figure 4.2:** **Left:** Illustration of the bias schemes used to measure the  $I - V$  characteristics and to reduce the normal-state resistance of the wires. Either the current bias scheme (red) or the voltage bias scheme (blue) was used. To automatize the switching between the bias schemes, we implemented several computer-controlled relays.  $I_p$  represents the applied pulse for the reduction of the wire resistance with the IEM method (see chapter 5). **Right:** Picture of the in house made temperature stage. The stage is mounted to the base plate and thermally decoupled by stainless steel tubes. The thermometer is placed directly besides the sample.

For the transport measurements, we use different bias schemes, depending on the regime in which the circuit operates. Fig. 4.2 shows a typical schematic diagram of the bias schemes: To record the  $I - V$  characteristics in the metallic and superconducting regime, a current bias scheme was used (depicted in red). As current source ( $I_{\text{bias}}, I_p$ ), we use a voltage-controlled, in-house made tunnel electronic which uses a Texas Instruments OPA2111 operational amplifier and current dividers as main elements. Additionally, for small bias values (below 10 nA), an extra voltage divider (1/10) is placed between the voltage source and the tunnel electronics. The input voltage signal is generated by a Keithley 2636A source meter and pre-filtered by a Stanford Instruments SR560 preamplifier. For the amplification of the output signal ( $V_{\text{out}}$ ), a low-noise instrumentation amplifier INA 105KP is used. The output signal is then filtered by a Stanford Instruments SR560, before it is measured with the second channel of the source meter. To reduce and measure the normal-state resistance, we directly used the output and input line of the source meter (without tunnel electronic and amplifier).

To measure samples in the insulating regime with pronounced Coulomb blockades, we used a voltage bias scheme (see blue circuit in Fig. 4.2). Here, one side of the sample is set to ground while on the other side, a FEMTO transimpedance amplifier (DDPCA-300) is applied. Just as for the current bias, the input voltage signal ( $V_{\text{input}}$ ) is generated by a Keithley 2636A and then filtered by a Stanford SR560. For small

blockades ( $< 0.4$  mV), we added a voltage divider (1/1000) between the voltage source and the transimpedance amplifier. The output signal ( $V_{\text{out}}$ ) is measured in the same way as described before.

## Sample holder

For all of our experiments, we used the same type of in house made sample holder. Fig. 4.3 shows pictures of the sample holder and the shields used to protect against external magnetic fields. The body of the sample box is made from copper. Inside the box, a printed circuit board (PCB) is screwed tightly to the sample holder, which features 24 DC supply lines for the transport measurements. To connect the box with the filtered DC leads, we use micro D metal (MDM) connectors. For the microwave experiments, two additional PCBs with impedance matched feedlines are mounted on opposite sides of the chip. Here, sub-miniature pushon (SMP) jacks are used to connect with the microwave input and output lines. The box is designed to host one  $5 \text{ mm} \times 5 \text{ mm}$  sample. To provide proper grounding for the backside electrode of our samples, we use conductive silver glue to mount the sample. After the sample preparation, the box is closed with a copper lid, put into a lead shield and successively inside a cryoperm shield to protect the experiment against external magnetic fields.

## 4.2 Chip layout and general design considerations

### Chip layout

As mentioned in Sec. 3.2, we use  $20 \text{ mm} \times 20 \text{ mm}$  sapphire substrates as the basis for our experiments. After the fabrication, the chip is diced into nine  $5 \text{ mm} \times 5 \text{ mm}$  chips. In the course of our work, small adjustments were made to the sample design. The main features of the chip layout are discussed below. The basic design of the experiments and important parameters are discussed together with the measurement results in the next chapter.

Fig 4.4 shows the two different  $5 \text{ mm} \times 5 \text{ mm}$  layouts we used for our experiments. The included structures can be classified as follows: (1) Single wire transport measurements, (2) Quantum phase slip interferometer, (3) Quantum phase slip interferometer with readout resonator, (4) Serial nanowire test arrays, (5) Test double wire resonators. The focus of this work lies on the single-wire experiments and the interferometers.

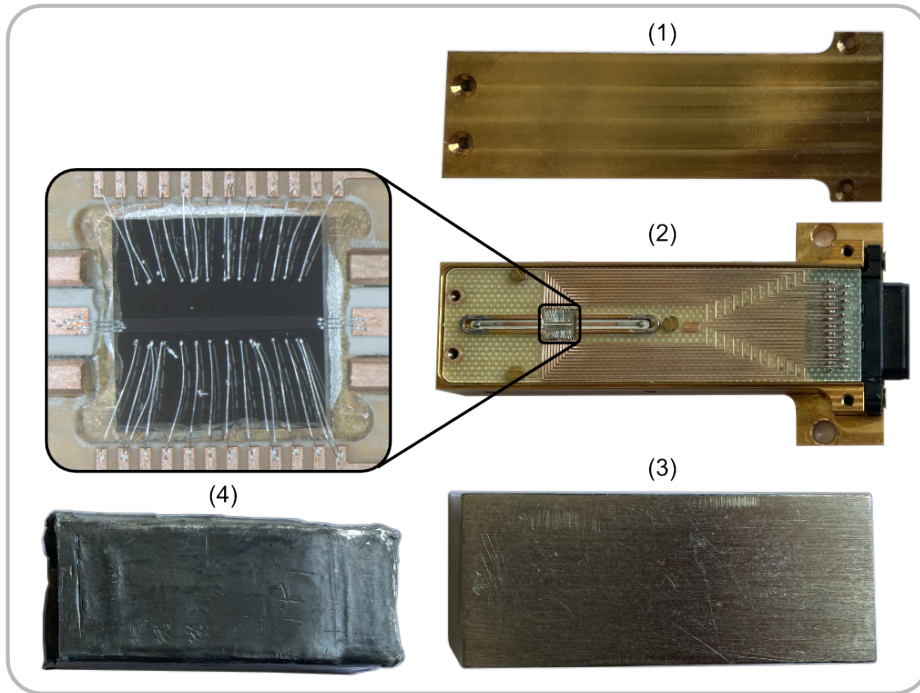


**Figure 4.3:** Sample holder and shielding: (1,2) Sample holder with lid. The zoom-in shows a mounted  $5\text{ mm} \times 5\text{ mm}$  chip. The surrounding PCB features 24 DC lines. The two PCBs on the left and right side provide feedlines for the microwave experiments. (3) Cryoperm shield. (4) Lead shield.

The blue line in the middle represents a  $\approx 100\text{ nm}$  thick and  $200\text{ }\mu\text{m}$  wide aluminum microwave microstrip feedline. During the fabrication, it is added by using standard optical lithography. This is being done after the rest of the chip has been patterned with the process described in Sec. 3.3. As backside ground plane, an aluminum backside metallization is added.

### 4.2.1 Single wire circuits

The design considerations for the single wire experiments are rather simple. In essence, the most important parameters for a high phase slip rate are sufficiently small cross-sectional areas and a high normal-conducting resistance. The different models for describing the phase slip rate were discussed in detail in Sec. 2.9.2. To recap the most important dependencies: The phase slip rate exponentially depends on the wire resistance and linearly depends on the wire length. The material of

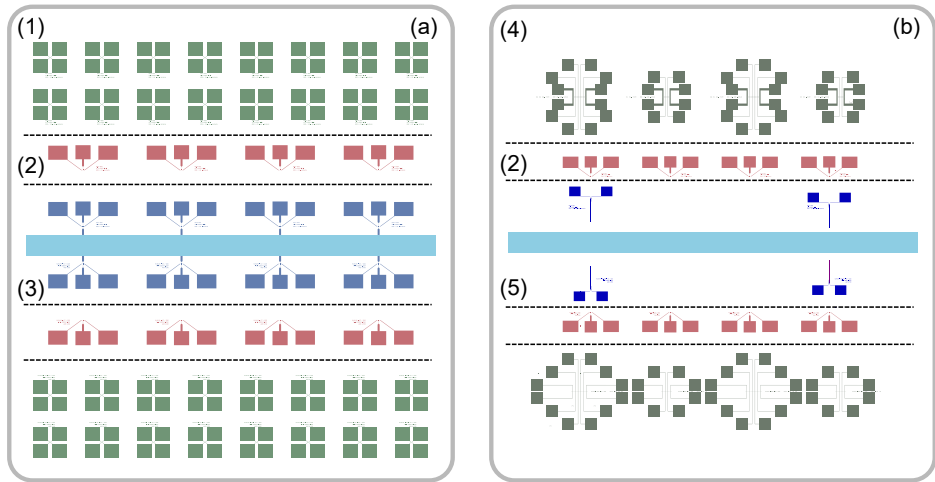


**Figure 4.4:** 5 mm  $\times$  5 mm chip layouts (a,b): Several experiments are hosted on the same chip. (1) Single wire transport measurements. Each column has a different wire length (ranging from 100 nm up to 1750 nm). (2) Phase slip interferometers. Here, the wire length  $L_w$  is varied between 300 nm and 1000 nm. Upper and lower line host samples with the same wire lengths but different island sizes. (3) Phase slip interferometers with readout resonator (4) Serial nanowire test arrays. (5) Test double wire resonators.

choice for our experiments are granular aluminum films with sheet resistances between 2 k $\Omega$  and 3 k $\Omega$  and a thickness of about 20 nm (see Sec. 3.1). For the wire geometries, we aimed for a fixed width of  $\approx$  20 nm and we varied the length of the wires from 50 nm up to 1000 nm.

A crucial part of the design are the on-chip leads and the direct environment of the nanowire. Here, a high impedance is favorable to effectively decouple the wire from the outer environment [ALR16]. The most common approaches to achieve the decoupling are high ohmic resistors (e.g. made from chromium) or high inductance leads. The former approach provides not only a high impedance but also a dissipation channel and therefore damping. However, it also can lead to overheating of the circuit and introduce Johnson noise at finite temperatures, which results in fluctuating voltage whose root mean square reads as:  $V_{\text{rms}} = (4k_BRTB)$  [Web+13]. Here,  $k_B$  is the Boltzmann constant,  $R$  is the resistance,  $T$  is the temperature, and  $B$  is the bandwidth of the circuit. Additionally, the fabrication process becomes more complex since at least one additional step is required. For the secondary approach one simply can make a wider, and long, segment from the same high kinetic inductance material which is used for the nanowires. Here it is important that this on-chip impedance is made wide enough so that phase slips from this part of the circuit are negligible. For our sample designs, we decided to

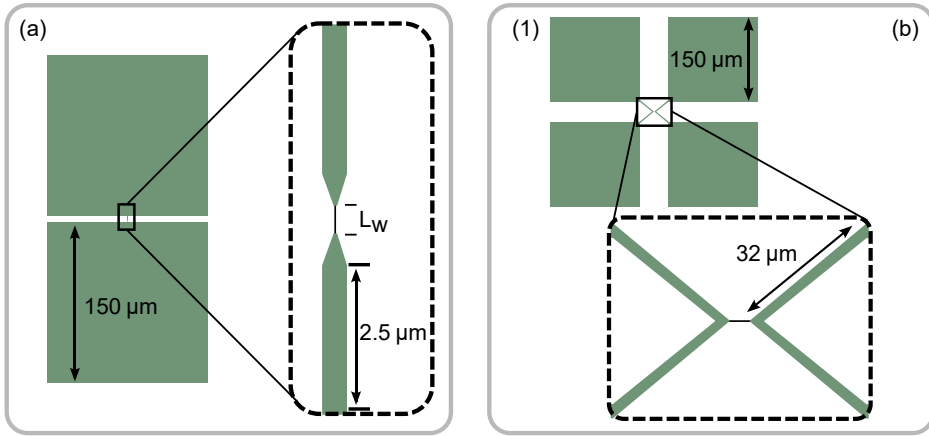


**Figure 4.5:** Designs for single wire experiments: **(a)** Initial, compact design. The rather large bond pads allow for 2W and 4W probes. **(b)** Modified design to increase the lead impedances and ease wire bonding for a four-point measurement. Both structures are fully made from a single layer of granular aluminum.

follow the second approach. To prevent strong impedance mismatches between the nanowires and the adjacent on-chip leads, we have added gradual narrowing to the nanowire width for all our experiments. In previous works, such impedance mismatch and the accompanying discontinuity in the number of quantum channels was seen as a possibility for coherent scattering at the boundaries, which could strongly affect the transport behavior of a wire [KR16].

The designs used for the single wire experiments are presented in figure 4.5. The left panel shows the initial design, which was later modified to increase the lead impedances and ease four-point probe bonding. For the first design, each nanowire has  $\text{AlO}_x$  leads with a width of  $0.5 \mu\text{m}$  and  $2.5 \mu\text{m}$  length, that contribute to an inductance of  $\approx 20 \text{ nH}$  (assuming a sheet resistance between  $2 \text{ k}\Omega$  and  $3 \text{ k}\Omega$ ). Together with a stray capacitance of about  $45 \text{ fF}$ , we estimate an environmental impedance of about  $0.6 \text{ k}\Omega$ , not considering the inductance of the nanowire itself. For the second design, the leads are  $2 \mu\text{m}$  wide and  $30 \mu\text{m}$  long. Here we estimate an impedance of about  $1.1 \text{ k}\Omega$  (assuming an inductance of  $\approx 60 \text{ nH}$  and a stray capacitance of about  $47 \text{ fF}$ ).

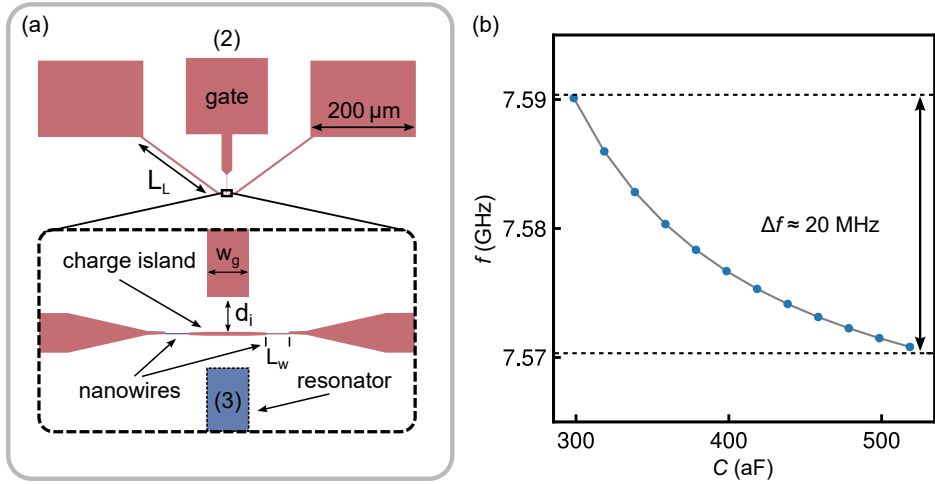


**Figure 4.6:** (a) Structural layout of the interferometers. Some of the devices have a readout resonator (see also Fig. 4.4). The coupling between gate and island / resonator and island is always designed symmetrically. (b) Simulated frequency shift of the readout resonator. The two nanowires are modeled by ideal capacitors, each having a capacitance of  $C/2$ . For the inductance per square  $L_{\square} = 1.6$  nH is used (corresponds to  $R_{\square} \approx 2$  k $\Omega$ ) and assumed to be the same for the whole structure.

## 4.2.2 Double wire circuits

The phase slip interferometer design is shown in figure 4.6 (a). The two large paddles on the left and right ( $150 \mu\text{m} \times 200 \mu\text{m}$ ) are used for two-probe or four-probe measurements. The pad in the middle is used for contacting the gate electrode ( $150 \mu\text{m} \times 150 \mu\text{m}$ ). In the following, typical design parameters are given.

The two high impedance leads have a length of  $L_L = 190 \mu\text{m}$  and are  $4 \mu\text{m}$  wide. The connection line to the charge island is  $13 \mu\text{m}$  long, and  $1 \mu\text{m}$  wide. This results in  $\approx 60$  squares for each lead (without the squares for the gradually narrowing to the nanowire). Assuming a sheet resistance of  $\approx 2.5$  k $\Omega$ , this gives a total kinetic inductance of  $L_k^L \approx 1.4 \mu\text{H}$ . The stray capacitances of the leads and constrictions are  $C_L \approx 17$  fF and  $C_c \approx 0.75$  fF. These numbers give an environmental impedance of about  $Z_L \approx 8$  k $\Omega$ , not considering the inductances of the nanowires itself. The wider segment of the gate lead is  $75 \mu\text{m}$  long and  $21 \mu\text{m}$  wide, the narrow part is  $35 \mu\text{m}$  long and  $1 \mu\text{m}$  wide. Here, the impedance is  $Z_G \approx 7$  k $\Omega$ .

As variation parameters for the realization of different coupling strengths between the gate electrode and the island, we have chosen the size of the island ( $1.5 \mu\text{m} \times 0.11 \mu\text{m}$  and  $1 \mu\text{m} \times 0.1 \mu\text{m}$ ), the distance to the electrode  $d_i$  ( $800$  nm and  $900$  nm), and the width of the electrode  $w_g$  ( $800$  nm and  $900$  nm). For samples with a readout

resonator, the thinning at the end of the resonator was altered symmetrically with the gate electrode. Also, the coupling distance is chosen to be the same. From numerical simulations, we get gate capacitances of  $C_g \sim 60$  aF and  $C_g \sim 30$  aF. The wire length on both sides is always the same and varies between 300 nm and 1000 nm for the different devices. The  $\lambda/2$  readout resonators are simple stripe geometries with resonance frequencies between 6 GHz and 8 GHz, depending on the exact sheet resistance of the film.

To model the effect of a change in the kinetic capacitances of the nanowires on the resonance frequency of the readout resonator, Sonnet<sup>TM</sup> simulations were performed. The wires are modeled by ideal capacitors with a capacitance of  $C/2$ . Fig. 4.6 (b) shows the simulated resonator frequencies assuming an inductance per square of  $L_{\square} = 1.6$  nH and capacitances between  $C = 300$  aF and  $C = 540$  aF. For this simulation, the island size was  $1 \mu\text{m} \times 0.1 \mu\text{m}$ . The coupling distance  $d_i$  and the width of the gate electrode  $w_g$  were 900 nm.

# 5 Intrinsic electromigration (IEM)

## 5.1 Modeling a granular aluminum nanowire

As stressed in section 3.1, the distribution of barrier thicknesses and the grain morphology has a great impact on the specific properties of granular aluminum films. When formed to a nanowire, averaging effects are highly suppressed, and local variations become more important. In order to get a better sense of how this affects the electrical properties of a nanowire, a closer look at the internal structure is important. Therefore, in this section, a model is presented which allows one to make predictions of the nanowire resistance and device-to-device variations in good accuracy [Bar+22]. The main idea is to model the intrinsic junction network as randomly distributed resistors. Each inter-grain junction is represented by a resistance value in a Laplace matrix from which the resistance between two arbitrary grains can be calculated [BAR21].

Assuming a typical grain size between 3 nm and 4 nm (see 3.1), wire diameters of  $d \sim 20$  nm and wire lengths of a few hundred nanometers, a single wire will host a network of hundreds or thousands of isolated aluminum grains. Each pair of neighboring grains forms a Josephson S-I-S (Al/AlO<sub>x</sub>/Al) junction with a characteristic coupling energy  $E_j = \hbar/2eI_c$ , where  $I_c$  is the critical current,  $\hbar$  the reduced Planck's constant and  $e$  is the charge of an electron. For this junction type,  $E_j$  is linked to the normal state resistance of the junction  $R_n$  via the Ambegaokar and Baratoff relation

$$I_c = \frac{\pi\Delta}{2eR_n} \tanh\left(\frac{\Delta}{2k_B T}\right) \quad (5.1)$$

[AB63a; AB63b].  $k_B$ ,  $\Delta$  are the Boltzmann's constant and the superconducting gap, respectively (see also Sec. 2.6). Consequently, calculating  $I_c$  allows for a conversion to  $R_n$ . For each knot of the network,  $I_c$  is given by:

$$I_c = \frac{2\sigma en_s \hbar}{\delta m_e} \exp\left(\frac{S_{ij}}{\delta}\right) \quad (5.2)$$

[Chu+01; Bar+22]. Here  $n_s$  is the density of cooper pairs,  $m_e$  is the electron mass,  $\sigma$  is the interaction area between the grains,  $\delta$  is a characteristic constant of the

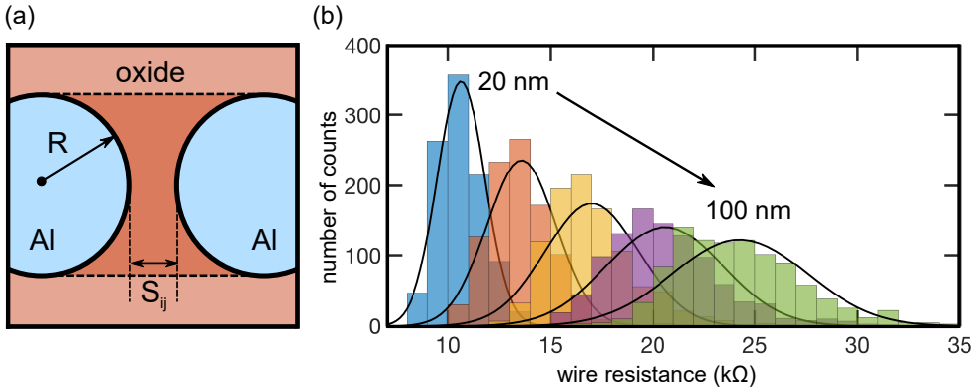


**Figure 5.1:** (a) Cross-section of two neighboring grains. It is assumed that all grains share the same radius  $R$  (2.5 nm).  $S_{ij}$  is the smallest distance between both spheres. The darker region marks the interaction area over which is integrated in the model. (b) Simulated device-to-device variation of the wire resistance for different wire lengths, assuming a constant width and thickness of 20 nm, represented as histograms. Each data set contains 1000 values. Adopted from [Bar+22].

dielectric.  $S_{ij}$  is the smallest distance between the grains (see Fig. 5.1 (a)). In the low temperature limit and assuming that  $R_n$  does not change significantly when going to cryogenic temperatures, the normal state resistance of a junction can be calculated by combining Eq. 5.1 and Eq. 5.2. As the microstructure of the granular aluminum films is rather uniform, it is reasonable to assume a constant grain size (5 nm) and a Gaussian distribution for the separation distance when modeling a whole wire (for more details, see Refs. [Bar+22], [BAR21]).

Fig. 5.1 (b) shows the resulting distributions of nanowire resistances, calculated for wires with different lengths [Bar+22]. Each histogram corresponds to a different wire length and contains one thousand simulated resistance values. For all calculations, the input parameters were kept constant ( $R = 0.25$  nm, standard deviation of separation distance 0.3 nm). There is a clear trend, that, when going from shorter to longer wires, the distribution broadens, resulting in a large wire to wire variation. At some point, for extremely long or very narrow wires, also open circuits become more likely. Another interesting aspect is the dependence of the 'effective' wire sheet resistance  $R_{\square}^e$  (wire resistance divided by the number of squares) on the length. The model predicts a linear increase as long as the wire diameters are large enough ( $\gg$  grain diameter). For extremely narrow wires, the resistance is fully dominated by fluctuations in single conductance channels, leading to strongly increased wire sheet resistances [BAR21]. These results overall agree well with the observations in our experiments. To give an example: A micrometer long nanowire, with diameters  $d \approx 20$  nm and made from a film with  $R_{\square} \approx 3$  k $\Omega$  revealed a

resistance ten times higher than expected from  $R_{\square}$ . Probably it is not mandatory to restrict the model to granular aluminum films, as many cermet materials have a similar intrinsic structure.

At first glance, the expected large resistance spread for longer wires seems to be problematic for a systematic investigation of QPS effects in single wires or when they are used as QPS elements in more complex circuits, because the parameter spread will be large. But surprisingly this problem can be turned into an advantage: A large statistic for the barrier thicknesses in combination with only very few parallel conductance channels can be beneficial for adjusting the resistance of a wire after the fabrication, using intrinsic electromigration (IEM).

## 5.2 Concept of IEM

A key element for the investigation and utilization of quantum phase slips in superconducting nanowires is a precise control over the electrical properties of the wire. The most common and natural approach is to do this by adjusting the geometry. This could ideally be achieved by a single fabrication, but more realistically by reshaping a wire multiple times (e.g. by ion beam milling) in order to readjust the properties after fabrication. For high kinetic inductance materials, such as granular aluminum, which are predestined as a basis for nanowires with high phase slip amplitudes, a limit for the controllability by geometry is set by the intrinsic disorder. As explained in Sec. 5.1, the combination of small diameters and small variations in the inner structure leads to fluctuations of the wire's normal state resistance, which affects the phase slip amplitude exponentially and the kinetic inductance linearly. Thus, the rather bad reliability of such devices i.e. strong wire to wire and batch to batch fluctuations, turned out to be a major problem for the systematic investigation and utilization.

These limitations have motivated us to develop a new technique, allowing to reduce the resistance of single wires by orders of magnitude in fine steps, in situ, and also at millikelvin temperatures. Due to its character, we named the method intrinsic electromigration (IEM). Current pulses with increasing amplitudes are applied to a wire in order to rearrange or short weakest links in its intrinsic network of Josephson junctions. With a current applied to the nanowire, the voltage will mainly drop over the oxide barriers. Above certain threshold currents  $I_p$ , the weakest barriers may break down, and neighboring grains are merged (e.g. by a movement of atoms at the grain boundaries [AR70; Bla69]). For single Josephson junctions, this is a well-known and studied phenomenon [TA08]. The suggested microscopical model is illustrated in Fig. 5.2. In contrast to widely used classical

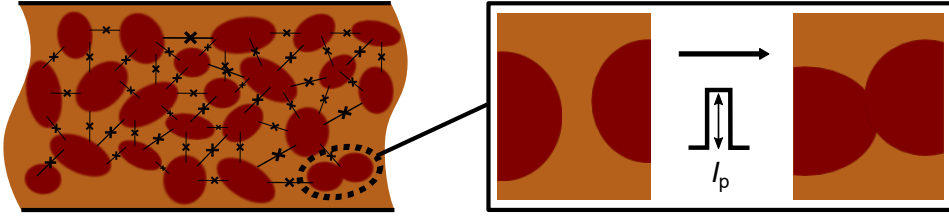


**Figure 5.2: Illustration of the proposed microscopic process:** The inner structure of a granular aluminum nanowire consists of pure aluminum grains (red, size  $\simeq 4$  nm), which are embedded in an aluminum-oxide matrix (orange), forming a random network of Josephson junctions (black crosses). The current pulses lead to an intrinsic electromigration process (IEM) merging grains and / or clusters of grains. From Ref. [Vos+21].

electromigration approaches (e.g. [Bau+16]), this method does not aim at a change of the macroscopic shape of the nanowire.

### 5.3 Modeling IEM as the formation of microscopic quantum point contacts

For single Al/ $\text{AlO}_x$ /Nb junctions, the gradual breakdown of the insulating barrier when stressed with currents  $I \gg I_c$  is known and can be explained by the formation of quantum point contacts (QPC) [TA08]. Above a critical applied voltage  $V^c$ , with a further increase of the voltage, more and more of these nano shorts in the junction are introduced by the movement of oxygen atoms. In the normal resistive state, this manifests as a reduction in resistance. In the superconducting state, it manifests as an increased critical current and a change of the I-V characteristics (e.g. occurrence of sub gap features, for details see [TA08]). As for intrinsic electromigration, the junctions are treated similarly, and a change in resistance is observed, it might be justified to adopt the model from Ref. [TA08] to IEM and combine it with the resistor network model [Bar+22; BAR21]. The condition for the formation of N QPC can be derived from the ionic current density for classical electromigration:

$$N = Bt \sinh(V_{ij}/V_{ij}^c) \quad (5.3)$$

[CM49; TA08; Bar+22].  $B$  is a temperature-dependent parameter (essentially describing the heat driven movement of ions),  $t$  is the stress duration,  $V_{ij}$  is the voltage across two neighboring grains.  $V_{ij}^c = (k_B T S_{ij}) / (qa)$  with the Boltzmann constant  $k_B$ , the temperature  $T$ , the activation distance  $a$ , the ion charge  $q$  and the separation

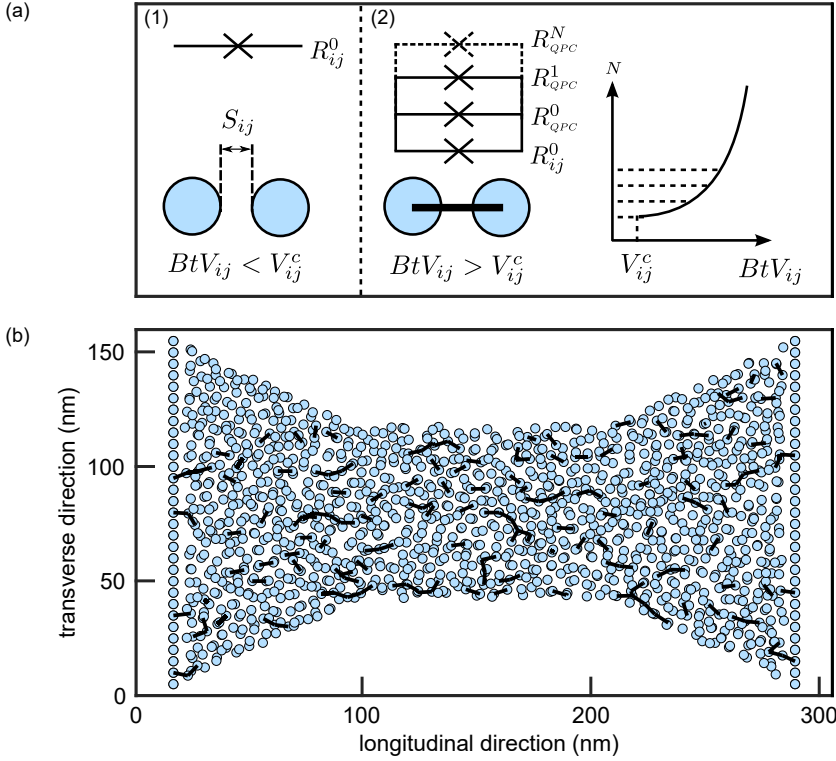


**Figure 5.3:** (a) Condition for the formation of QPCs: (1) For  $BtV_{ij} < V_{ij}^c$ , no shorts are created, and the spheres are represented without a black connection. (2) If  $BtV_{ij} > V_{ij}^c$ ,  $N$  parallel channels are created, each having a resistance of  $R_{QPC}$ . These junctions are represented by the black lines, connecting two neighboring grains. The increase of the number of QPCs  $N$  with the voltage across the barrier and stress duration is illustrated on the right side. For details see Ref. [TA08]. (b) Illustrative example for a simulation of the formation of QPCs (from Ref. [Bar+22]). It shows the cross-sectional view of a 3D simulation, where an applied current of  $I_p \approx 220 \mu\text{A}$  was assumed. The black lines between the grains represent junctions where QPCs were formed by the current stress.

distance between the grains  $S_{ij}$ . It is assumed that a single displacement of an ion leads to one QPC and therefore adds a conductive channel with resistance  $R_{QPC}$ . Therefore  $N$  is rounded down to integers. Consequently, for  $BtV_{ij} > V_{ij}^c$ , at least one additional channel is added, which can be seen as a parallel conductance channel, reducing the resistance across two adjacent grains (see Fig. 5.3 (a)). Mathematically, the voltage drop across inter grain junctions can be calculated using a matrix representation of Ohm's law with Kirchoff's current law and the Moore-Penrose pseudoinverse together with the resistance matrix, described in Sec. 5.1[Bar+22; BAR21]. For relatively small applied currents/voltages, one can use small angle

approximation to rewrite Eq. 5.3 in the form:

$$N = \frac{Btaq}{k_B T} \frac{V_{ij}}{S_{ij}} \quad (5.4)$$

[Bar+22]. Fig. 5.3 (b) shows a cross section view of the simulated formation of QPCs for a wire with a length of 100 nm, a width of 75 nm and a thickness of 10 nm [Bar+22]. The black connections between certain grains represent the QPCs which have formed after an applied current pulse of  $I_p \approx 220 \mu\text{A}$ .

## 5.4 IEM results

In the course of this work, the IEM method has been successfully applied to more than a hundred samples. In the following, we present the results for two selected wires ( $L_w = 1000 \text{ nm}$  and  $L_w = 250 \text{ nm}$ ) and give a summary of some general observations.

The altering procedure was carried out as follows: In a first step, a tuning pulse with a duration of  $t_p = 20 \text{ ms}$  was applied. Next, after a couple of minutes waiting time to let the system go back into thermal equilibrium, a test pulse with an amplitude of 300 nA and a duration of 50 ms was applied to determine the new resistance value.

Figure 5.4 shows two data sets of the wire resistance recorded at 25 mK vs. the amplitude  $I_p$  of current pulses which were stepwise increased upwards [Vos+21]. Both wires were shaped from the same granular aluminum film with an average sheet resistance of  $R_\square \approx 2.7 \text{ k}\Omega$ . We have applied current pulses with increasing amplitudes ranging from  $I_p \simeq 1 \mu\text{A}$  to  $I_p \approx 400 \mu\text{A}$  in more than 200 steps to both wires. Once some critical  $I_p$  value is reached, and the weakest link in the wire breaks down, the wire resistance drops to a lower value which is dictated by another slightly stronger weak link. This step-like behavior is visible in the inset of Fig. 5.4 (a). Once a reduction of  $R_n$  at a certain threshold current  $I_p$  is observed, applying pulses with an amplitude below the next threshold does not change  $R_n$ .

For the one micrometer long wire, the resistance was reduced from initially about 900 k $\Omega$  to only a few kilo-Ohms, for the 250 nm long wire it was still reduced roughly by a factor of ten (12.4 k $\Omega$  to 1.5 k $\Omega$ ).

The current pulses can be either applied at low temperatures (as in the case of the present examples) or at room temperatures with very similar results. In both cases, the change in resistance is permanent. For samples that were tuned at low temperatures,  $R_n$  also remained stable after thermal cycling of the cryostat to room

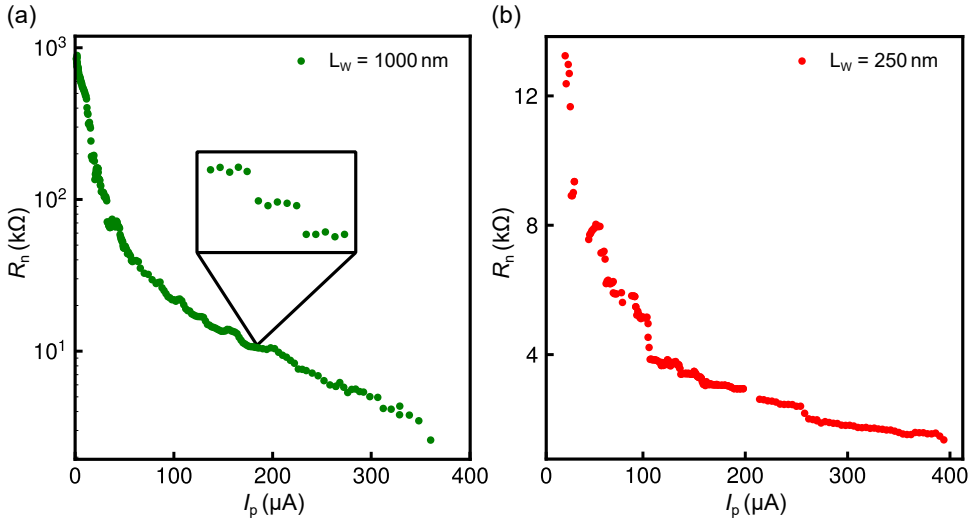


**Figure 5.4:** Normal state resistance of a 1000 nm long (a) and a 250 nm long (b) nanowire as a function of the applied pulse current  $I_p$ , measured at 25 mK. Both wires are  $\sim 20$  nm wide and were fabricated from a film with  $R_{\square} \approx 2.7$  k $\Omega$ . For the 1000 nm long wire,  $R_n$  was lowered from 900 k $\Omega$  to 2.5 k $\Omega$ , for the 250 nm long wire from 12.4 k $\Omega$  to 1.5 k $\Omega$ . In the beginning, the resistance steps are rather steep, but with a further reduction, the height of the steps decreases. Figures adopted from Ref. [Vos+21]

temperature. For longer time scales, like days or weeks, no aging effects were observed. In order to investigate the influence of the pulse duration on the change in resistance, we applied pulses with different durations, ranging from milliseconds up to minutes. At least for these time scales, no effect of the pulse duration was observed. For much shorter (e.g.  $\mu$ s or ns) or longer (e.g. hours) stress durations, this might change and it therefore needs further investigation. However, to avoid unnecessary heating, it can be advantageous to apply relatively short pulses.

These findings and the discrete drops in the nanowire resistance, which do only depend on the current pulse height and on the history of previous drops, support the proposed model of merging grains. Another indication that it is a critical local electric field across the weakest oxide barrier(s) that causes, when exceeded, the resistance drop, lies in the distribution of the resistance steps  $R_n$  and the initial resistance value of a virgin sample. We note that both, the magnitude of the  $R_n$  changes and the adjusting accuracy, are dependent on the wire length. The wire resistance tends to increase with length, but does not strictly scale with it. For example, the initial resistance of the 1  $\mu$ m long wire in Fig. 5.4, is  $\sim 75$  times larger than that of the 250 nm long wire. The reason for this lies in the disordered character of the internal structure of the wire. A qualitative explanation for this

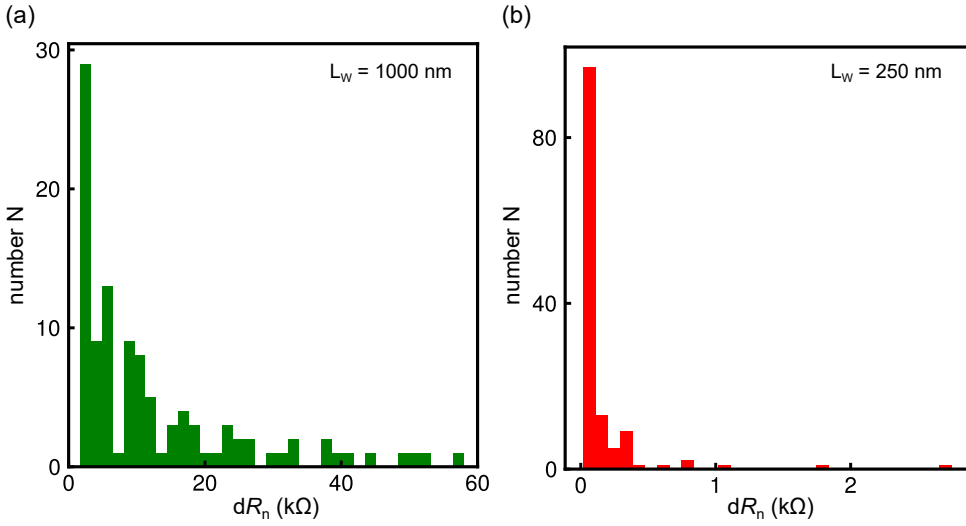


**Figure 5.5:** (a) Distribution of resistance steps  $R_n$  for a 1000 nm long nanowire. Adopted from Ref. [Vos+21]. (b) Distribution of resistance steps  $R_n$  for a 250 nm long nanowire. The related change in resistance for both wires is presented in Fig. 5.4. For the 1000 nm wire, the larger steps of  $dR_n > 20$   $k\Omega$  occur only at very small  $I_p$  values. For the 250 nm wire most resistance steps  $dR_n$  are below 1  $k\Omega$ .

behavior may lie in the random distribution of barrier thicknesses. To first order, the number of junctions in the network scales linearly with the length of the nanowire. The probability of having a few very weak internal junctions dominating  $R_n$  therefore also increases quickly with the length. As a consequence, the first changes in resistance are very steep (Fig. 5.4). With a further reduction of resistance, however, we observe smaller steps. Figure 5.5 displays the distributions of resistance steps  $dR_n$  for both wires from Fig. 5.4. The 250 nm wire revealed mainly small jumps ( $< 1$   $k\Omega/\mu A$ ) of similar height, while for the longer wire, at the beginning of the tuning process, also larger steps were observed ( $> 30$   $k\Omega/\mu A$ ). This is in good agreement with a random distribution of barrier thicknesses and fits to the expectations from the theoretical model, discussed in Sec. 5.1. Of course, there is a limit for the tuneability of a wire. At some point, for too high currents/powers, the stress can lead to structural damage, which in turn can lead to an increase in resistance or even to open circuits. But this limit seems to be rather high (for the wires studied here this limit was measured to be of the order of mA).

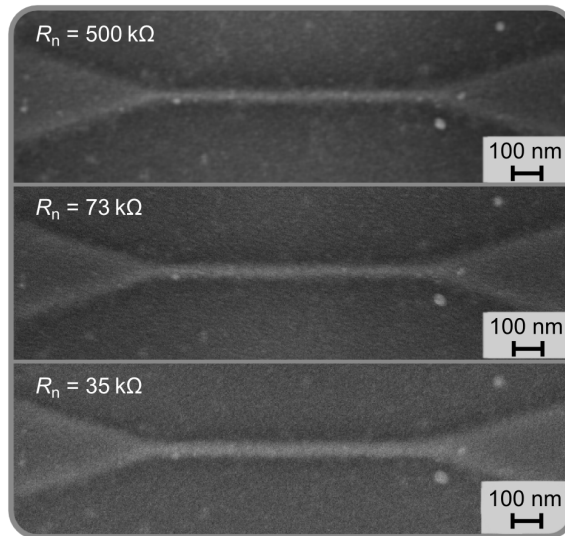


**Figure 5.6:** SEM pictures of the same 1000 nm long nanowire, taken before and after the treatment with current pulses. The resistance was reduced from  $R_n \approx 500 \text{ k}\Omega$  to  $R_n \approx 35 \text{ k}\Omega$ , at room temperature and with pulse amplitudes up to  $I_p \approx 180 \mu\text{A}$ .

## Impact of IEM on the geometric shape of the wire

To look for any changes in the geometry caused by the IEM treatment, we took scanning electron microscope (SEM) pictures of a virgin sample and of the same sample after it was altered by IEM. Fig. 5.6 displays three micrographs of the same micrometer long wire (initial resistance  $R_n = 500 \text{ k}\Omega$ ) before and after the treatment with pulses up to  $I_p \approx 180 \mu\text{A}$  leading to  $R_n = 35 \text{ k}\Omega$ . At least at this resolution, no changes in the geometric shape can be observed.

This is an important result for the further experiments, as it allows us to assume a constant wire geometry and, therefore, to study gradual resistance effects such as the relation between the phase slip energy  $E_s$  and  $R_n$ .

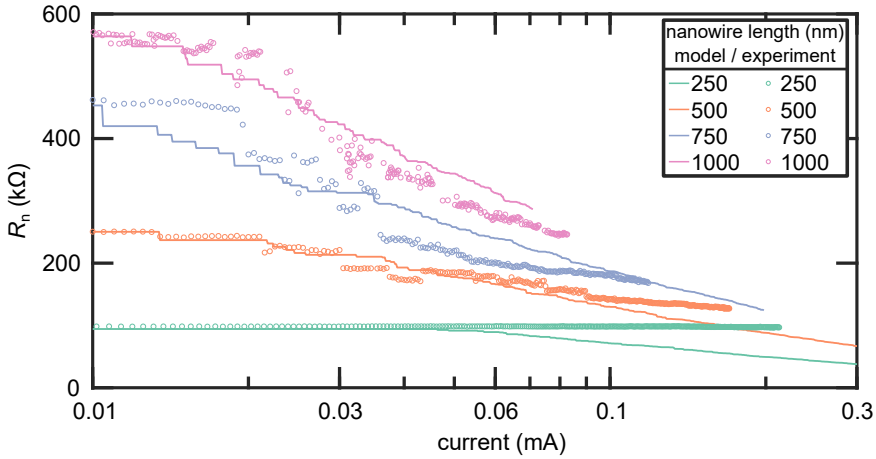


**Figure 5.7:** Normal state resistance vs. current pulse amplitude for wires of different length. The dots correspond to experimental data (measured at 4 K), and the solid lines correspond to simulations (fit parameter  $A = 0.2$  nm). Adapted from [Bar+22].

## Comparison between measurements and QPC model

Fig. 5.7 shows the change in resistance as a function of the applied current pulse for four wires of different lengths (250 nm, 500 nm, 750 nm, 1000 nm), measured and tuned at  $T = 4$  K [Bar+22]. The samples stem from a different fabrication run than the ones discussed before. The solid lines are fits to the QPC model. As fit parameter,  $A = Bta$  with dimension of length was used. For all curves,  $A$  was found to be 2 nm. Before the application of current pulses was simulated, several runs of wire construction were computed (assuming a mean separation distance and standard deviation of 0.35 nA) for the same geometry as in the experimental data in order to achieve a good agreement in initial resistances between experiment and simulation (for more details see Refs. [Bar+22; BAR21]).

In both, experiment and simulation, the resistance change rate ( $dR_n/dI$ ) is larger at the beginning of the tuning and decreases with further reduction of  $R_n$ . For longer wires, this behavior is pronounced. These findings fit well to the observed distributions of resistance steps, discussed in the previous part of this section. Interestingly, the model expects a linear dependence between the number of QPCs and the pulse duration (see Eq. 5.4). As stressed before, this is something we have not observed in the experiments. However, with tested pulse lengths between milliseconds and minutes, this might change for different time scales. Overall, taking into consideration the simplicity of the model, the comparison with our ex-

periments is surprisingly good, and the formation of point contacts in the junctions could be a possible explanation for IEM in granular aluminum nanowires.



# 6 Quantum phase slip experiments with nanowires

In this chapter, the main results of low-temperature measurements on nanowires made from granular aluminum are presented. The chapter is divided into two parts. In the first section, measurements on single wires are presented and the relationship between the transport behavior and quantum phase slips is discussed. In particular, the effects of gradual resistance changes are investigated for wires with pronounced phase slip behavior. The results are compared with the microscopic theory for quantum phase slip rates, developed by Zaikin and Goulubev [Zai+97; GZ01]. We then follow the approach introduced by Mooij and co-workers in Ref. [Moo+15] to derive a phase diagram for the phase slip driven superconductor to insulator transition and compare the result with previous works. In the last part of this section, the temperature dependence of the wire resistance below 3 K is investigated.

In the second section, measurements on realizations of the double wire circuit introduced in Sec. 2.12 are presented. We investigate the gate dependent transport behavior of circuits with different design parameters and the impact of IEM treatment. For certain configurations, we observe a gate induced transition between insulating and metallic resp. superconducting behavior. The results are compared with the QPS model and the phase transition, found for single wires.

## 6.1 Single wire experiments

To investigate the relationship between the normal state resistance of a granular aluminum nanowire and its transport behavior at milli-Kelvin temperatures, we use the intrinsic electromigration (IEM) method [Vos+21]. This approach significantly differs from the commonly used methods, such as ion beam milling or classical electromigration, since the structural shape of the nanowire remains unchanged while the intrinsic structure gets modified (see Sec. 5.2). Until now, it was not possible to access the regimes of high and low phase slip rates at low magnetic fields

with the same single wire [Kim+18; Bau+16; Kov+10], since the intrinsic properties, like coherence length or nanowire resistance, were fixed by the preparation of the wire. Apart from this new possibility, the approach we follow is very simple. In essence, we apply current pulses and measure the changes in the normal-state resistance of a wire together with the  $I - V$  characteristics in the superconducting state.

The dual to the Josephson energy  $E_j$  is the phase slip energy  $E_s$ , and instead of a charging energy  $E_c$ , one has an inductive energy  $E_L$  [MN06]. Consequently, the behavior of the phase slip junction should be defined by the ratio of these characteristic energies. To find a reasonable expression for the phase slip energy, Mooji and co-workers followed the Zaikin and Golubev model for zero current and temperatures close to  $T = 0$  (see Eq. 2.76). For the inductive energy  $E_L = \Phi_0^2/2L_k$ , it can be assumed that the kinetic inductance of the wire is fully dominating. The ratio between phase slip energy and inductive energy therefore can be expressed by Eq. 2.77. When altering  $R_n$ ,  $E_s$  changes exponentially and  $E_L$  linearly. Here, the general problem for the investigation and utilization of wires made from highly disordered superconductors where the resistance can strongly scatter, even under the assumption of a constant geometry, becomes evident (see also Sec. 3.1). Already small changes in  $R_n$  have a high impact on the ratio between  $E_s$  and  $E_L$  and thus on the transport properties of the wire. For the chosen approach, this strong dependency is actually beneficial since it allows to cover a large range of  $E_s/E_L$  ratios for a single wire.

Following Mooij *et al.* [Moo+15], we expect the following behavior for the wires: If  $E_L$  is much larger than  $E_s$ , the superconducting phase difference along the wire is well defined, and the wire reveals a superconducting behavior. In this regime, the coherent transport of Cooper pairs leads to a vanishing voltage drop up to a critical current  $I_c$ . The opposite energetic regime is reached when  $E_s$  is much larger than  $E_L$ . Here, the phase coherence across the wire is destroyed by phase slips, and no conductance is observed up to an applied critical voltage of  $V_c = 2\pi/2e E_s$ . In this insulating regime, the critical voltage provides a measure for the phase slip energy.

In the following, we report on the characterization of three nanowires with different lengths (1000 nm (A), 750 nm (B), 250 nm (C)). For all samples,  $L_w$  is much larger than the coherence length ( $\xi_0 \approx 8$  nm) determined in Sec. 3.1, which is an important requirement for high phase slip rates. The three nanowires are fabricated with the three-layer stack approach (first process), described in Sec. 3.3. All samples are placed on the same chip and made from a 20 nm thick  $\text{AlO}_x$  film with a sheet resistance of 2.7 k $\Omega$ . A detailed description of the sample layout, the surrounding impedances, and the measurement schemes used is provided in chapter 3. Fig. 6.1

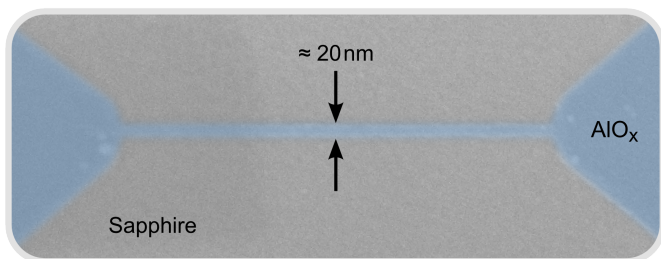


**Figure 6.1:** Scanning electron micrograph of a lithographically fabricated granular aluminum nanowire (colored in blue) on a sapphire substrate. The wire has a width and thickness of about 20 nm and is 750 nm long.

shows a scanning electron microscope picture of a 750 nm long and about 20 nm wide wire. The characterization of the transport behavior, as well as the application of the IEM method, were carried out in a dilution refrigerator at a temperature of 25 mK.

### 6.1.1 Reducing the normal state wire resistance with current pulses

For the transport characterization and the gradual resistance changes, we used a computer-controlled measurement protocol which includes the following steps: First, the  $I - V$  characteristics were measured in either a voltage biased scheme (insulating regime) or a current biased scheme (metallic regime and superconducting regime). Then, a current pulse with amplitude  $I_p$  is applied for about 20 ms to reduce the normal state resistance  $R_n$  of the wire. This step is followed by a waiting time of at least a few seconds (for larger currents several minutes), to allow the samples to recover into thermal equilibrium. The new resistance value is then determined with an excitation significantly below  $I_p$ . The measurement cycle then is completed by the next  $I - V$  characterization [Vos19].

Fig. 6.2 shows the change in wire resistance as a function of the amplitude of the applied IEM pulse for samples A and C. For sample A, the resistance is reduced from 900 k $\Omega$  to 2.5 k $\Omega$ , for sample C from 12.4 k $\Omega$  to 1.5 k $\Omega$ . The colored areas in Fig. 6.2, labeled as insulating, metallic and superconducting, reflect the observed transport behavior for small bias values. The individual regimes will be examined in more detail in the course of the following discussion.

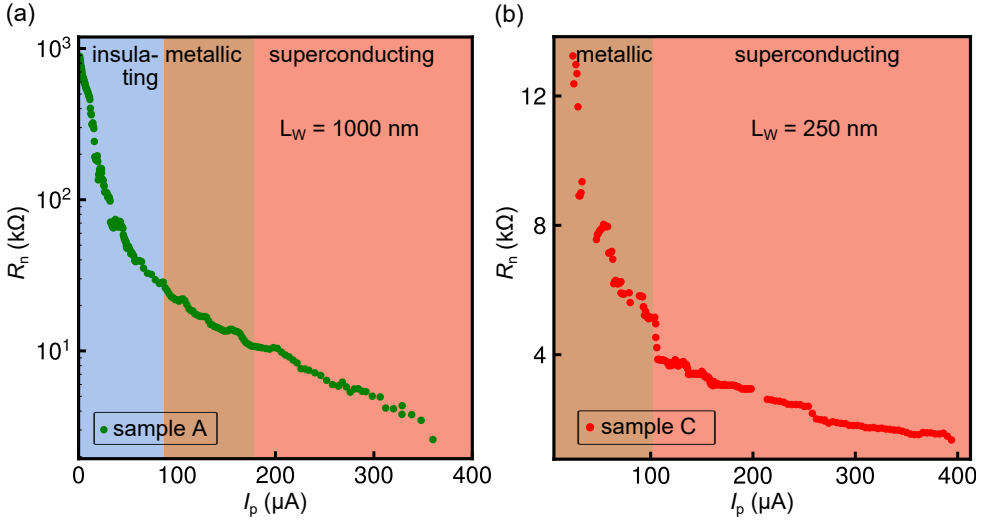


**Figure 6.2:** Normal state resistance  $R_n$  as a function of the applied pulse current  $I_p$  for sample A (a) and sample C (b). The measurements are performed at 25 mK. For sample A,  $R_n$  is lowered from 900  $k\Omega$  to 2.5  $k\Omega$ , for sample C from 12.4  $k\Omega$  to 1.5  $k\Omega$ . At low bias values, the  $I - V$  characteristics reveal an insulating, metallic and superconducting behavior, depending on the respective resistance (see coloring). From Ref. [Vos+21].

The wire resistances shown in Fig. 6.2 as well as those used in the further discussion are determined by  $R_n = R_{\text{tot}} - R_L - R_{\text{th}}$ , where  $R_{\text{tot}}$  is the respective total value of the resistance measured.  $R_L = 26.5$   $k\Omega$  (samples A and C),  $R_L = 39$   $k\Omega$  (sample B) are the resistances of the on-chip leads connecting the nanowires. At larger current bias values, we also recognized a ‘thermal’ resistance offset  $R_{\text{th}}$ , which is of the order of 15  $k\Omega$  and can be explained by considering Joule heating [Bau+16]. Experimentally, the lead resistances and the thermal offset can be precisely determined from the resistive slopes of the  $I - V$  characteristics above  $I_c$  (when the wire is in the superconducting regime). The lead resistances found are in very good agreement with values calculated from the geometry and the sheet resistance. For the present samples, we determined the resistances  $R_{\text{tot}}$  in the insulating and metallic regime from  $I_p$ . In the superconducting regime, we extracted the  $R_n$  values directly from the resistive slopes.

**Table 6.1: Parameters of the samples measured at mK temperatures.** All  $\text{AlO}_x$  nanowires have a width and a thickness of 20 nm.  $R_n^0, R_n^E$  denote the initial and final normal-state resistance (before and after altering the nanowire),  $E_s^0$  and  $E_s^E$  are the corresponding phase slip energies.  $R_n^m, E_s^m$  and  $R_n^s, E_s^s$  are the largest metallic and superconducting normal-state resistances / phase slip energies.

#	$L_w$ nm	$R_n^0$ k $\Omega$	$R_n^E$ k $\Omega$	$R_n^m$ k $\Omega$	$R_n^s$ k $\Omega$	$\frac{R_n^0}{R_n^E}$	$\frac{E_s^0}{h}$ GHz	$\frac{E_s^m}{h}$ GHz	$\frac{E_s^s}{h}$ MHz	$\frac{E_s^E}{h}$ Hz
A	1000	900	2.5	37	16	360	200	2.5	1	10e-21
B	750	500	3.7	28	17	135	164	3.0	34	10e-7
C	250	12.4	1.5	12.4	4.7	8.3	0.5	0.5	2.5e-3	10e-16

## 6.1.2 Insulating regime

In the insulating regime, by definition, no charge transport is possible below a certain threshold voltage. From the discussion above we expect such a behavior for  $E_s \gg E_L$  and therefore for rather large resistance values and / or long wires (see Eq. 2.76).

In Fig. 6.2 (a), it was already indicated that sample A initially showed an insulating behavior. The  $I - V$  curves associated with the resistance values shown there are presented in Fig. 6.3. For wire resistances between 900 k $\Omega$  and 37 k $\Omega$ , the measured curves show a clear Coulomb blockade with a critical voltage that strongly depends on the normal state resistance of the wire. For this sample, the blockade range is from 3.6 mV to about 0.1 mV, which corresponds to a QPS rate span of  $\approx 200$  GHz.

Sample B also showed, prior to applying any current pulses to lower  $R_n$  and for  $R_n$  values down to  $\approx 28$  k $\Omega$ , a pronounced Coulomb blockade. Sample C had an initial  $R_n = 12.4$  k $\Omega$  and did not show an insulating behavior. An overview of the resistance values and associated phase slip rates for all three samples is given in Tab. 6.1.

## 6.1.3 Dependence of the Coulomb blockade on the normal state resistance

In the blockade, the measured current is below  $\sim 400$  fA (for samples A and B), and the transition to the conductive state is, in general, rather sharp. Also, the  $I - V$  characteristics are not hysteretic in the current values. Therefore, the critical voltage can be precisely determined from a threshold current, defining the conductive state. Only for high blockades with critical voltages  $V_c > 2$  mV (corresponding to

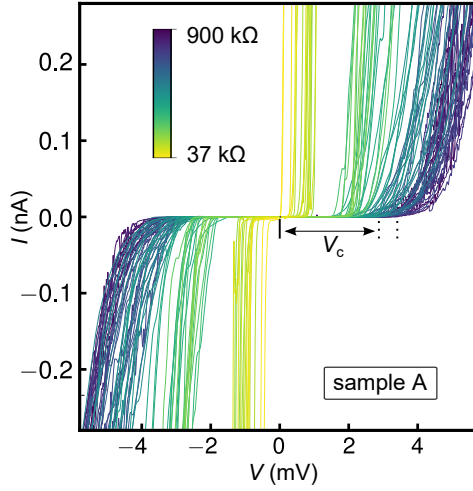


**Figure 6.3:** (a)  $I - V$  characteristics for a 1000 nm long nanowire. The sample starts with a high  $R_n$  value (dark) and is tuned to lower  $R_n$  (bright). The Coulomb blockade range is from 3.6 mV for a normal-state resistance of  $\approx 800 \text{ k}\Omega$  down to about 0.1 mV for the lowest resistance value ( $\approx 40 \text{ k}\Omega$ ).

$E_s/h \approx 150 \text{ GHz}$ ), we observed a continuous rounding of the  $I - V$  characteristics close to  $V_c$ . This rounding leads to a significant error in the determination of  $V_c$ . A possible explanation comes from the relatively low environment impedance of  $0.6 \text{ k}\Omega$  (for more details about the sample design, see Sec. 4.2.1). Dissipation in the nanowire can lead to an elevated temperature and therefore a smoothing at the transition from blockade to conductive state [HZ12].

The extracted critical voltages for samples A and B are shown in Fig. 6.4 (a). Larger gaps in  $V_c(R_n)$  can be explained by the initially rapid change in  $R_n$ , when using the IEM method. In this region (see also Fig. 6.2 (a)) the resistance steps can be of the order of  $\sim 10 \text{ k}\Omega$ .

With the successive reduction of the wire resistance, we also expect the coherence length to slightly increase, since the IEM treatment leads to more and more galvanically connected grains inside the wire. Thus, the grain boundary scattering gets reduced [SA92], which leads to a longer mean free path  $l_0$  and therefore to an increased coherence length  $\xi_{\text{eff}} = \sqrt{l_0} \xi_0$ . This effect has also been observed in previous experiments, where granular and amorphous systems were grown under different conditions [Bos+06] or treated by classical electromigration [AB11].

The data presented in Fig. 6.4 (a,b) are best fitted assuming a linear  $\xi$  span from  $\xi = 8 \text{ nm}$  ( $R_n = 900 \text{ k}\Omega$ ) to  $\xi = 12 \text{ nm}$  ( $R_n = 37 \text{ k}\Omega$ ). The overlaid curves in Fig. 6.4 (a) are fits of the Zaikin, Golubev and Mooji model to the measured values, using

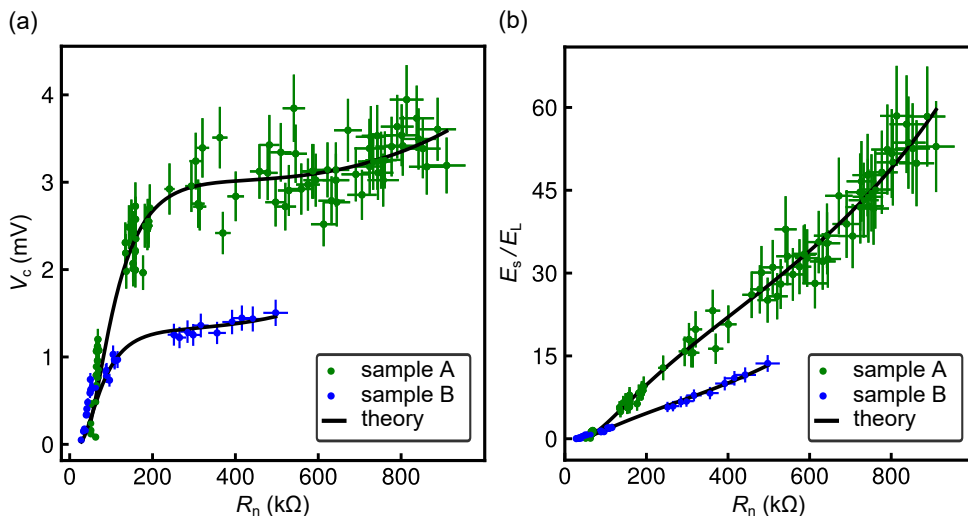


**Figure 6.4:** (a) Critical voltages  $V_c$  as a function of the normal-state resistance  $R_n$ . The comparison of measured values and the predictions from Eq. 2.76 (a) and Eq. 2.77 (b) with the fitting parameters  $\alpha = 0.07 \pm 0.01$  and  $\beta = 0.49 \pm 0.03$  shows a good agreement for both wires (see black solid lines in (a) and (b)). (b) Ratio between phase slip energy  $E_s$  and inductive energy  $E_L$  as a function of the normal-state resistance of wires A and B. For both wires, the ratio converges for smaller resistances towards the same value of  $E_s/E_L \approx 0.02$ , where the metallic regime begins. From Ref. [Vos+21]

Eq. 2.76. From these fits, we find values for the empirical parameters  $\alpha = 0.07 \pm 0.01$  and  $\beta = 0.49 \pm 0.03$  that are common to the data of samples A and B. The extracted parameters are in good agreement with the values given in Ref. [Moo+15].

Interestingly, it seems that for very high  $R_n$  values ( $> 200$  k $\Omega$ ),  $V_c(R_n)$  only grows slowly. The reason for this behavior is not yet clear. In general an upper limit for the critical voltage is roughly given by  $V_{c,\max} \sim (L_w/\xi)(\Delta/e)$  [AL22]. This upper threshold is one order of magnitude higher than the values measured for the present wires and therefore seems not to be the limiting factor. A possible explanation is that this limit is reached for some sections of the wire and not for others.

Fig. 6.4 (b) shows how the ratio between the phase slip energy and the inductive energy develops for samples A and B. For the highest resistance values, the ratio is  $\sim 60$ , while for the smallest  $R_n$  values it only is  $\approx 0.02$ . The solid black curves show the expectations from the phase slip model, using Eq. 2.77 together with the previously determined values for  $\alpha$  and  $\beta$ . The agreement between the measurements and the QPS theory is excellent, especially when considering that also the change in inductive energy is taken into account. Below a ratio of  $E_s/E_L \approx 0.02$ , both wires

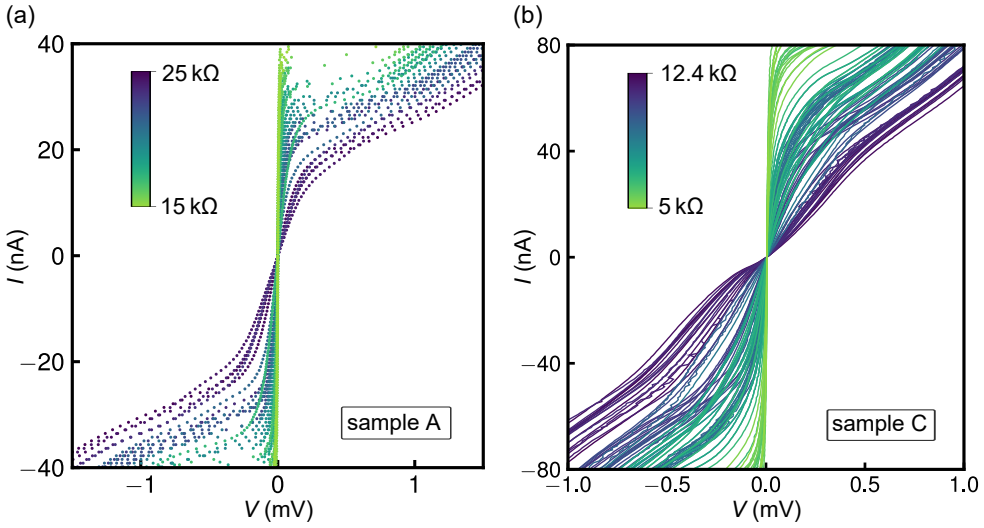


**Figure 6.5:**  $I - V$  characteristics of samples A (a) and C (b) in the metallic regime: For sample A the resistance span is from  $\approx 25 \text{ k}\Omega$  to  $15 \text{ k}\Omega$ , for sample C from  $\approx 12.4 \text{ k}\Omega$  to  $4.7 \text{ k}\Omega$ . In the vicinity of zero bias current, the slope increases when the wire resistance is reduced. For all  $I - V$  curves in the metallic regime, the differential resistance around zero bias is  $dV/dI > 0$ . Sample C, in distinction from samples A and B, initially showed a metallic behavior. From Ref. [Vos+21]

revealed no Coulomb blockade anymore. Instead, a metallic-like behavior is then observed.

### 6.1.4 Metallic regime

For all samples with  $R_n$  values between  $40 \text{ k}\Omega$  and  $16 \text{ k}\Omega$ , a metallic-like behavior is observed. Here, the  $I - V$  characteristics show a linear response for small bias values and a non-linear response at larger bias values. The  $I - V$  curves, taken from samples A and C in this regime, are presented in Fig. 6.5.

Following Ref. [MN06], the expectations for the transport behavior for the two extreme regimes  $E_s \gg E_L$  and  $E_s \ll E_L$  are an insulating and a superconducting behavior. There is no statement about a possible intermediate regime. Naturally, one could expect a similar transition as it is observed for Josephson junctions with the phase diffusion regime at  $E_j \sim E_C$ , in particular at finite temperatures [Ian+89; Fis14]. Consequently, such a regime would be something like a charge diffusion regime, where on average neither the localization of charges in the wire nor the

phase coherence across the wire is dominating. However, the origin of this metallic regime is currently not clear and we can only speculate:

If we assume that the QPS model is still valid, we can estimate values for the characteristic energies, using the previously determined parameters  $\alpha$  and  $\beta$ . From Eq. 2.76 we get a frequency span for the QPS rate, ranging from  $E_s/h \approx 3$  GHz down to  $E_s/h \approx 30$  MHz. The inductive energies range from  $E_L/h \approx 150$  GHz to  $E_L/h \approx 250$  GHz. To calculate these values, we used the largest and smallest resistance values in the metallic regime (see Tab. 6.1). For the phase slip energy, the smallest values are already of the same order as the thermal energy corresponding to a temperature of  $\approx 25$  mK.

Although the exact origin of the insulating to metallic and metallic to superconducting (I-M-S) transition is not clear for the wires at hand, there are similar systems where such a transition has also been observed. For example in 2D granular films [KKS19; Kat95; GD10; Bel+07], metal hybrids, [AHB12] or 1D/2D arrays of Josephson junctions [FZ01; Vog+15; VCS16; Ced+15; Ced+17]. Since the internal structure of the wires can be described by a random network of Josephson junctions, it can be expected that for the systems mentioned and for the wires similar energy scales are relevant. In the junction model, the two characteristic energies are the finite charging energy of the grains and the Josephson energy. The former leads to a localization of charges, while the latter defines the energy scale for the delocalization. Depending on which energy is dominating, a network of junctions should reveal an insulating or superconducting behavior but also an intermediate regime for the cross over, where some few conductance channels exist.

From the measurements on double wire systems, presented in Sec. 6.2, we see that the phase slip energy plays a crucial role in the I-M-S transition. However, further investigation of the dependencies on magnetic fields and on temperature are needed to get a clearer understanding of the underlying physical processes.

### 6.1.5 Superconducting regime

For all samples, the metallic regime is followed by a superconducting regime, when  $R_n$  is further reduced. Here, current transport without dissipation is observed up to a critical value  $I_c$ . Just as for the transition from insulating to metallic behavior, this transition is sharp.

Fig. 6.6 displays the  $I - V$  characteristics for samples A and C in this regime. The inset in Fig. 6.6 (a) reveals an interesting detail. For relatively small critical currents, and therefore large  $R_n$  values, the voltage develops rather smoothly around  $I_c$ . This

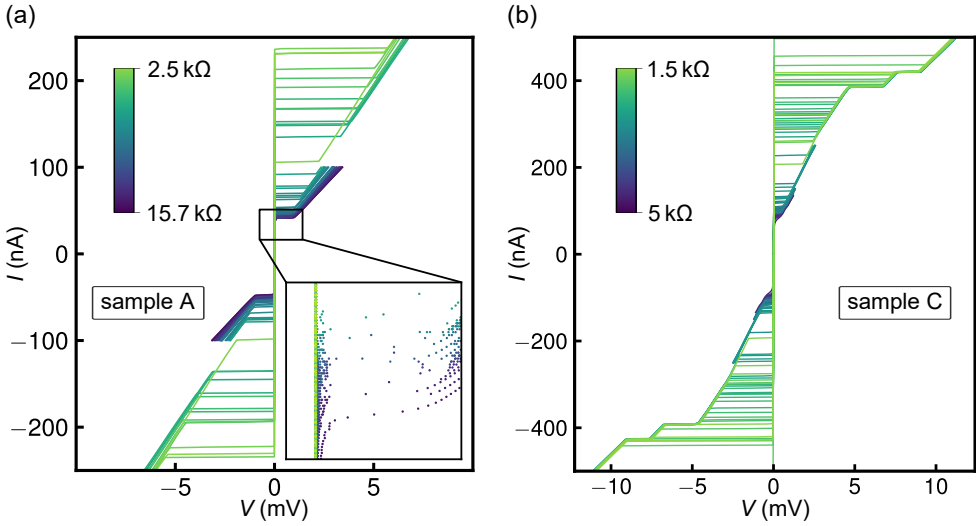


**Figure 6.6: Superconducting regime:**  $I - V$  characteristics of sample A (a) and C (b) as a function of normal-state resistance. Here  $R_n$  is extracted from the resistive slope above  $I_c$  at finite voltages. For sample C, the linear subbranches above  $I_c$  are caused by the on-chip leads, where the superconductivity breaks down sequentially in distinct steps (for sample A only visible at larger currents, outside of the shown current range). From Ref. [Vos+21]

transition to the resistive branch looks very similar to the phase diffusion behavior, observed for small capacitance Josephson junctions. With further reduction of  $R_n$ , the critical current increases and the switching becomes more sharp, until a clear voltage jump can be found. The magnitude of this voltage discontinuity then further increases with the decrease in wire resistance, as it is typical for superconducting nanowires.

The wire resistance per nanometer for all wires in this regime is below  $R_n/L_w \approx 20 \Omega/\text{nm}$ . For the two longer wires, the total normal state resistance  $R_n$  can be far above the resistance quantum  $R_q = 6.45 \text{ k}\Omega$ . Thus, these observations do not fit to the expectations from Chakravarty–Schmid–Bulgadaev theory, which predicts a transition at  $R_n = R_q$ , driven by dissipation and the interaction of QPS with the environment [Cha82; Bul84; Sch83; Kat+06]. Similar observations were made for MoGe nanowires in Ref. [Bol+08] and for NbTiN wires in Ref. [Kat+06]. These measurements, however, are in accordance with a phase transition driven by the  $E_s/E_L$  ratio, which will be discussed in Sec. 6.1.7.

## 6.1.6 Dependence of the critical current on the normal state resistance

Just as we did for the metallic regime, we can use the previously determined values for  $\alpha$  and  $\beta$  and make some estimates for the energies from the perspective of the QPS model. While  $E_s$  is of the order of a few MHz for the largest resistance values and decreases to almost zero for the smallest  $R_n$  values,  $E_L$  is of the order of a few hundred GHz. Consequently, the inductive energy is fully dominating in this regime, and phase coherence across the wire occurs. Therefore it might be justified to describe the wire as a superconducting weak link, and compare some commonly used models with the observed  $I_c(R_n)$  dependency.

In Sec. 2.6, the Ambeogaokar-Baratoff (AB) relation for S-I-S Josephson junctions and the Kulik-Omel'yanchuk (KO1) relation for short weak links in the dirty limit were introduced. At first glance, both systems are rather different compared to the nanowires presented here. However, some arguments can be found which may justify a comparison: For the AB relation, a simple S-I-S junction with the same energy gap at both electrodes is assumed. For the nanowire, the intrinsic structure is a random network of S-I-S Josephson junctions. Due to the relatively small wire diameters ( $\sim 20$  nm), compared to the aluminum grain size ( $\sim 4$  nm), there are only a very few parallel conductance channels. Thus, the wire could behave similarly to a one-dimensional chain of Josephson junctions. Therefore, the critical current of the wire would be defined by the weakest junctions in the network. Following this idea, it is possible that the same dominating junction gets modified multiple times by the application of IEM pulses, e.g. by a reshaping of the junction or by the formation of nanoshorts in the barrier.

The KO1 model is valid for a short weak link in the dirty limit ( $L_{\text{link}} < \xi$  and mean free path  $l_0 \ll L_{\text{link}}$ ). Obviously, the wire lengths are much longer than the coherence length of  $\xi \sim 8$  nm. This is still true when taking into account the possible increase of  $\xi$  by a few nanometers through the IEM treatment. The upper limit of the applicability for the KO1 theory is given by  $L_{\text{link}}/\xi \sim 3.49$ . However, since the phase will mainly drop over the insulating barriers between the aluminum grains, the relevant length is highly reduced. If we assume a grain size of 4 nm and a barrier thickness of 1 nm, the effective wire length is  $L_{\text{eff}} \simeq L_w/5$ . This could even be smaller if a significant portion of the grains is galvanically shorted.

The extracted  $I_c(R_n)$  values for the three wires are presented in Fig. 6.7 together with a comparison to the AB and KO1 models ( $\langle I_c \rangle = g'(\pi\Delta_{\text{BCS}}/2e)\langle R_n \rangle^{-1}$  with  $g' = 1.32$  (KO1, Eq. 2.27) or  $g' = 1$  (AB, Eq. 2.26)). Here, no fitting parameters were introduced.

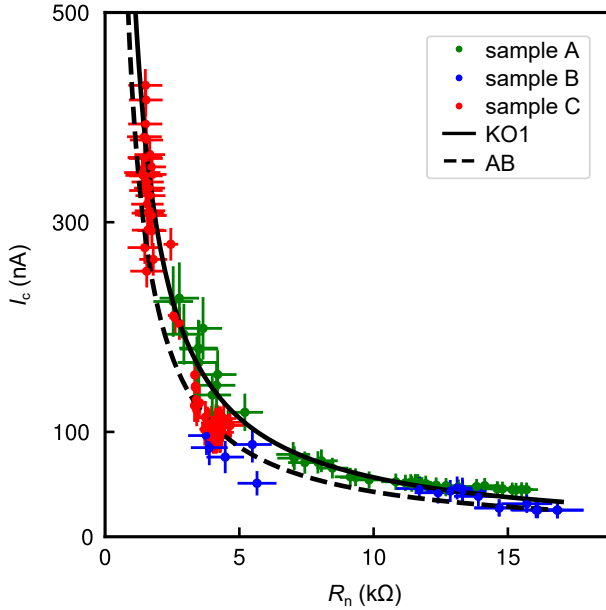


**Figure 6.7:** Critical currents, when the wires are in the superconducting regime, compared with the predicted values from the KO1 theory (black solid line) and AB theory (black dashed line). From Ref. [Vos+21]

Considering how different the compared systems are, the agreement is surprisingly good. The observed critical currents are ranging from  $I_c \sim 25$  nA up to  $I_c \sim 500$  nA. This large span, combined with the good adjustability of  $I_c$ , using the IEM method, makes these nanowires an interesting candidate to be used as key elements in quantum circuits, operating not only in the QPS regime [Sch21; Sch+20].

### 6.1.7 Phase diagram

Now that the different regimes, insulating, metallic and superconducting have been discussed, the transition and the dependencies on the wire parameters will be examined in more detail. We use the results to construct a tentative phase diagram. Even though one can smoothly tune through the different regimes, using the IEM method, at the border between two neighboring regimes a sudden and drastic change in the  $I - V$  characteristics between two  $R_n$  values is observed.

Fig. 6.8 shows the extreme change in the transport behavior for the insulating to metallic (a) and for the metallic to superconducting (b) transition. Of course, one

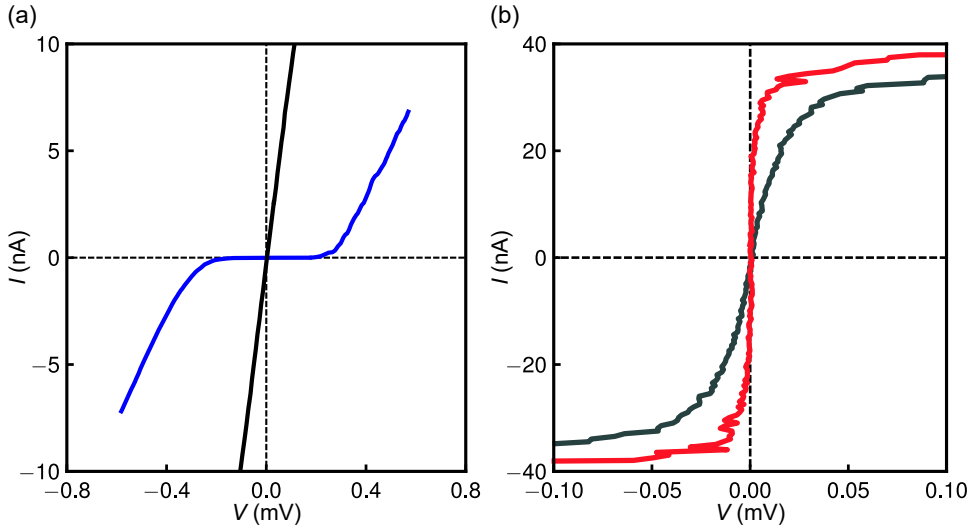


**Figure 6.8:**  $I - V$  characteristics of sample A at the phase transitions (between two IEM pulses). **(a)** For  $R_n > 37 \text{ k}\Omega$ , the response is insulating (blue line), below it is metallic (black line). **(b)** The second transition appears at  $R_n \approx 18 \text{ k}\Omega$ . Here the behavior again changes abruptly, but now from metallic (black line) to a superconducting behavior (red line). From Ref. [Vos+21]

can argue that there is a resistance gap between the tuning steps, and that therefore the smoothness of the transition might only be a matter of resolution. However, in the course of this work, over fifty wires have been examined and for all samples the boundary was sharp enough to make a clear distinction.

To construct the phase diagram, we follow the approach from Mooji *et al.* and determine the ratios  $E_s/E_L$  at which the insulating to metallic and the metallic to superconducting transitions occur [Moo+15].

For the transition from insulating to metallic behavior, the ratio can be determined from the smallest critical voltage in the insulating regime and the corresponding resistance value. The resulting ratio is  $E_s/E_L \approx 0.02$ . The transition ratio for the metallic to superconducting transition is determined from the largest  $R_n$  value in the superconducting regime. At this transition, in the QPS model, the ratio  $E_s/E_L \approx 10^{-4}$ .

With these values and assuming that they are common for all wires, we can use Eq. 2.77 to define the borders between the different regimes (see Sec. 2.10). The resulting diagram for our nanowires is presented in Fig. 6.9. Here, the resistance per coherence length ( $R_\xi = R_n \xi / L_w$ ) divided by the quantum resistance is plotted over the wire length in units of  $\xi$ . The black solid lines mark the constant  $E_s/E_L$

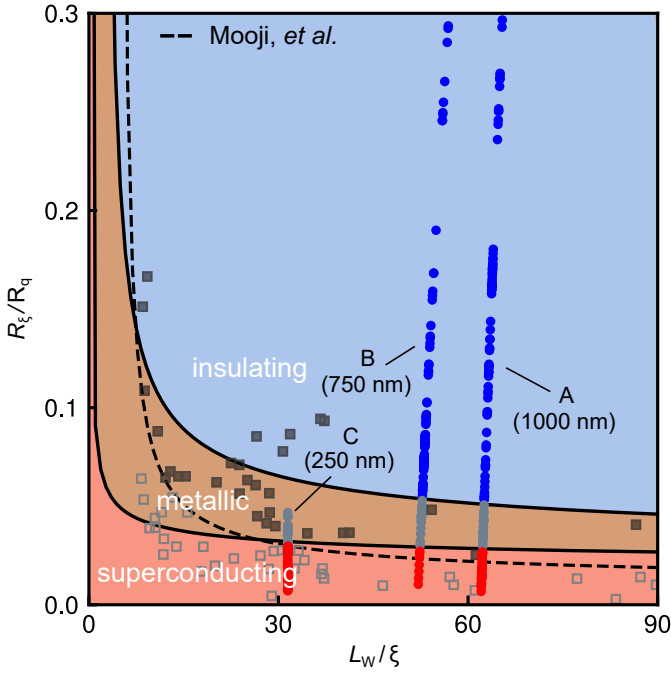


**Figure 6.9:** Tentative phase diagram for nanowires made from oxidized (granular) aluminum. For the black lines, the ratio between the phase slip energy and the inductive energy of the wires is constant for different geometries and specific resistances. The dots represent the altered normal-state resistances and the colour represents the low temperature state (blue = insulating, gray = metallic, red = superconducting). Assuming a constant wire geometry and only small changes in the coherence length, the ratio between  $E_s$  and  $E_L$  decreases together with  $R_n$ . From the smallest measurable critical voltages, we find a constant ratio of  $E_s/E_L \approx 0.02$  (see Fig. 6.4) for the insulating to metallic transition (upper black line). The ratio at which the transition, metallic to superconducting, occurs ( $E_s/E_L \approx 10^{-4}$ , lower black line), is determined from the smallest  $R_n$  values in the superconducting regime. For both transition lines, the previously determined values of  $\alpha = 0.07$  and  $\beta = 0.49$  have been used. The black and gray squares represent the data from Bollinger *et al.* [Bol+08] and the model is taken from [Moo+15]. From Ref. [Vos+21]

ratios for the crossovers. Samples A, B and C are represented by the dotted lines. Each point stands for a different resistance value. The small tilt is caused by the change in coherence length. Even though the wires have rather different lengths, the transitions are at approximately the same  $E_s/E_L$  ratios. For comparison, the data for MoGe wires from Bollinger, *et al.* [Bol+08] (squares) with the proposed phase separation from Mooji, *et al.* (dashed line) are added. For these data, it is not strictly distinguished between insulating and metallic behavior. This explains why the data for the insulating regime appear in both, the metallic, and the insulating regime in our diagram.

The parameters for the dashed line are  $\alpha \approx 0.2$ ,  $\beta \approx 0.11$  and  $E_s/E_L \approx 0.3$ , however, similar good results were achieved with different sets of parameters [Moo+15]. The reason is the indeterminacy of the empirical parameters  $\alpha$  and  $\beta$ . Here, a major difference to our approach becomes evident. Since we can determine  $\alpha$  and  $\beta$  from a single wire in the insulating regime, the only free parameter is the ratio  $E_s/E_L$  which can be determined as described above.

In Ref. [Mak+16], the authors were also following the approach from Mooji, *et al.* to derive a phase diagram for NbTiN nanowires (also not strictly discriminating between metallic and insulating behavior). Doing so, they faced the same problem with the uncertainty of  $\alpha$  and  $\beta$  and therefore presented several combinations of parameters. The parameter range is compatible with the values from Ref. [Moo+15] and therefore also with our results. This is an indication that the separation of phases we found for granular aluminum wires is of a more general character and valid also for wires made from other materials.

An interesting detail of the phase diagram is that it predicts a higher tolerance for phase slips in the metallic and superconducting state for shorter wires, which we will use in the double wire experiments.

### 6.1.8 Temperature dependence of the nanowire resistance below 3 K

For the discussion up to this point, only measurements at temperatures close to  $T = 0$  were considered. In the following, we will briefly discuss the temperature dependence of the transport behavior. For this purpose, we tuned individual wires through the phase diagram described above by using the IEM method. We recorded the I-V curves for the different resistances/regimes as a function of the temperature. The broad spectrum of bias excitations generated in this way also allows to investigate the bias current dependence of the differential resistance.

Fig. 6.10 shows the  $R(T)$  measurements for a 250 nm (a) and a 500 nm (b) long nanowire for different normal state resistances  $R_n$  and at small excitations ( $< 0.1$  nA). The resistance offsets, coming from the leads ( $\sim 20$  k $\Omega$ ), are not subtracted.

For both wires, we initially find (for large  $R_n$  values, dark lines) a strong increase of the resistance below  $T_c$ . At temperatures close to  $T = 0$ , we measure clear Coulomb blockades for these resistances. For the other extreme of rather low resistance values (bright lines), the samples reveal a superconducting behavior below  $T_c$ . At intermediate resistances,  $dV/dI$  approaches constant non zero values, or it can

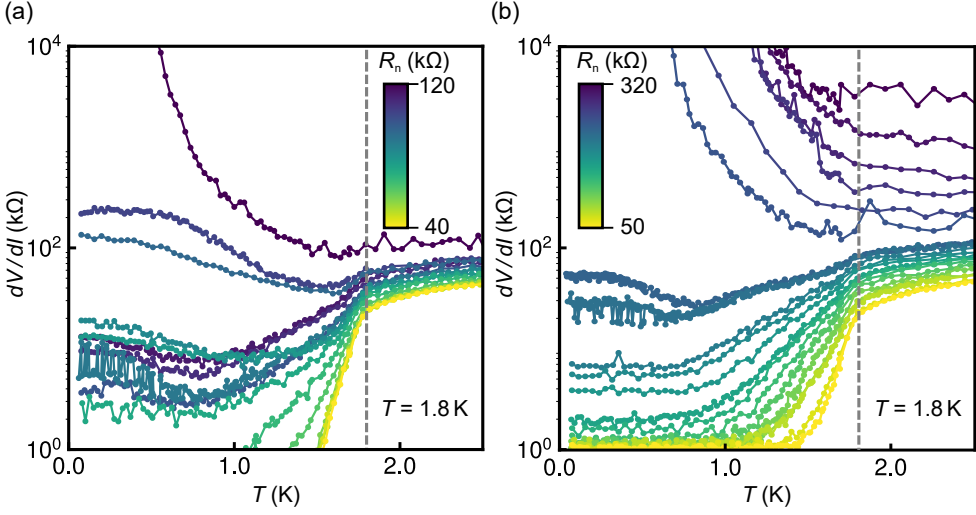


**Figure 6.10:**  $R(T)$  dependence for a 250 nm (a) and 500 nm (b) long nanowire for different normal state resistances  $R_n$ . The excitation used is below 0.1 nA. For large resistance values,  $R(T)$  increases below  $T_c$ , for small values it decreases. Even though the normal state resistance of the wires is highly reduced,  $T_c$  seems not to change significantly.

even increase again far below  $T_c$ . The former behavior is typical for nanowires with pronounced QPS rate (for an overview see e.g. Ref. [Bez12]). The latter is a signature of a zero bias anomaly (ZBA). Here,  $dV/dI$  also strongly depends on the bias current. Such ZBAs were frequently observed in nanowires of different materials and shapes, but the origin is rather unclear and still under debate. Possible explanations include electron heating, localization of quasi particles and interaction between QPS pairs [RS20; Mei+11; Zai+97].

For  $R_n$  values below pronounced ZBAs, we can compare the  $R(T)$  dependence below  $T_c$  with the QPS and TAPS (thermally activated phase slips) models, introduced in Sec. 2.9. Above  $T_c$  we follow Ref. [Del+12] and compare the resistance with the Aslamasov-Larkin (AL) model in the 1D limit, describing the additional contribution to the conductivity which comes from the condensate, that starts to form close to  $T_c$ :  $(R_{AL}^{-1}(T) - R_n^{-1})^{-1} = \frac{32L_w}{\pi^2} (\hbar/(4e^2\zeta_0)) (T/(T - T_c))^{-3/2}$ . Fig. 6.11 shows a selection of the  $R(T)$  curves from Fig. 6.10 (a), together with fits, using the AL model for temperatures above  $T_c$ , Littel's fit (Eq. 2.42 with Eq. 2.55) for temperatures slightly below  $T_c$  and the Golubev and Zaikin QPS model for lower temperatures (Eq. 2.61). For all fits it is assumed that  $\zeta_0 = 8$  nm and  $L_w = 250$  nm. The fitting parameters  $(\alpha, \beta, a)$  are of the order of one and were kept constant. The

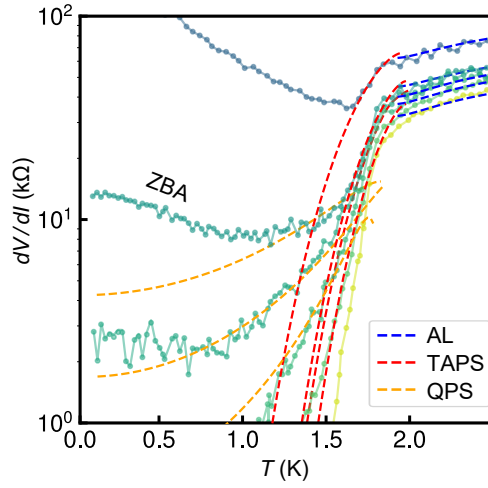


**Figure 6.11:**  $R(T)$  curves from Fig. 6.10 (a) together with a comparison to the expected temperature dependencies of Aslamasov-Larkin (AL), TAPS and QPS models. Above  $T_c \approx 1.8$  K, the decrease in  $dV/dI$  can be explained for all curves by the AL model. Slightly below  $T_c$ , the resistance follows the typical TAPS behavior. The QPS model fits only for traces with  $dV/dI \ll R_n$  at lowest temperatures.

best fits are obtained for  $T_c = 1.9$  K. In general,  $T_c$  seems not to be significantly affected by the reduction of the wire resistance.

For temperatures above  $T_c$ ,  $R(T)$  can be well explained by the AL model for all traces. Close below  $T_c$ , the curves follow the TAPS behavior, except for lowest resistances (bright curve). For lower temperatures, QPS start to dominate the resistance. Here, the QPS model fits best for  $R(T)$  behaviors which are flat at lowest temperatures (see also Fig. 6.10 (b)). For wire resistances, which are roughly above  $30 \text{ k}\Omega$  the increase in  $dV/dI$  (ZBA) is not governed by the model. This is not surprising since the QPS model used is only applicable when  $R_{\text{QPS}} \ll R_n$ . As stressed before, the nature of the ZBA is still under investigation. In the tentative phase diagram which was introduced earlier, these curves are associated with the metallic phase, where neither the phase slip energy nor the inductive energy is dominating. Interestingly, we observe a trend, that strongly pronounced ZBAs are more likely in shorter wires (also visible when comparing Fig. 6.10 (a) for the 250 nm wire with (b) for the 500 nm wire). This agrees with the phase diagram from Fig. 6.9 and is a hint, that the absolute value of  $dV/dI$  at temperatures close to  $T = 0$  and small bias values is related to  $E_s$ . Overall, the observed transition is very similar to the one found in Ref. [Mak+16] for NbTiN nanowires. Here, the SIT transition is also well explained by the change in  $E_s/E_L$  ratio.

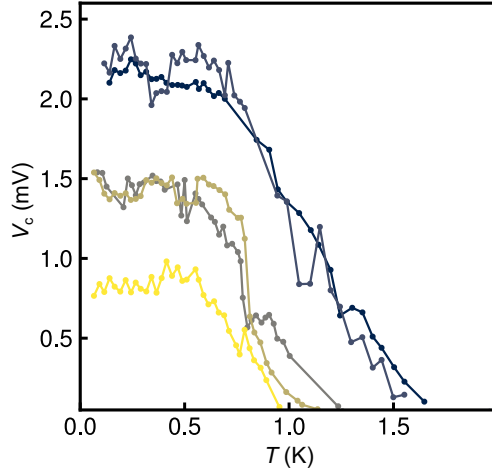


**Figure 6.12:** Temperature dependence of the critical voltages. The values are extracted from the  $I - V$  characteristics of the 500 nm long wire. The corresponding  $R(T)$  curves, which show rapid increase below  $T = T_c$ , are presented in Fig. 6.10 (b).

### 6.1.9 Temperature dependence of the critical voltage

To investigate the temperature dependence of the critical voltage, we have extracted  $V_c(T)$  from the temperature dependent  $I - V$  curves of the previously discussed 500 nm long wire at different  $R_n$  values. The corresponding  $R(T)$  curves show a strong increase below  $T_c$  (see Fig. 6.10 (b)).

Fig. 6.12 shows the extracted critical voltages as a function of the temperature. In the blockade, the measured current for this sample was below 500 fA. At temperatures close to  $T = 0$ , the critical voltage is not significantly affected by an increase in temperature and we find plateaus. The size of the plateau depends on the maximum value of  $V_c$ . The observed plateaus for lowest temperatures are consistent with the observations made for NbSi nanowires with pronounced QPS behavior [Web+13]. For the largest blockade of about 2.3 mV, the comparable thermal energy is  $eV_c/k_B \approx 27$  K, while for the smallest ( $\approx 0.8$  mV) it is 9 K. For higher temperatures, the critical voltage starts to decrease rapidly until it fully vanishes significantly before  $T_c$  is reached. In general, we have observed no blockades above  $T_c$ . An example for the temperature dependence of a very small Coulomb blockade ( $V_c < 100 \mu\text{V}$ ) is provided in the discussion of the double wire circuits. The system shows qualitatively the same behavior but the blockade disappears already below 300 mK.

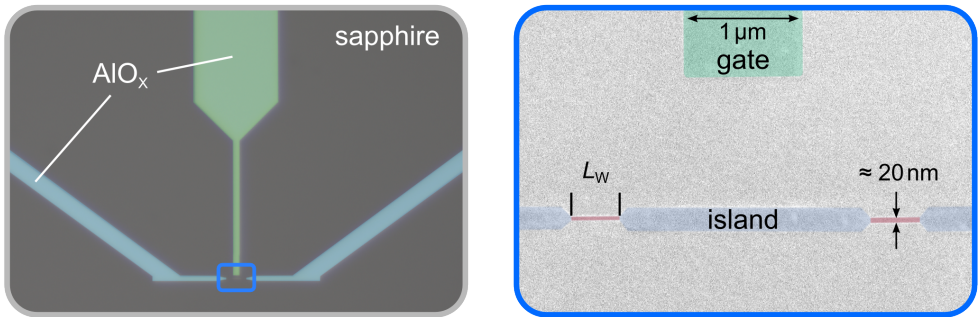


**Figure 6.13:** Optical (left) and electron micrograph (right) image of the double wire circuit. The device basically consists of two long high impedance on chip leads (colored in blue), two nanowires (colored in red), a charge island, and a gate electrode (colored in green). The whole structure is made from the same about 20 nm thick layer of granular aluminum and is placed on a sapphire substrate.

## 6.2 Double wire circuit experiments

In the previous section, quantum phase slips in single wires were extensively discussed. In this context, we have seen that the transport behavior can be well explained using the phase slip model, introduced in Refs. [Zai+97; GZ01; Moo+15]. Now we will explore the interference between phase slips, originating in two different wires. For this purpose, a quantum phase slip interferometer was developed in this work. The underlying idea for such a device and the principle of operation are explained in detail in Sec. 2.11.2. An interesting possibility that opens up with such a device is the investigation of the previously discussed superconductor to insulator phase transition by means of interference between QPS. The special feature here is that only the effective phase slip energy of the double-wire system is varied in a reversible manner. The inductive energy remains constant. Apart from its meaning for fundamental research, such a device is also interesting for various applications like transistors, detectors, or for serving as a tunable phase slip junction.

Experimentally, the exponential dependence of the phase slip energy  $E_s$  on  $R_n$  can be problematic. For the limit of strong interference, a very high degree of homogeneity is required. Therefore, even the natural resistance spread, expected for  $\text{AlO}_x$  nanowires [Bar+22], or small variations in geometry can highly suppress the possible interference. In previous experiments, this was confirmed to be one of the major limiting factors [APF21; HZ12]. To overcome this problem, we again use intrinsic electromigration (IEM), but this time for adjusting the normal state resistance  $R_n$  of two nanowires which are connected in series ( $R_n = R_{n1} + R_{n2}$ ).

Apart from a simple reduction of  $R_n$ , due to its character, this method also leads to increased homogeneity of the circuit (see Sec. 5.2). Following this approach, we can change the amplitude and ratio of the wires' phase slip energies  $E_{s1}$ ,  $E_{s2}$  and of the kinetic inductances  $L_{k1}$ ,  $L_{k2}$  with the IEM method.

Fig. 6.13 shows an optical (left) and a scanning electron microscope (right) image of a sample with two 500 nm long wires. The two high impedance input lines are colored in blue, two nanowires in red, the charge island and the gate electrode in green. The whole structure is made from a single layer of granular aluminum, using the double stack process (second process), presented in Sec. 3.3. For all samples, the sheet resistance is between 2 k $\Omega$  and 3 k $\Omega$ . A detailed description of the circuit layout and the chip design can be found in Sec. 4.2.2. A theoretical discussion of important design parameters is provided in Sec. 2.12.2. The measurements were performed at 25 mK (unless stated otherwise). The resistance reduction of  $R_n$  was carried out in the same way as for single wires, described in the previous section.

## 6.2.1 Gate dependent modulation of the critical voltage

To study the gate effect on the transport behavior of the double wire circuits, we measured the  $I - V$  characteristics as a function of the applied gate voltage  $V_g$ .

Fig. 6.14 (a) shows the dependency of the critical voltage on  $V_g$  for a sample with two 1000 nm long wires (A) after the resistance was reduced from  $R_n \approx 1\text{M}\Omega$  to  $R_n \approx 160\text{ k}\Omega$ . Exemplary  $I - V$  curves for the maximal ( $V_g = 0\text{ mV}$ , blue) and minimal ( $V_g = 49\text{ mV}$ , red) blockade can be found in Fig. 6.14 (b). The measurement time per trace was  $\sim 90\text{ s}$ . In the blockade, the current is below 2 pA and the transition to the conductive state is very sharp, allowing to precisely determine  $V_c$ .

The modulation of  $V_c$  is periodic, symmetric around zero gate voltage and has a sinusoidal shape. The overlaid curve is a fit to the effective threshold voltage for strongly different QPS amplitudes (e.g.  $V_{c1} \gg V_{c2}$ ), using Eq. 2.95. The extracted parameters are  $V_{c1} = 1.5\text{ mV}$ ,  $a = V_{c2}/V_{c1} = 0.22$  and  $C_g = 6.5\text{ aF}$ , assuming a periodicity of  $2e$ .

Using these values, the coupling parameter is  $\beta_s \approx 0.1$ , indicating that the modulation strength is rather limited by inhomogeneities than by a weak coupling of the wires. The blockades correspond to  $E_s(V_g)/E_L(R_n)$  ratios between 6.4 (maximal constructive interference,  $\Gamma_{\text{QPS}} \approx 138\text{ GHz}$ ) and 3.9 (maximal destructive interference,  $\Gamma_{\text{QPS}} \approx 90\text{ GHz}$ ). Thus, the device is operating deep in the phase slip regime ( $E_s \gg E_L$ ).

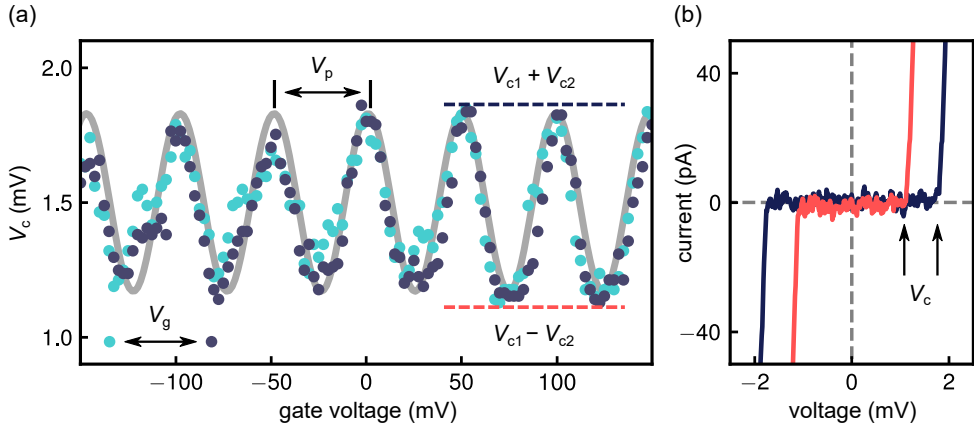


**Figure 6.14:** (a) Critical voltage  $V_c$  vs. gate voltage  $V_g$  for a sample with two  $1\ \mu\text{m}$  long wires (A). The solid line is a fit to the effective threshold voltage across the circuit, using Eq. 2.95 ( $V_{c1} = 1.5\text{ mV}$ ,  $C_g = 6.5\text{ aF}$ ,  $a = V_{c2}/V_{c1} = 0.22$ ).  $V_p = 49\text{ mV}$ . There is no hysteresis between the different scan directions (dark and bright dots). The maxima correspond to constructive interference, the minima to destructive interference (indicated with the dashed lines). (b)  $I - V$  curves for  $V_g = 0\text{ mV}$  (blue) and  $V_g = 49\text{ mV}$  (red).

## 6.2.2 Time stability of the Coulomb blockade

To investigate the time stability of  $V_c$ , we recorded the  $I - V$  characteristics of sample A at zero applied gate voltage and over a time span of four hours. Fig. 6.15 shows a histogram of the extracted critical voltages. The sampling time for the  $I - V$  curves was about  $0.04\text{ s}$  ( $\sim 90\text{ s}$  per trace) and the histogram contains 140 values (7 bins).

The blue curve in Fig. 6.15 is a fit to a Gaussian distribution from which we extract a median of  $V_c = 1.787\text{ mV}$  and a standard deviation of 1.3 percent. Thus, the system is very stable in time and  $V_c$  fluctuates on average about two percent around the gate period, presented in see Sec. 6.2.1. Fluctuations on much shorter time scales than the measurement time for a single trace will average out and are not visible in this measurement.

Generally, it can be added that the measured modulations were stable over days. We see no sudden jumps of the  $V_c$  value at constant gate voltage or in the  $I - V$  characteristics above  $V_c$ , as e.g. can be caused by single electron tunneling [Sch+00]. Many of the measurements, especially for devices with strongly pronounced Coulomb blockade, were performed over periods of several hours.

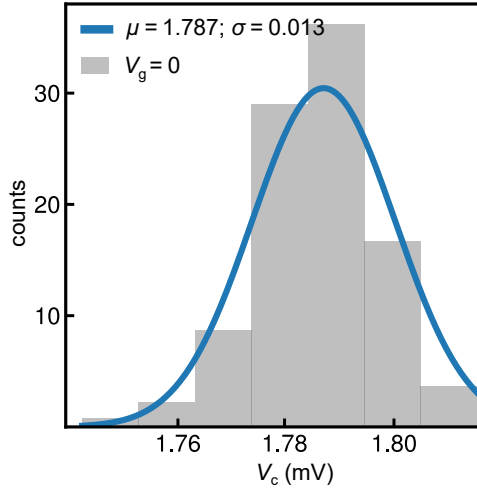


**Figure 6.15:** Distribution of critical voltages for sample A at zero applied gate voltage. The measurements are performed over a time span of four hours. The histogram contains 140 values. The blue curve shows a Gaussian distribution with a median of 1.787 mV and a standard deviation of 1.3 percent.

### 6.2.3 Temperature dependence of the critical voltage

For small critical voltages ( $V_c < 100 \mu\text{V}$ ), the Coulomb energy  $eV_c$  compares to a thermal energy of a few hundred mK only. Thus, already a small increase in temperature can cause a smoothing of the transition from the insulating to the conductive state (see Sec. 2.11.2). To investigate  $V_c(T)$  for the double wire circuits, we measured the  $I - V$  curves as a function of the temperature.

Fig 6.16 shows the temperature dependence of the extracted  $V_c$  resp.  $dV/dI$  values of a sample with two 500 nm long wires with a common normal state resistance of  $R_n \approx 63 \text{ k}\Omega$  at  $V_g = 0$ . At the base temperature of  $\approx 25 \text{ mK}$ , we measured  $V_c \approx 63 \mu\text{V}$ . For lowest temperatures we find a very low sensitivity of  $V_c$  regarding  $T$  (the same behavior as presented for single wires in Sec. 6.1.9). Close to  $T \approx 280 \text{ mK}$ , the blockade rapidly reduces. For higher temperatures the differential resistance around zero bias reduces with an increase in  $T$ .

The  $V_c(T)$  plateau at low temperatures indicates that even for very small blockades, the measured  $V_c$  values are not distorted by thermal effects. This conclusion gets supported by a relatively weak smoothing around  $V_c$ , even for samples with blockades below  $50 \mu\text{V}$  (see Sec. 6.2.7, Fig. 6.22 (b)).

For the modulation of  $V_c$  with the applied gate voltage, we see no smooth transition from  $2e$  to  $e$  periodicity when increasing the temperature (e.g. seen for Cooper pair

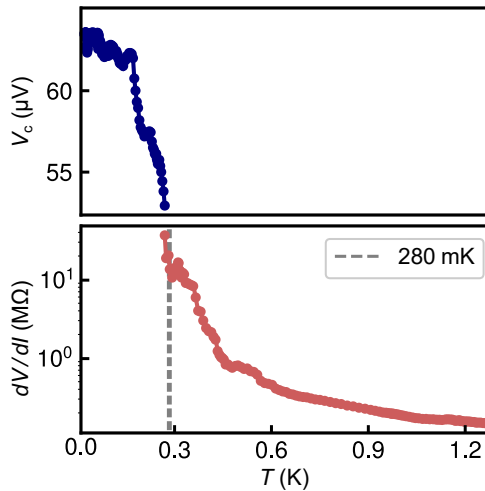


**Figure 6.16:** Temperature dependence of  $V_c$  (upper panel) and  $dV/dI$  around zero bias ( $I < 0.3$  nA) (lower panel) for a double wire circuit with two 500 nm wires ( $R_n \approx 63$  k $\Omega$ ). At  $T \approx 280$  mK, the blockade fully vanishes. For all samples,  $T_c \approx 1.8$  K.

transistors in Ref. [Joy95]) but a strong decrease of the modulation strength. A possible reason, why we don't see such a transition is the suppression of quasi particle poisoning due to the high impedance leads. However, the temperature dependence of the modulation was not studied in detail and needs further investigation.

## 6.2.4 Resistance dependence of the critical voltage and the gate modulation

In the following, we will discuss the effect of resistance changes in  $R_n$  on  $V_c$  and on the periodicity of  $V_c(V_g)$ .

Fig. 6.17 shows the  $I - V$  (a) curves and the extracted critical voltages as a function of the applied gate voltage (b) of a sample with two 500 nm long wires (B) for three different  $R_n$  values (300 k $\Omega$  (blue), 230 k $\Omega$  (red), 180 k $\Omega$  (green)). The dashed lines in Fig. 6.17 (b) are fits to Eq. 2.95 from which a common gate capacitance of  $C_g = 8.9$  aF is extracted. The modulation strength  $a$  increased from 0.12 ( $R_n \approx 300$  k $\Omega$ ) to 0.28 ( $R_n \approx 180$  k $\Omega$ ). An overview of all extracted parameters and associated values for the ratio between  $E_s$  and  $E_L$  is given in table 6.2.

The strong decrease of the maximum threshold voltage (from 5 mV to 1.5 mV) together with the reduction of  $R_n$  fits the expectations from the phase slip model,

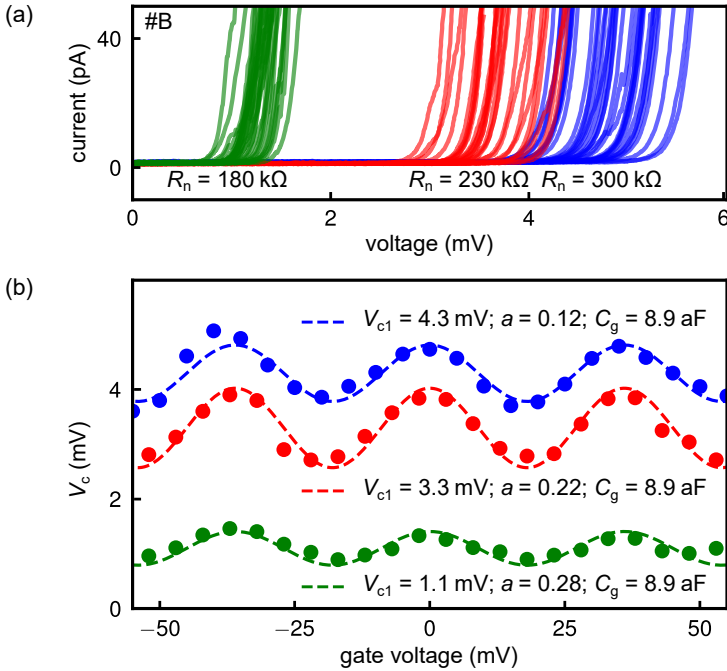


**Figure 6.17:** (a)  $I - V$  characteristics for sample with two 500 nm long wires (B) at different  $R_n$  values and at different applied gate voltages. The  $R_n$  values are 300 kΩ (blue), 230 kΩ (red), 180 kΩ (green). (b) Extracted critical voltages vs. gate voltage. The dashed lines show fits, using Eq. 2.95.

presented for various wire lengths in Sec. 2.12.2. As the modulation frequency remains the same for the different  $R_n$  values, the effective island size seems not to be affected by the resistance tuning with the IEM method. This observation provides a hint, that the charge island is well defined at the intended location in between the wires.

Apart from the technical advantages, resulting from the tunability, the possible large range of wire resistances also can help to distinguish the effect of the interference of QPS from other effects that could cause a gate dependent oscillation of a Coulomb blockade, e.g., Coulomb blockades due to single Josephson junctions (gate dependent electron tunneling) [CW94; Hav+91].

The increase in the modulation strength  $V_{c2}/V_{c1}$  (from 0.12 to 0.28) can be explained by an increased wire homogeneity of the resistance. Assuming that both wires have the same geometry, one can make a rough estimate (using Eq. 2.76) for the ratio of the single wire resistances at  $R_n = 180$  kΩ:  $R_{n2}/R_{n1} \approx 0.6$ . Here, we can already

**Table 6.2:** Extracted parameters for three different common wire resistances  $R_n$  (sample B):  $R_n$  is the common normal state resistance of both wires. The values for the critical voltages and gate capacitances are extracted from the fits, presented in Fig. 6.17 (b). The sheet resistance of the granular aluminum film used for the fabrication of this sample was measured with a larger test structure to be  $R_{\square} \approx 2.5 \text{ k}\Omega$ .

$R_n$	$V_{c,\min}$	$V_{c,\max}$	$C_g/dV_g$	$\frac{V_{c2}}{V_{c1}}$	$\frac{E_{s,\min}}{E_L}$	$\frac{E_{s,\max}}{E_L}$
300	3.5 mV	5 mV	8.9 aF / 36 mV	0.12	7	10
230	2.6 mV	3.9 mV	8.9 aF / 36 mV	0.22	5	8
180	0.9 mV	1.5 mV	8.9 aF / 36 mV	0.28	2	3

see the expected increased sensitivity to a difference in resistance for smaller  $R_n$  values, discussed in Sec. 2.12.2 (Fig. 2.20).

## 6.2.5 Resistance dependence of the two wire homogeneity

For virgin samples (not treated with IEM), we found strong Coulomb blockades of a few mV but only a weak reaction to the applied gate voltage. This changed dramatically after first gentle treatments with current pulses. This behavior can be explained by the increased homogeneity. Initially, very few weak junctions dominate the properties of the single wires, leading to large differences in phase slip amplitudes and inductances. By treating the samples with IEM pulses, these dominating junctions die more and more out (see also Sec. 5.2).

For the implemented configuration, only the sum of  $R_{ni}$  ( $R_n = R_{n1} + R_{n2}$ ) can be measured directly. The single wire resistances can only be determined indirectly from  $V_c(V_g)$  measurements after several gradual resistance changes of the same device. The common function  $V_c(R_{ni})$  can be derived by solving the equations

$$V_{c1} + V_{c2} = V_c(hR_n/(1+h)) + V_c(R_n/(1+h)) \quad (6.1)$$

for a set of  $R_n$  values numerically. Here, we have introduced the two wire homogeneity  $h = R_{n2}/R_{n1}$ .

Fig. 6.18 (a) shows the maximum expected threshold voltage for different wire lengths  $L_w$  vs. the common normal state resistance  $R_n$  together with a comparison to the measurements of a sample with two 300 nm long wires (D) (at zero gate voltage, see also Fig. 6.18 (c)). For the theory curves Eq. 2.76 is used and perfect symmetry for the wires is assumed ( $R_{n1} = R_{n2}$ ). The green dashed line marks the ratio  $E_s/E_L \approx 0.02$  at which the transition from insulating to metallic behavior was found for single wires in the previous section. The gate voltage dependencies after

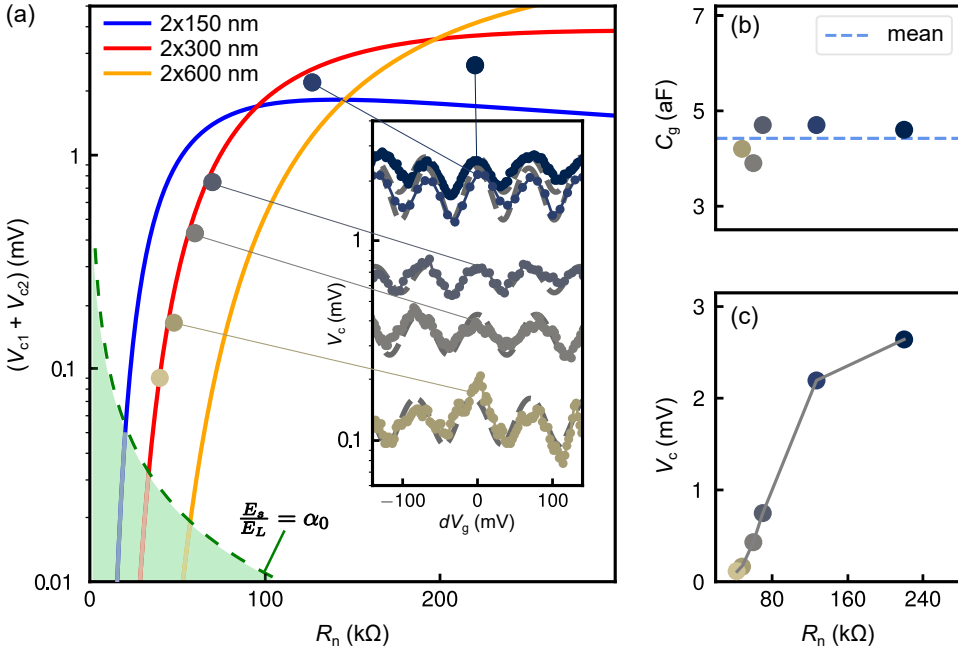


**Figure 6.18:** (a) Expected Coulomb blockade of two wires in series as a function of the common normal state resistance  $R_n$  (see also Fig. 2.19). The dots represent different iterations of sample D, with two 300 nm wires. The modulation with applied gate voltage is shown in the inset. For the smallest  $R_n$  value, the device switches between insulating and metallic regime (discussed separately in Sec. 6.2.7).  $E_s/E_L = \alpha_0 = 0.02$  marks the expected transition from the insulating to the metallic regime. (b) Gate capacitances vs.  $R_n$ , determined from the gate modulation with fits using Eq. 2.95. The mean value of  $C_g \approx 4.5$  aF is represented by the dashed line. (c) Critical voltage of the circuit at zero applied gate voltage vs.  $R_n$ .

each IEM run are presented in the inset. For all  $R_n$  values, the periodicity remains approximately the same ( $C_g \approx 4.5$  aF, see Fig. 6.18 (c)). For the smallest  $R_n$  value (41 k $\Omega$ ,  $V_c(V_g = 0) \approx 90$   $\mu$ V) a gate driven switching between an insulating and a conductive state is observed, which will be discussed separately.

These measurements provide a set of five equations (Eq. 6.1) for the determination of  $V_c(R_{ni})$ . Using Eq. 2.76 for  $V_c(R_{ni})$ , we find the common function for  $\alpha \approx 0.17$  and  $\beta \approx 0.59$ . This is in very good agreement with the previously found values from single wire measurements. Fig. 6.19 shows the single wire critical voltage as a function of the single wire resistance together with the determined function  $V_c(R_{ni})$  (blue solid line).  $V_{c1,2}$  is determined from fits to the gate modulation, the  $R_{ni}$  values are determined from the  $V_c(R_{ni})$  function. The modulation strength

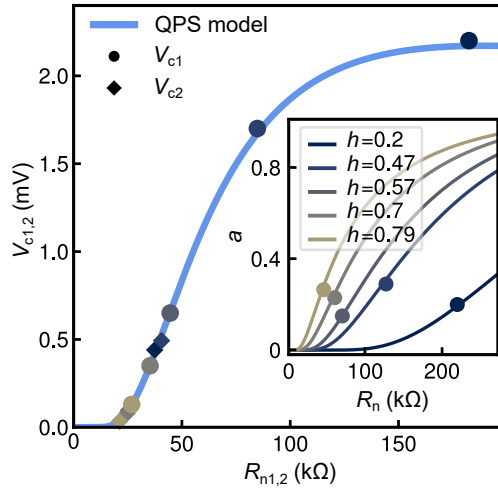


**Figure 6.19:** Critical voltages of the single wires as a function of the single wire resistance (sample D). The  $V_{ci}$  values are extracted from the modulation, the  $R_{ni}$  values are determined from the  $V_c(R_{ni})$  function ( $\alpha \approx 0.17$  and  $\beta \approx 0.59$ ). The inset shows the modulation strength  $a = V_{c2}/V_{c1}$  as a function of  $R_n$  for different homogeneities  $h = R_{n2}/R_{n1}$ . The dots are the measured values.

$a = V_{c2}/V_{c1}$  vs.  $R_n$  for the different homogeneities is presented in the inset. The dots represent the measured values from the modulation, presented in Fig. 6.18 (a).

From this analysis we find an increase of the double wire homogeneity from 0.2 to about 0.8 for a reduction of  $R_n$  from  $\approx 220$  kΩ to  $\approx 44$  kΩ. The corresponding mean value of the double wire sheet resistance at  $R_n \approx 44$  kΩ is  $\approx 1.5$  kΩ which is roughly 1 kΩ below the measured film sheet resistance (determined with large test structures). The large difference between the homogeneity and the modulation strength is explained by the enhanced sensitivity to wire inhomogeneities for small phase slip amplitudes (see Sec. 2.12.2). For the smallest  $R_n$  value of this device (41 kΩ), we estimate from the  $V_c(V_g)$  range in the insulating regime a  $h > 0.9$ .

## 6.2.6 Homogeneity of the two wire circuit in dependence of the current pulses

Fig. 6.20 displays the increase of the homogeneity from  $\approx 0.2$  up to  $\approx 0.9$  with the application of IEM pulses with amplitudes up to  $I_p = 82 \mu\text{A}$ , found for sample D. Initially, almost exclusively, the resistance of wire 1 is reduced. The evolution of the common wire resistance  $R_n$  with increasing current pulses is presented in

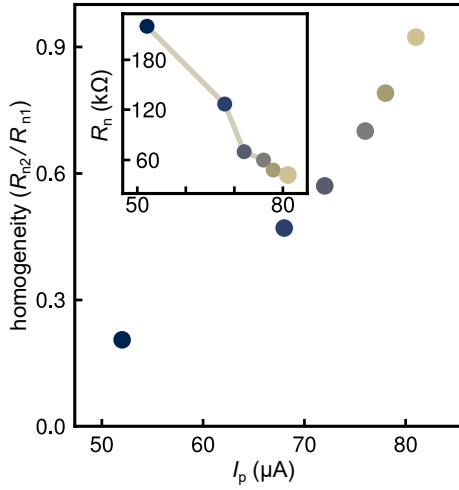


**Figure 6.20:** Homogeneity vs. amplitude of the IEM pulse  $I_p$  for sample D ( $2 \times 300$  nm wires). For increasing amplitudes, the single wire resistances more and more approach similar values. The inset shows the reduction of the common normal state resistance.

the inset. Prior to the application of any IEM pulses,  $R_n$  for this sample was above  $1 \text{ M}\Omega$  and no gate modulation was observed.

For the presented  $R_n(I_p)$  values, the decrease in resistance with increasing pulse amplitude is rather linear. For  $I_p$  values  $\ll 50 \mu\text{A}$  we observed the same rapid change as for single wires (presented in Sec. 6.1.1). For samples that were fabricated from the same granular aluminum film and shared the same wire length, we found similar values for  $R_n(I_p)$  for  $I_p > 70 \mu\text{A}$ , indicating a rather low device to device variation of the geometric shape of the wires.

In general, it can be said that a strong increase in homogeneity was observed in practically all samples measured. This also matches the observations made during test measurements on serial arrays, which allowed the single-wire resistance to be measured directly. Here, homogeneities of well over 90 percent are achieved. Interestingly, in some cases a saturation of homogeneity can be observed. Once this maximum value is reached, the resistances of both wires are uniformly reduced and the homogeneity oscillates around a constant value. Naturally, an upper bound is also given by the degree of equality of the geometric shapes.

## 6.2.7 Gate dependent transport transition from insulating to metallic

For a very high degree of homogeneity and/or small  $V_c(V_g = 0)$  values, we observe not only a modulation of the threshold voltage with  $V_g$ , but also a periodic switching to a conductive state. Below we discuss this gate driven transition from insulating to a metallic behavior and compare it with the resistance driven transition for single wires discussed in Sec. 6.1.7.

### Transition for a circuit with two 300 nm long wires

For the smallest resistance value of sample D ( $R_n = 41 \text{ k}\Omega$ ,  $V_c(V_g = 0) \approx 90 \text{ }\mu\text{V}$ ) a periodic switching between blockade and metallic-like behavior is observed. The gate dependent  $I - V$  characteristics are presented in Fig. 6.21 (a). The gray lines are fits to the resistive branch at larger bias values from which we extracted  $R_n$ . For comparison, the minimal differential resistance ( $\approx 1.5 \text{ M}\Omega$ ) in the metallic regime around zero bias ( $I < 30 \text{ pA}$ ) is added (red dashed line).  $I - V$  curves for insulating and metallic behavior at small bias values are shown in 6.21 (b). For the metallic state, instead of  $V_c$ , the slope around zero bias changes with  $V_g$ .

The smallest critical voltage before the switching to the metallic regime is  $\approx 30 \text{ }\mu\text{V}$  which corresponds to  $E_s/h \approx 2.3 \text{ GHz}$ . Thus, we find a transition ratio of  $E_s(V_{c,\min})/E_L(R_n) \approx 0.022$ , which agrees well with the transition ratio  $\alpha_0 \approx 0.02$ , found in the single wire experiments. This supports the expectation, that the two strongly coupled wires behave like a single wire with a gate tunable phase slip energy. This also explains the much higher  $R_n$  value, compared to the resistance of single wires with similar lengths (as both wires together) at the insulating to metallic transition (see table 6.1).

### Transition for a circuit with two 500 nm long wires

A more pronounced switching between insulating and metallic regime was found for a sample with two 500 nm long wires (C) and a common wire resistance of  $R_n \approx 56 \text{ k}\Omega$ .

Fig. 6.22 (b) shows  $I - V$  curves for the largest blockade ( $\approx 37 \text{ }\mu\text{V}$ , upper graph) and the smallest differential resistance ( $dV/dI \approx 40 \text{ k}\Omega$ , lower graph). Fig. 6.22 (a) presents the extracted gate dependent  $V_c(V_{c,\min})$  and  $dV/dI(V_g)$  values for a gate up (blue) and a gate down (red) sweep. The blockade range in the  $I - V$  curves is defined by the current noise in the blockade of  $\sim 8 \text{ pA}$ . Due to the rounding

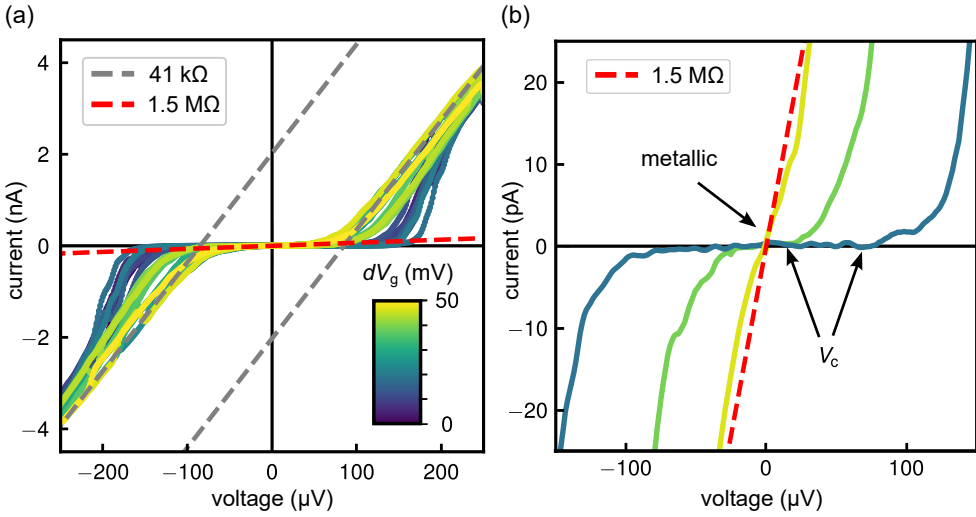


**Figure 6.21:** (a) Development of the  $I - V$  characteristics with  $V_g$  (sample C,  $R_n = 41 \text{ k}\Omega$ , see also Fig. 6.18 (a)). Darker lines correspond to smaller gate voltages, brighter to higher. At  $E_s/E_L \approx 0.02$  ( $dV_g \approx 35 \text{ mV}$ ,  $V_c \approx 30 \mu\text{V}$ ), the device switches to a conductive state. (b) Examples for insulating and metallic  $I - V$  curves at small bias values. The colors correspond to the colorbar from (a).

close to  $V = V_c$ , the error for the blockade values is relatively large. A possible explanation for the smoothing are finite temperature effects, which become more pronounced at such small blockades where the thermal energy is of the same order of magnitude as  $eV_c$  [EN21]. In both regimes, the change in  $V_c$  resp.  $dV/dI$  develops smoothly with the gate voltage.

From the modulation pattern in Fig. 6.22 (a), we find a peak to peak gate voltage of  $\sim 220 \text{ mV}$  and therefore, assuming a  $2e$  periodicity, a gate capacitance of  $C_g \approx 1.5 \text{ aF}$ . This value is significantly smaller than the values which were observed for other samples with similar geometry ( $\sim 4 \text{ aF}$  to  $5 \text{ aF}$ ). Thus, the deviation cannot be explained by simple fluctuations between individual fabrication runs. A possible explanation is an effect of the dynamic capacitances of the nanowires, which increase with  $1/V_c$  and for this sample are in the range of a few fF. Interestingly, there seem to be extreme deviations in the values for the maxima and minima. Simple explanations could be charge noise, which is more visible in these extreme regions, or a parity effect of the charge number on the island, similar as it has been seen in spectroscopy measurements in Ref. [Gra+18]. In the interference picture, a sudden switching between the two extremes is associated with a  $\pi$  phase jump caused by adding a charge of  $e$  onto the island.

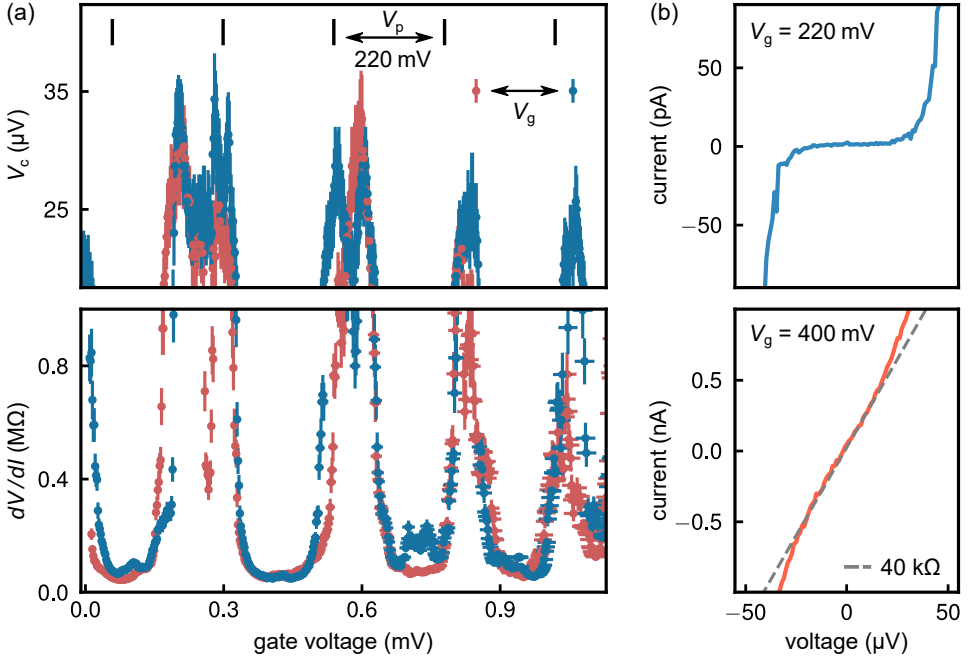


**Figure 6.22:** (a)  $V_c$  vs.  $V_g$  (upper panel) and  $dV/dI$  vs.  $V_g$  (lower panel). The values are extracted from the gate dependent  $I - V$  curves of sample C ( $2 \times 500$  nm wires,  $R_n \approx 56$  k $\Omega$ ). The device switches periodically ( $V_p \approx 220$  mV) between insulating and metallic behavior. (b) Exemplary  $I - V$  curves for both extremes. The upper panel shows a clear Coulomb blockade of  $V_c(V_g = 200$  mV)  $\approx 37$   $\mu$ V, the lower an  $I - V$  curve with a  $dV/dI \approx 40$  k $\Omega$  around zero bias.

With the smallest blockades being  $\approx 18$   $\mu$ V, the associated phase slip rate  $E_s/h$  is about 1.4 GHz (one GHz below the value for sample D) at the transition from the insulating to the metallic regime. Using  $R_n \approx 56$  k $\Omega$ , we find a transition ratio of  $E_s(V_{c,\min})/E_L(R_n) \approx 0.0185$ , which is in good agreement with the values found from sample D and in the single wire experiments. The observation that the switching to the conductive state appears at smaller  $V_c$  values, in comparison to sample D, agrees with the expectation that  $\alpha_0$  is shifted towards smaller blockades for longer wires (see Sec. 2.12.2).

## 6.2.8 Gate dependent transport transition from insulating to superconducting

The charge-induced transition can even be more extreme than the one from insulating to metallic, discussed above. Also a switching between an insulating state

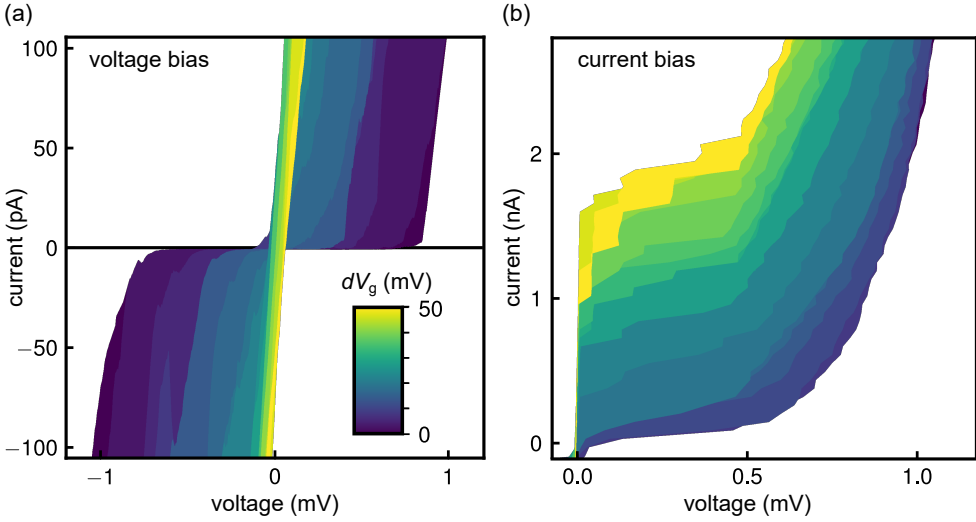


**Figure 6.23:** Raw data of the gate voltage dependent  $I - V$  characteristics for a sample with two 300 nm wires and  $R_n = 130 \text{ k}\Omega$  (E), measured with voltage bias scheme (a) and current bias scheme (b). The gate voltage range is half the period of the modulation, presented in Fig. 6.24 (a), and is the same for both measurements.

with critical voltages  $V_c(V_g)$  and a superconducting state with switching currents  $I_{SW}(V_g)$  can be observed.

Fig. 6.23 shows the gate dependent  $I - V$  characteristics for a sample with two 300 nm wires and  $R_n = 130 \text{ k}\Omega$  (E), measured with a voltage bias scheme (a) and a current bias scheme (b). The gate voltage range is the same for both measurements. It is half a period of the modulation frequency. From the  $I_V$  curves measured with voltage bias  $V_c(V_g)$  is determined (the current in the blockade is below 400 fA). The gate dependent critical currents  $I_{SW}(V_g)$  are extracted from the current bias measurements.

Fig. 6.24 (a) presents the extracted  $V_c(V_g)$  and  $I_{SW}$  values for a larger range of gate voltages. With peak values for  $V_c$  of about 0.5 mV and a corresponding phase slip rate of  $\Gamma_{QPS} \approx 50 \text{ GHz}$ , the device operates for constructive interference deep in the QPS regime. For destructive interference on the other hand, it switches at some point to the phase regime ( $E_s \ll E_L$ ), manifesting as switching currents with values up to 2 nA. Single traces for both extremes are shown on the right panels of Fig. 6.24 (b). For the superconducting regime, we have no good measure for the phase slip rate anymore and it is not clear what is limiting the maximal critical current. Nevertheless, for the sake of completeness, we can make the same comparison between the expected values from Ambeogaokar-Baratoff (AB)/Kulik-

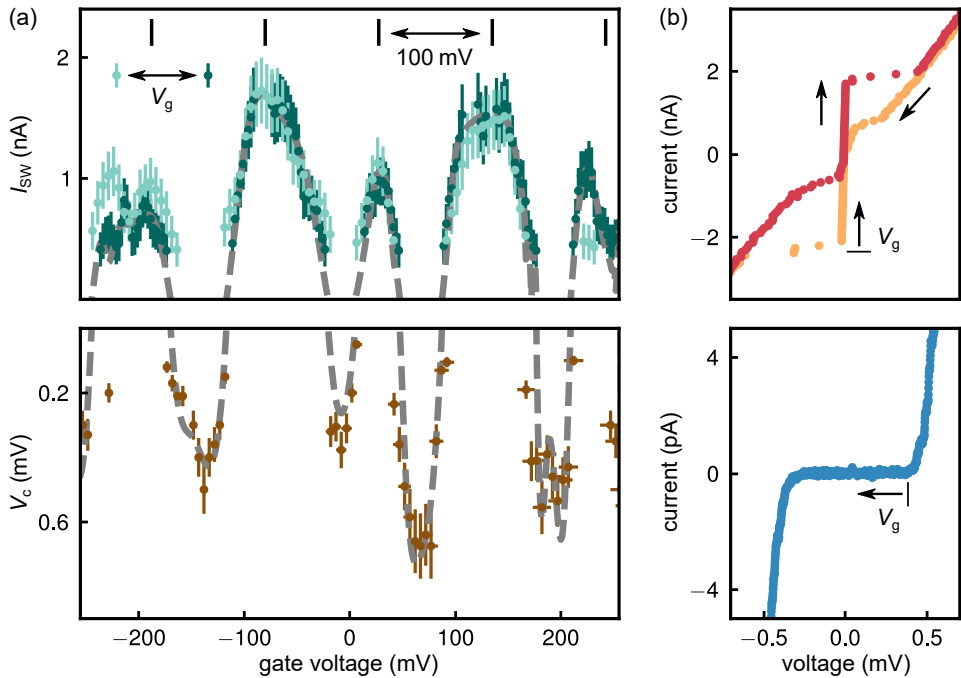


**Figure 6.24:** Gate induced periodic ( $V_p \approx 100$  mV) switching between insulating and supercurrent regime for sample E: (a) Shows how the switching current (upper) and critical voltage (lower) evolve with the the applied gate voltage. (b) Presents exemplary  $I - V$  curves for both regimes, measured in either a current bias scheme (supercurrent regime) or a voltage bias scheme (insulating regime).

Omel'yanchuk (KO1) relations and the maximum measured critical current, as it was done in the previous section for single wires. The values are 3 nA (AB) and 4.3 nA (KO1) which compare surprisingly well with the measured  $\approx 2$  nA.

The periodicity of  $V_p \approx 100$  mV compares well with the values from other samples sharing the same design. However, the shape of the modulation is rather different. A possible explanation for the discrepancy to the ordinary sinusoidal modulation is the formation of a parasitic charge island (e.g. by a cluster of strongly coupled grains), leading to a system where interference between more than two QPS junctions becomes relevant and thereby to a more complex interference pattern [Gra20; Pop+12]. However, expectable values for the coupling capacitance of such a parasitic island do not really fit with the modulation frequency since they are expected to be at least an order of magnitude smaller (when located in the nanowire). Another reason could be the existence of uncontrolled charged defects on the surface of the nanowires, leading to random phase offsets between different segments [Moo+15].

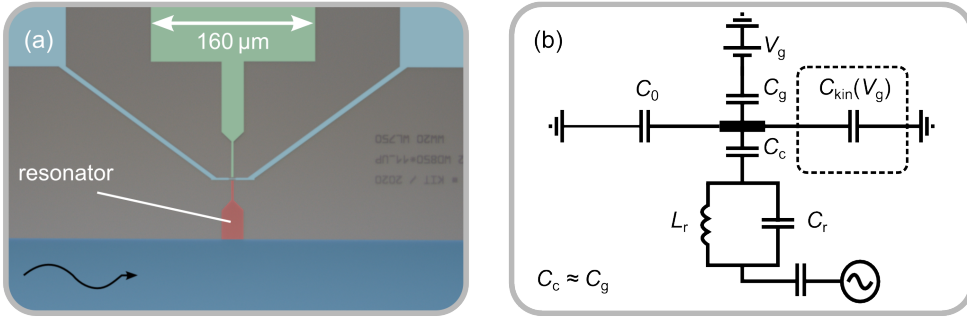


**Figure 6.25:** (a) Optical image of a double wire circuit with readout resonator. The resonator is colored in red, and the structure below is a microwave feedline (blue). The upper part is the same as for the devices discussed before. (b) Simplified circuit diagram:  $C_0$ ,  $C_c$  and  $C_g$  are the self-capacitance of the island, the resonator coupling capacitance and the gate capacitance. The common kinetic capacitance to ground across both wires is represented by  $C_{\text{kin}}(V_g)$ .  $C_r$  and  $L_r$  are the capacitance and the inductance of the resonator.

In summary, we observe not only a transition from insulating to metallic regime but also a transition from insulating to superconducting regime. We thus find the same regimes and transitions as previously described in the single wire experiments but now for much higher  $R_n$  values and driven by the interference of QPS. Also, the value for the ratio  $E_s/E_L$  ( $\approx 0.02$ ) at the transition point from insulating to metallic behavior seems to remain valid for the double-wire system. This is consistent with expectations that two strongly coupled wires should behave like a single one with a gate-dependent phase slip energy.

## 6.2.9 Resonator readout of the nanowire interference circuit

For some of the devices, a capacitively coupled  $\lambda/2$  readout resonator was added. The resonators are made from the same layer of granular aluminum as the rest of the device and typically have resonance frequencies between 6 GHz and 8 GHz. Fig. 6.25 (a) shows an optical image of a sample with a readout resonator. The upper part is analogous to the devices discussed before. The resonator is colored in red, the blue colored structure below is an aluminum microstrip feedline.

The principle of operation is as follows: If both wires are strongly coupled, and the leads are set to ground, the parallel kinetic capacitances to ground can be modeled as a common kinetic capacitance to ground  $C_{\text{kin}}(V_g)$ , which depends on the induced charge on the island. Therefore, the effective island capacitance to ground can be controlled by the gate voltage and the interference becomes visible

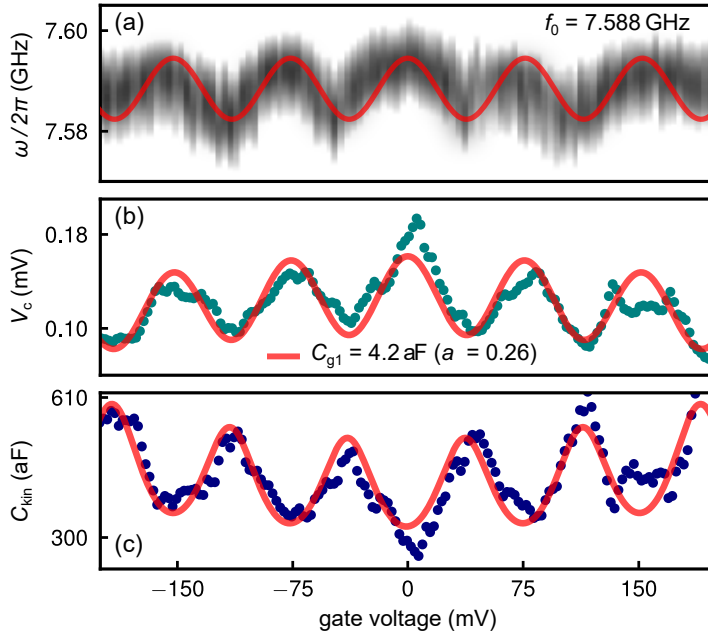


**Figure 6.26:** (a) Resonator frequency as a function of the applied gate voltage (leads set to ground). The modulation is around  $f_0 \approx 7.588$  GHz, periodic and has a span of  $\sim 12$  MHz. The red curve shows the modulation frequency found in the DC characterization. (b) Critical voltages as a function of  $V_g$ , extracted from the DC characterization of the same device. The red curve is a fit to Eq. 2.95 from which one finds  $C_{g1} \approx 4.2$  aF and  $a = V_{c2}/V_{c1} \approx 0.26$ . (c) Values for the kinetic capacitances ( $C_{\text{kin}} = e/(\pi V_c)$ ), associated with the  $V_c$  values from (b).

as a frequency shift of the capacitively coupled resonator. A simplified circuit diagram is presented in Fig. 6.25 (b).  $C_0$ ,  $C_g$  are the self-capacitance of the island and the gate capacitance.  $C_c$  is the coupling capacitance to the readout resonator, which is designed symmetrically to the DC gate coupling. Therefore, it can be assumed that  $C_c \approx C_g$ .  $L_r$  and  $C_r$  are the inductance and the capacitance of the resonator.

Fig. 6.26 (a) shows the modulation of the resonance frequency with the applied gate voltage for a sample with two 300 nm long wires ( $R_n \approx 50$  k $\Omega$ ). The modulation is periodic around  $f_0 \approx 7.588$  GHz and the maximal frequency shift is  $\approx 12$  MHz. The rather large linewidth is explained by the strong coupling to the feedline ( $Q_c \sim 200$ ). We also observed an increased gate and current noise for measurements with enabled low temperature HEMTs (high-electron-mobility transistors) amplifiers. This might be due to a ground issue and can explain the noise on the signal for RF measurements.

The  $V_c(V_g)$  values from the DC characterization for the same device at the same  $R_n$  value are presented in Fig. 6.26 (b). Here, the modulation of the critical voltages is between  $V_c \approx 90 \mu\text{V}$  (7 GHz) and  $V_c \approx 170 \mu\text{V}$  (13 GHz). The red curve is a fit, using Eq. 2.95. To account for a small parasitic modulation with much larger periodicity, an additional term is added ( $C_{g2} \approx 0.2 \text{ aF}$ ). Fig. 6.26 (c) gives the associated values for the kinetic capacitance ( $C_{\text{kin}} = 2e/(2\pi V_c)$ ). The kinetic capacitance varies between  $\sim 300 \text{ aF}$  and  $\sim 600 \text{ aF}$ . Using these values as a basis for simulations, we find a frequency range for the shift of the readout resonator between 10 MHz and 20 MHz, which is in good agreement with the measured modulation (see Sec. 4.2.2).

### Change from capacitive coupling to inductive coupling

If the resistance of the two nanowires  $R_n$  is reduced until one or both wires are in the superconducting regime, the common kinetic capacitance disappears. For this case, the two DC leads are connected to the island via the wire inductances and the capacitive coupling to ground turns into an inductive coupling. This change in coupling is illustrated in Fig. 6.27 (b) and (c). Here,  $Z_L$  are the lead impedances ( $\sim 8 \text{ k}\Omega$ ),  $L_{ki}$  are the kinetic inductances of the wires and  $C_{ki}$  are the kinetic capacitances of the wires.

Fig. 6.27 (a) shows the resonances of the readout resonator at  $R_n \approx 50 \text{ k}\Omega$  (blue,  $V_c \approx 170 \mu\text{V}$ ) and  $R_n \approx 14 \text{ k}\Omega$  (red,  $I_c \approx 80 \text{ nA}$ ). The dashed lines are Lorentzian fits from which we extract  $f_0 \approx 7.588 \text{ GHz}$  and  $f'_0 \approx 7.552 \text{ GHz}$ .

The change in resonance frequency is about 36 MHz and therefore three times higher than the previously observed gate modulation. This jump to a lower resonance frequency can be explained by the additional inductance, the resonator sees. The decrease in the depth of the resonance dip can have its reason in the stronger coupling to ground.

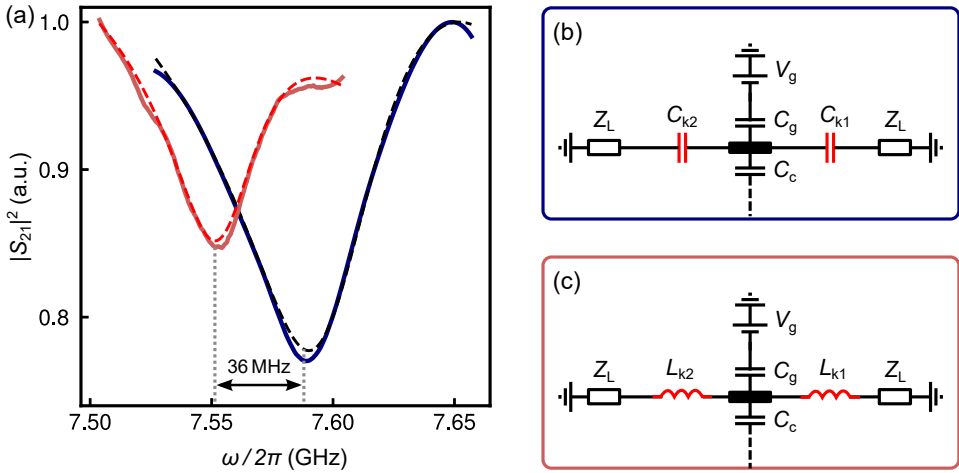


**Figure 6.27:** Frequency shift of the readout resonator: The blue curve shows the resonance dip at  $R_n \approx 50 \text{ k}\Omega$  ( $V_c \approx 170 \text{ }\mu\text{V}$ ), the red curve at  $R_n \approx 14 \text{ k}\Omega$  ( $I_c \approx 80 \text{ nA}$ ). Both curves are measured at  $V_g = 0$ . The dashed lines are Lorentzian fits to determine the resonance frequency. The right panels illustrate the different couplings to ground. If both wires are in the insulating regime, they have a kinetic capacitance  $C_{ki}$  (a). If the wires are in the superconducting regime,  $C_{ki}$  disappears and the coupling turns into an inductive one through the kinetic inductances  $L_{ki}$ .  $Z_L$  represent the on chip lead impedances.

## 6.2.10 Concluding remarks

Conclusively, we will discuss the parameter range, covered in the presented experiments, and summarize important findings.

Fig. 6.28 shows the  $V_g$  and  $R_n$  dependent  $E_s/E_L$  range for samples A to E. The different points for fixed parameters correspond to different  $V_g$  values. For samples that have shown a switching between insulating and metallic/superconducting regimes, only values in the insulating region are shown (for the other values, there is no measure for  $E_s$  anymore).

The range for  $E_s/E_L$  ratios is from 28 down to about 0.02, with critical voltages ranging from  $\approx 5 \text{ mV}$  down to  $\approx 18 \text{ }\mu\text{V}$ . Thus, we find the same lower limit for the  $E_s/E_L$  ratio as for single wires. Also the  $V_c(R_n)$  (at  $V_g = 0$ ) dependency agrees well with the results from single wire measurements.

The extracted gate capacitances are all in the same range and scale with the geometry (e.g. sample B has a larger island size, and the gate electrode is closer to the island, compared to sample D). The values are below the calculated values of a

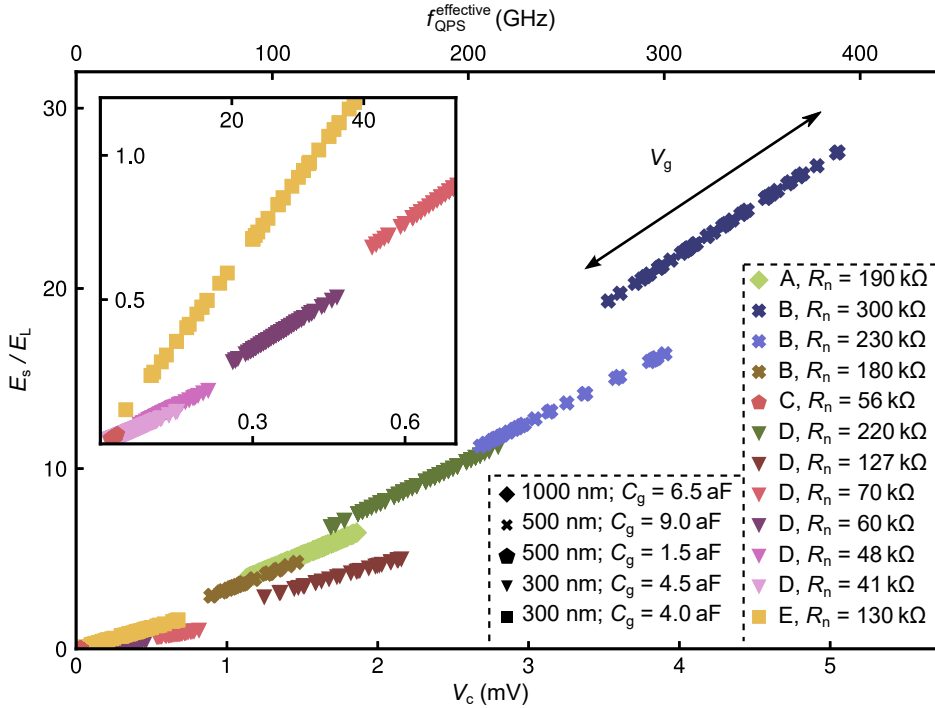


**Figure 6.28:** Operation range of samples A to E in the insulating regime. The critical voltage range is from  $\sim 5$  mV down to  $\sim 18 \mu\text{V}$  and the  $E_s/E_L$  ratios are between  $\approx 28$  and  $\approx 0.02$  ( $\alpha_0$ ). The upper x-axis provides the associated phase slip rates. The different points for each sample/iteration correspond to different applied gate voltages (the effective phase slip energy of the double-wire system is reduced reversely by interference, indicated by the double-sided arrow). The table in the inset provides the sample name (introduced during the discussion), the double wire resistance  $R_n$ , the wire length and the gate capacitance (extracted from the gate dependent  $V_c$  modulation).

few ten aF, but in accord with measured values for similar geometries (e.g. in Refs. [Kru+01; HZ12]). Thus we can conclude that the charge island seems to be well defined and is not significantly affected by the IEM tuning.

Fig. 6.29 shows the corresponding coupling parameter for all samples/iterations. Here the largest value is 0.5 and the smallest is about  $10^{-4}$  ( $C_0 \ll C_g$ ). Thus, most samples are operating deep in the strong coupling limit  $\beta_s \ll 1$ . For a single device,  $\beta_s$  can reduce by more than one order of magnitude when reducing  $R_n$  (e.g. for sample D from  $\beta_s \approx 0.12$  down to  $\beta_s \approx 0.004$ ).

Regarding the homogenization of the wires, we find that values of well above  $R_{n2}/R_{n1} = 0.9$  for a sufficient IEM treatment are possible for the wires investigated here. For small blockades ( $V_c < 100 \mu\text{V}$ ), the kinetic capacitances of the wires can

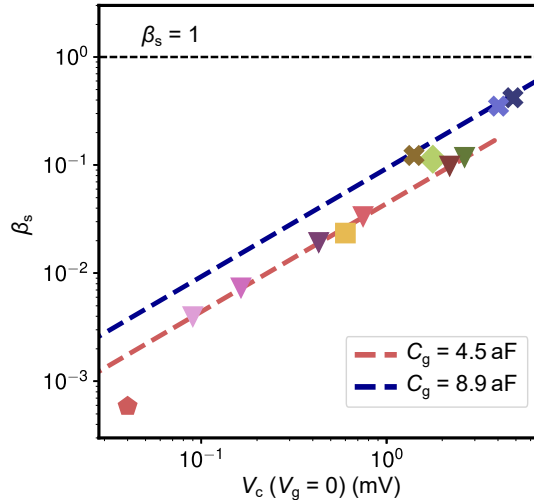


**Figure 6.29:** Coupling parameter  $\beta_s$  for samples A to E as a function of the critical voltage ( $V_g = 0$ ). For the calculation, the self-capacitance of the island is neglected. Different symbols and colors are related to the table in Fig. 6.28. The largest  $\beta_s$  is about 0.5, the smallest about  $10^{-4}$ . Most devices (iterations of devices) are operating deep in the strong coupling limit ( $\beta_s \ll 1$ ).

reach values well above fF, which is almost two orders of magnitude larger than what is achievable by typical Al/AlO<sub>x</sub>/Al junctions of the same diameters as that of the wires crosssections [Dep+04].

In general, we observe that it tends to be easier to observe switching between regimes for devices with shorter wires. For longer wires, on the other hand, smaller blockades can be achieved. This observation is consistent with the expectations from the phase diagram derived in the preceding section (see also Fig. 2.20).



## 7 Conclusion

In this work, we have investigated the phenomenon of quantum phase slips in superconducting nanowires, made from granular aluminum. For this purpose, in a first step, a new technique has been developed which allows for gradual resistance changes of the normal state resistance by orders of magnitude, at millikelvin temperatures, *in-situ*, and without changing the geometric shape of the wire. By the application of small current pulses, the wire's intrinsic network of Josephson junctions is modified, leading to a reduction in the normal state resistance. As a consequence, important properties in the superconducting state, such as the kinetic inductance or the fluctuation rate of the superconducting order parameter can be adjusted precisely and over a wide range. Due to its character, we named it intrinsic electromigration (IEM).

The new degree of freedom that has thereby been generated allowed us to probe and confirm the microscopic theory for quantum phase slips in the insulating regime, developed by Zaikin, Goulubev and Mooji (ZGM), for its applicability to the wires at hand [Vos+21]. Investigating the transport behavior for single wires over a large range of normal state resistances, we find an insulating to metallic and a metallic to superconducting (I-M-S) transition. In the insulating and superconducting regime, the normal state resistance defines the critical voltage resp. the critical current, while in the metallic regime it controls the nonlinear conductance around zero bias. To derive a phase diagram, we follow the approach from Mooij and co-workers in the spirit of the duality between quantum phase slip junctions and Josephson junctions and separate the regimes by certain ratios between phase slip energy and inductive energy. The shapes of the transition lines are thereby well defined from the comparison with the QPS model in the insulating regime. The resulting diagram is well consistent with results found for MoGe nanowires in Ref. [Moo+15] and NbTnN wires from Ref. [Mak+16], indicating a more general character.

In the second part of this work, we use the knowledge gained from the single wire experiments to develop a quantum phase slip interferometer. This allows us to probe the coherent character of quantum phase slips but also gives new access to the exploration of the I-M-S transition, observed for single wires.

Our experimental realization includes two long ( $L \gg \zeta_0$ ) nanowires, which are strongly coupled by a small charge island in between. The interference is controlled by a gate induced charge and caused by the Aharonov Casher effect. The serial arrangement of the wires allows to use the IEM method to adjust the energetic operating point of both wires simultaneously. This creates the possibility to study a large range of wire impedances for a single device. Apart from a simple reduction of the wire resistances, also the homogeneity of the circuit gets highly increased with this procedure, which is particularly important for the investigation of strong interference effects and the limit of small phase slip amplitudes.

In the insulating regime, where the effective phase slip energy of the double wire system is much larger than the inductive energy, the interference is visible as a periodic modulation of the critical Coulomb blockade voltage. For small blockades or a high degree of homogeneity, we observe a switching between insulating and metallic or even superconducting regimes. Thus, we find the same I-M-S transition as for single wires, but at much larger wire resistances. The observations are in well accord with the derived phase diagram, since here, in contrast to the single wire experiments, the effective phase slip energy of the system is reduced by interference of phase slips, and therefore in a reversible manner.

To investigate the kinetic capacitance of the wires more directly, we have developed a second circuit design, which includes an additional readout resonator, capacitively coupled to the charge island. Here, the gate induced charge defines the common kinetic capacitance of both wires to ground and the interference becomes visible as a frequency shift of the resonator.

# Bibliography

- [ACC66] B. Abeles, R. W. Cohen, and G. W. Cullen: *Enhancement of Superconductivity in Metal Films*. Phys. Rev. Lett. **17** (1966), pp. 632–634. doi: 10.1103/PhysRevLett.17.632 (cit. on p. 50).
- [AB59] Y. Aharonov and D. Bohm: *Significance of Electromagnetic Potentials in the Quantum Theory*. Phys. Rev. **115** (1959), pp. 485–491. doi: 10.1103/PhysRev.115.485 (cit. on p. 15).
- [AC84] Y. Aharonov and A. Casher: *Topological Quantum Effects for Neutral Particles*. Phys. Rev. Lett. **53** (1984), pp. 319–321. doi: 10.1103/PhysRevLett.53.319 (cit. on pp. 15, 16, 37).
- [AHB12] A. Allain, Z. Han, and V. Bouchiat: *Electrical Control of the Superconducting-to-Insulating Transition in Graphene–Metal Hybrids*. Nature Materials **11.7** (2012), pp. 590–594. doi: 10.1038/nmat3335 (cit. on p. 89).
- [Alt+06] F. Altomare, A. M. Chang, M. R. Melloch, Y. Hong, and C. W. Tu: *Evidence for Macroscopic Quantum Tunneling of Phase Slips in Long One-Dimensional Superconducting Al Wires*. Phys. Rev. Lett. **97** (2006), p. 017001. doi: 10.1103/PhysRevLett.97.017001 (cit. on pp. 1, 18).
- [AB63a] V. Ambegaokar and A. Baratoff: *Tunneling Between Superconductors*. Phys. Rev. Lett. **10** (1963), pp. 486–489. doi: 10.1103/PhysRevLett.10.486 (cit. on pp. 12, 69).
- [AB63b] V. Ambegaokar and A. Baratoff: *Tunneling Between Superconductors*. Phys. Rev. Lett. **11** (1963), pp. 104–104. doi: 10.1103/PhysRevLett.11.104 (cit. on pp. 12, 69).
- [AD64] P. W. Anderson and A. H. Dayem: *Radio-Frequency Effects in Superconducting Thin Film Bridges*. Phys. Rev. Lett. **13** (1964), pp. 195–197. doi: 10.1103/PhysRevLett.13.195 (cit. on p. 21).
- [AR63] P. W. Anderson and J. M. Rowell: *Probable Observation of the Josephson Superconducting Tunneling Effect*. Phys. Rev. Lett. **10** (1963), pp. 230–232. doi: 10.1103/PhysRevLett.10.230 (cit. on p. 10).

- [APF21] M. S. Anwar, J. A. Potter, and J. C. Fenton: *Gate-controlled conductance of superconducting NbN nanowires: coherent quantum phase-slip or Coulomb blockade?* *Superconductor Science and Technology* **34.11** (2021), p. 115018. DOI: 10.1088/1361-6668/ac2997 (cit. on pp. 45, 99).
- [AB11] T. Aref and A. Bezryadin: *Precise in Situ Tuning of the Critical Current of a Superconducting Nanowire Using High Bias Voltage Pulses.* *Nanotechnology* **22.39** (2011), p. 395302. DOI: 10.1088/0957-4484/22/39/395302 (cit. on p. 86).
- [AGZ08] K. Arutyunov, D. Golubev, and A. Zaikin: *Superconductivity in one dimension.* *Physics Reports* **464.1-2** (2008), pp. 1–70. DOI: 10.1016/j.physrep.2008.04.009 (cit. on pp. 1, 18, 24).
- [AL22] K. Y. Arutyunov and J. S. Lehtinen: *Arutyunov and Lehtinen Reply:* *Phys. Rev. Lett.* **128** (2022), p. 159702. DOI: 10.1103/PhysRevLett.128.159702 (cit. on p. 87).
- [Aru+12] K. Y. Arutyunov, T. T. Hongisto, J. S. Lehtinen, L. I. Leino, and A. L. Vasiliev: *Quantum phase slip phenomenon in ultra-narrow superconducting nanorings.* *Scientific Reports* **2.1** (2012), p. 293 (cit. on pp. 1, 49).
- [ALR16] K. Arutyunov, J. Lehtinen, and T. Rantala: *The quantum phase slip phenomenon in superconducting nanowires with high-impedance environment.* *Journal of Superconductivity and Novel Magnetism* **29.3** (2016), pp. 569–572. DOI: 10.1007/s10948-015-3298-9 (cit. on p. 65).
- [Ast+12] O. V. Astafiev, L. B. Ioffe, S. Kafanov, Y. A. Pashkin, K. Y. Arutyunov, D. Shahar, O. Cohen, and J. S. Tsai: *Coherent quantum phase slip.* *Nature* **484.7394** (2012), pp. 355–358. DOI: 10.1038/nature10930 (cit. on pp. 1, 49).
- [AR70] M. J. Attardo and R. Rosenberg: *Electromigration Damage in Aluminum Film Conductors.* *Journal of Applied Physics* **41.6** (1970), pp. 2381–2386. DOI: 10.1063/1.1659233 (cit. on p. 71).
- [Bac+15] N. Bachar, U. Pracht, E. Farber, M. Dressel, G. Deutscher, and M. Scheffler: *Signatures of Unconventional Superconductivity in Granular Aluminum.* *Journal of Low Temperature Physics* **179** (2015). DOI: 10.1007/s10909-014-1244-z (cit. on p. 52).
- [BCS57] J. Bardeen, L. Cooper, and J. Schrieffer: *Microscopic Theory of Superconductivity.* *Physical Review* **106.1** (1957), pp. 162–164 (cit. on pp. 5, 8).

- [BP82] A. Barone and G. Paterno: *The Physics of Superconductors: Introduction to Fundamentals and Applications*. John Wiley & Sons, Ltd, 1982. URL: <https://onlinelibrary.wiley.com/doi/abs/10.1002/352760278X.fmatter> (cit. on p. 11).
- [BAR21] T. C. BARTOLO: *Superconducting nanowires: the role of topology and morphology*. PhD thesis. RMIT University, 2021 (cit. on pp. 69, 70, 72, 73, 78).
- [Bar+22] T. Bartolo, J. S. Smith, Y. Schoen, J. N. Voss, M. Cyster, A. V. Ustinov, H. Rotzinger, and J. H. Cole: *Microscopic quantum point contact formation as the electromigration mechanism in granular superconductor nanowires*. *New Journal of Physics* (2022). URL: <http://iopscience.iop.org/article/10.1088/1367-2630/ac7a58> (cit. on pp. 69, 70, 72–74, 78, 99).
- [Bau+16] X. D. A. Baumans, D. Cerbu, O.-A. Adami, V. S. Zharinov, N. Verellen, G. Papari, J. E. Scheerder, G. Zhang, V. V. Moshchalkov, A. V. Silhanek, and J. Van de Vondel: *Thermal and quantum depletion of superconductivity in narrow junctions created by controlled electromigration*. *Nature Communications* **7.1** (2016), p. 10560. DOI: 10.1038/ncomms10560 (cit. on pp. 50, 72, 82, 84).
- [Bel+07] I. S. Beloborodov, A. V. Lopatin, V. M. Vinokur, and K. B. Efetov: *Granular electronic systems*. *Rev. Mod. Phys.* **79** (2007), pp. 469–518. DOI: 10.1103/RevModPhys.79.469 (cit. on p. 89).
- [BLT00] A. Bezryadin, C. N. Lau, and M. Tinkham: *Quantum suppression of superconductivity in ultrathin nanowires*. *Nature* **404**.6781 (2000), pp. 971–974. DOI: 10.1038/35010060 (cit. on pp. 1, 18, 49).
- [Bez12] A. Bezryadin: *Superconductivity in Nanowires*. Wiley-VCH Verlag GmbH & Co. KGaA, 2012 (cit. on pp. 1, 8, 23, 96).
- [Bla69] J. R. Black: *Electromigration—A brief survey and some recent results*. *IEEE Transactions on Electron Devices* **16.4** (1969), pp. 338–347. DOI: 10.1109/T-ED.1969.16754 (cit. on p. 71).
- [Bol+08] A. T. Bollinger, R. C. Dinsmore, A. Rogachev, and A. Bezryadin: *Determination of the Superconductor-Insulator Phase Diagram for One-Dimensional Wires*. *Phys. Rev. Lett.* **101** (2008), p. 227003. DOI: 10.1103/PhysRevLett.101.227003 (cit. on pp. 1, 32, 33, 90, 94).
- [BRB06] A. T. Bollinger, A. Rogachev, and A. Bezryadin: *Dichotomy in short superconducting nanowires: Thermal phase slippage vs. Coulomb blockade*. *Europhysics Letters (EPL)* **76.3** (2006), pp. 505–511. DOI: 10.1209/epl/i2006-10275-5 (cit. on p. 34).

- [Bos+06] S. Bose, P. Raychaudhuri, R. Banerjee, and P. Ayyub: *Upper critical field in nanostructured Nb: Competing effects of the reduction in density of states and the mean free path*. Phys. Rev. B **74** (2006), p. 224502. doi: 10.1103/PhysRevB.74.224502 (cit. on p. 86).
- [Bou+98] V. Bouchiat, D. Vion, P. Joyez, D. Esteve, and M. H. Devoret: *Quantum Coherence with a Single Cooper Pair*. Physica Scripta **T76.1** (1998), p. 165. doi: 10.1238/physica.topical.076a00165 (cit. on p. 28).
- [BGB04] H. P. Büchler, V. B. Geshkenbein, and G. Blatter: *Quantum Fluctuations in Thin Superconducting Wires of Finite Length*. Phys. Rev. Lett. **92** (2004), p. 067007. doi: 10.1103/PhysRevLett.92.067007 (cit. on p. 26).
- [BK12] W. Buckel and R. Kleiner: *Supraleitung*. Weinheim, Germany: Wiley-VCH Verlag GmbH & Co. KGaA, 2012, pp. 296–296. doi: 10.1002/9783527668670 (cit. on pp. 10, 35).
- [Bul84] S. Bulgadaev: *Phase diagram of a dissipative quantum system*. JETP Lett **39.6** (1984), pp. 264–267 (cit. on p. 90).
- [CM49] N. Cabrera and N. F. Mott: *Theory of the oxidation of metals*. Reports on Progress in Physics **12.1** (1949), pp. 163–184. doi: 10.1088/0034-4885/12/1/308 (cit. on p. 72).
- [Ced+15] K. Cedergren, S. Kafanov, J.-L. Smirr, J. H. Cole, and T. Duty: *Parity effect and single-electron injection for Josephson junction chains deep in the insulating state*. Phys. Rev. B **92** (2015), p. 104513. doi: 10.1103/PhysRevB.92.104513 (cit. on p. 89).
- [Ced+17] K. Cedergren, R. Ackroyd, S. Kafanov, N. Vogt, A. Shnirman, and T. Duty: *Insulating Josephson Junction Chains as Pinned Luttinger Liquids*. Phys. Rev. Lett. **119** (2017), p. 167701. doi: 10.1103/PhysRevLett.119.167701 (cit. on p. 89).
- [Cha82] S. Chakravarty: *Quantum Fluctuations in the Tunneling between Superconductors*. Phys. Rev. Lett. **49** (1982), pp. 681–684. doi: 10.1103/PhysRevLett.49.681 (cit. on p. 90).
- [CW94] V. Chandrasekhar and R. A. Webb: *Single electron charging effects in high-resistance In<sub>2</sub>O<sub>3</sub> wires*. Journal of Low Temperature Physics **97.1** (1994), pp. 9–54. doi: 10.1007/BF00752978 (cit. on p. 104).
- [Chu+01] S. M. Chudinov, G. Mancini, M. Minestrini, R. Natali, S. Stizza, and A. Bozhko: *Critical current in granular superconductor C-Si-W with peak-type re-entrant superconductivity*. Journal of Physics: Condensed Matter **14.2** (2001), pp. 193–209. doi: 10.1088/0953-8984/14/2/307 (cit. on p. 69).

- [CB04] J. Clarke and A. I. Braginski: *The SQUID handbook. Vol. 1, Fundamentals and technology of SQUIDs and SQUID systems*. Wiley-VCH, 2004 (cit. on p. 36).
- [CA68] R. W. Cohen and B. Abeles: *Superconductivity in Granular Aluminum Films*. *Phys. Rev.* **168** (1968), pp. 444–450. DOI: 10.1103/PhysRev.168.444 (cit. on pp. 50, 53).
- [Cyr73] M. Cyrot: *Ginzburg-Landau theory for superconductors*. *Reports on Progress in Physics* **36.2** (1973), pp. 103–158. DOI: 10.1088/0034-4885/36/2/001 (cit. on p. 7).
- [Del+12] C. Delacour, B. Pannetier, J.-C. Villegier, and V. Bouchiat: *Quantum and Thermal Phase Slips in Superconducting Niobium Nitride (NbN) Ultrathin Crystalline Nanowire: Application to Single Photon Detection*. *Nano Letters* **12.7** (2012), pp. 3501–3506. DOI: 10.1021/nl3010397 (cit. on pp. 25, 96).
- [Dep+04] F. Deppe, S. Saito, H. Tanaka, and H. Takayanagi: *Determination of the capacitance of nm scale Josephson junctions*. *Journal of Applied Physics* **95.5** (2004), pp. 2607–2613. DOI: 10.1063/1.1645673 (cit. on p. 119).
- [Deu+80] G. Deutscher, B. Bandyopadhyay, T. Chui, P. Lindefeld, W. L. McLean, and T. Worthington: *Transition to Localization in Granular Aluminum Films*. *Phys. Rev. Lett.* **44** (1980), pp. 1150–1153. DOI: 10.1103/PhysRevLett.44.1150 (cit. on p. 53).
- [DES80] G. Deutscher, O. Entin-Wohlman, and Y. Shapira: *Upper critical fields in granular superconductors*. *Phys. Rev. B* **22** (1980), pp. 4264–4270. DOI: 10.1103/PhysRevB.22.4264 (cit. on p. 52).
- [Deu+73] G. Deutscher, H. Fenichel, M. Gershenson, and E. GrÅÆnbaum: *Transition to Zero Dimensionality in Granular Aluminium Superconducting Films*. *Journal of Low Temperature Physics* **10.1/2** (1973) (cit. on p. 51).
- [Dua95] J.-M. Duan: *Quantum Decay of One-Dimensional Supercurrent: Role of Electromagnetic Field*. *Phys. Rev. Lett.* **74** (1995), pp. 5128–5131. DOI: 10.1103/PhysRevLett.74.5128 (cit. on p. 24).
- [EN21] J. Erdmanis and Y. Nazarov: *Synchronization of Bloch oscillations by gate voltage modulation*. (2021). DOI: 10.48550/ARXIV.2107.10565 (cit. on pp. 1, 42–44, 110).
- [FZ01] R. Fazio and H. van der Zant: *Quantum phase transitions and vortex dynamics in superconducting networks*. *Physics Reports* **355.4** (2001), pp. 235–334. DOI: [https://doi.org/10.1016/S0370-1573\(01\)00022-9](https://doi.org/10.1016/S0370-1573(01)00022-9) (cit. on p. 89).
- [Fey82] R. P. Feynman: *Simulating physics with computers*. *Int. J. Theor. Phys.* **21** (1982), pp. 467–488. DOI: 10.1007/BF02650179 (cit. on p. 10).

- [Fis14] M. V. Fistul: *Josephson phase diffusion in small Josephson junctions: a strongly nonlinear regime*. (2014). DOI: 10.48550/ARXIV.1405.1876 (cit. on p. 88).
- [GD10] V. F. Gantmakher and V. T. Dolgoplov: *Superconductor-insulator quantum phase transition*. (2010) (cit. on p. 89).
- [GL55] V. L. Ginzburg and L. D. Landau: *On the theory of superconductivity*. Zh. Eksp. Teor. Fiz. 20, 1064 (1950). English translation in: L. D. Landau, *Collected papers* (Oxford: Pergamon Press, 1965) p. 546 2.6 (1955), p. 546 (cit. on p. 6).
- [Gio94] N. Giodano: *Superconducting fluctuations in one dimension*. Physica B: Condensed Matter **203.3** (1994), pp. 460–466. DOI: [https://doi.org/10.1016/0921-4526\(94\)90097-3](https://doi.org/10.1016/0921-4526(94)90097-3) (cit. on pp. 18, 23).
- [Gio88] N. Giordano: *Evidence for Macroscopic Quantum Tunneling in One-Dimensional Superconductors*. Phys. Rev. Lett. **61** (1988), pp. 2137–2140. DOI: 10.1103/PhysRevLett.61.2137 (cit. on pp. 1, 18, 19).
- [GZ99] D. S. Golubev and A. D. Zaikin: *Golubev and Zaikin Reply*: Phys. Rev. Lett. **82** (1999), pp. 3191–3191. DOI: 10.1103/PhysRevLett.82.3191 (cit. on p. 21).
- [GZ01] D. S. Golubev and A. D. Zaikin: *Quantum tunneling of the order parameter in superconducting nanowires*. Phys. Rev. B **64** (2001), p. 014504. DOI: 10.1103/PhysRevB.64.014504 (cit. on pp. 18, 24, 81, 99).
- [GKI04] A. A. Golubov, M. Y. Kupriyanov, and E. Il'ichev: *The current-phase relation in Josephson junctions*. Rev. Mod. Phys. **76** (2004), pp. 411–469. DOI: 10.1103/RevModPhys.76.411 (cit. on p. 12).
- [Gra20] S. E. de Graaf: *Dual Fraunhofer interference and charge fluctuations in long quantum phase slip wires*. Phys. Rev. B **102** (2020), p. 144509. DOI: 10.1103/PhysRevB.102.144509 (cit. on p. 113).
- [Gra+18] S. E. de Graaf, S. T. Skacel, T. Hönigl-Decrinis, R. Shaikhaidarov, H. Rotzinger, S. Linzen, M. Ziegler, U. Hübner, H.-G. Meyer, V. Antonov, E. Il'ichev, A. V. Ustinov, A. Y. Tzalenchuk, and O. V. Astafiev: *Charge quantum interference device*. Nature Physics **14.6** (2018), pp. 590–594. DOI: 10.1038/s41567-018-0097-9 (cit. on pp. 1, 2, 38, 49, 110).
- [Grü+18] L. Grünhaupt, N. Maleeva, S. T. Skacel, M. Calvo, F. Levy-Bertrand, A. V. Ustinov, H. Rotzinger, A. Monfardini, G. Catelani, and I. M. Pop: *Loss Mechanisms and Quasiparticle Dynamics in Superconducting Microwave Resonators Made of Thin-Film Granular Aluminum*. Physical Review Letters **121.11** (2018), p. 117001. DOI: 10.1103/PhysRevLett.121.117001 (cit. on p. 51).

- [Grü+19] L. Grünhaupt, M. Spiecker, D. Gusenkova, N. Maleeva, S. T. Skacel, I. Takmakov, F. Valenti, P. Winkel, H. Rotzinger, W. Wernsdorfer, A. V. Ustinov, and I. M. Pop: *Granular aluminium as a superconducting material for high-impedance quantum circuits*. *Nature Materials* (2019). doi: 10.1038/s41563-019-0350-3 (cit. on p. 51).
- [Hav+91] D. B. Haviland, L. S. Kuzmin, P. Delsing, and T. Claeson: *Observation of the Coulomb Blockade of Cooper Pair Tunnelling in Single Josephson Junctions*. *Europhysics Letters (EPL)* **16.1** (1991), pp. 103–108. doi: 10.1209/0295-5075/16/1/018 (cit. on p. 104).
- [Hoh67] P. C. Hohenberg: *Existence of Long-Range Order in One and Two Dimensions*. *Phys. Rev.* **158** (1967), pp. 383–386. doi: 10.1103/PhysRev.158.383 (cit. on p. 17).
- [HZ12] T. T. Hongisto and A. B. Zorin: *Single-Charge Transistor Based on the Charge-Phase Duality of a Superconducting Nanowire Circuit*. *Phys. Rev. Lett.* **108** (2012), p. 097001. doi: 10.1103/PhysRevLett.108.097001 (cit. on pp. 1, 2, 39, 42, 43, 45, 86, 99, 118).
- [HN11] A. M. Hriscu and Y. V. Nazarov: *Coulomb blockade due to quantum phase slips illustrated with devices*. *Phys. Rev. B* **83** (2011), p. 174511. doi: 10.1103/PhysRevB.83.174511 (cit. on p. 1).
- [Ian+89] M. Iansiti, M. Tinkham, A. T. Johnson, W. F. Smith, and C. J. Lobb: *Charging effects and quantum properties of small superconducting tunnel junctions*. *Phys. Rev. B* **39** (1989), pp. 6465–6484. doi: 10.1103/PhysRevB.39.6465 (cit. on p. 88).
- [Jak+64] R. C. Jaklevic, J. Lambe, A. H. Silver, and J. E. Mercereau: *Quantum Interference Effects in Josephson Tunneling*. *Phys. Rev. Lett.* **12** (1964), pp. 159–160. doi: 10.1103/PhysRevLett.12.159 (cit. on p. 2).
- [Jos62] B. D. Josephson: *Possible new effects in superconductive tunnelling*. *Physics Letters* **1** (1962), pp. 251–253. doi: 10.1016/0031-9163(62)91369-0 (cit. on p. 10).
- [Joy95] P. Joyez: *The single Cooper pair transistor: a macroscopic quantum system*. Theses. Université Pierre et Marie Curie - Paris VI, 1995. URL: <https://tel.archives-ouvertes.fr/tel-00534358> (cit. on p. 103).
- [KKS19] A. Kapitulnik, S. A. Kivelson, and B. Spivak: *Colloquium: Anomalous metals: Failed superconductors*. *Rev. Mod. Phys.* **91** (2019), p. 011002. doi: 10.1103/RevModPhys.91.011002 (cit. on p. 89).
- [Kat95] S. Katsumoto: *Single-electron tunneling and phase transitions in granular films*. *Journal of Low Temperature Physics* **98.5** (1995), pp. 287–349. doi: 10.1007/BF00752273 (cit. on p. 89).

- [Kat+06] N. Katz, M. Ansmann, R. C. Bialczak, E. Lucero, R. McDermott, M. Neeley, M. Steffen, E. M. Weig, A. N. Cleland, M. M. John, and A. N. Korotkov: *Coherent State Evolution in a Superconducting Qubit from Partial-Collapse Measurement*. *Science* **312**.5779 (2006), pp. 1498–1500. DOI: 10.1126/science.1126475 (cit. on p. 90).
- [Kim+18] H. Kim, F. Gay, A. Del Maestro, B. Sacépé, and A. Rogachev: *Pair-breaking quantum phase transition in superconducting nanowires*. *Nature Physics* **14** (2018), pp. 912–917. DOI: 10.1038/s41567-018-0179-8 (cit. on p. 82).
- [KR16] H. Kim and A. Rogachev: *Zero-bias anomaly in homogeneously disordered MoGe nanowires undergoing a superconductor-insulator transition*. *Phys. Rev. B* **94** (2016), p. 245436. DOI: 10.1103/PhysRevB.94.245436 (cit. on p. 66).
- [Kov+10] Y. Koval, X. Jin, C. Bergmann, Y. Simsek, L. Özyüzer, P. Müller, H. Wang, G. Behr, and B. Büchner: *Tuning superconductivity by carrier injection*. *Applied Physics Letters* **96**.8 (2010), p. 082507. DOI: 10.1063/1.3327825 (cit. on p. 82).
- [Kru+01] V. A. Krupenin, A. B. Zorin, M. N. Savvateev, D. E. Presnov, and J. Niemeyer: *Single-electron transistor with metallic microstrips instead of tunnel junctions*. *Journal of Applied Physics* **90**.5 (2001), pp. 2411–2415. DOI: 10.1063/1.1389758 (cit. on p. 118).
- [Kun+87] M. Kunchur, P. Lindenfeld, W. L. McLean, and J. S. Brooks: *Absence of superconductivity in metallic granular aluminum*. *Phys. Rev. Lett.* **59** (1987), pp. 1232–1235. DOI: 10.1103/PhysRevLett.59.1232 (cit. on p. 53).
- [Lan37] L. D. Landau: *On the theory of phase transitions*. *Zh. Eksp. Teor. Fiz.* **7** (1937), pp. 19–32 (cit. on p. 6).
- [LA67] J. S. Langer and V. Ambegaokar: *Intrinsic Resistive Transition in Narrow Superconducting Channels*. *Phys. Rev.* **164** (1967), pp. 498–510. DOI: 10.1103/PhysRev.164.498 (cit. on pp. 18, 20).
- [Lau+01] C. N. Lau, N. Markovic, M. Bockrath, A. Bezryadin, and M. Tinkham: *Quantum Phase Slips in Superconducting Nanowires*. *Phys. Rev. Lett.* **87** (2001), p. 217003. DOI: 10.1103/PhysRevLett.87.217003 (cit. on pp. 1, 18).
- [Leh+12] J. S. Lehtinen, T. Sajavaara, K. Y. Arutyunov, M. Y. Presnjakov, and A. L. Vasiliev: *Evidence of quantum phase slip effect in titanium nanowires*. *Phys. Rev. B* **85** (2012), p. 094508. DOI: 10.1103/PhysRevB.85.094508 (cit. on p. 50).

- [Lik86] K. K. Likharev: *Introduction to superconductivity, Second Edition*. GORDON and BREACH SCIENCE PUBLISHERS, 1986 (cit. on pp. 37, 40).
- [Lit67] W. A. Little: *Decay of Persistent Currents in Small Superconductors*. Phys. Rev. **156** (1967), pp. 396–403. DOI: 10.1103/PhysRev.156.396 (cit. on pp. 17, 19).
- [LL35] F. London and H. London: *The Electromagnetic Equations of the Superconductor*. Royal Society of London Proceedings Series A **149** (1935), pp. 71–88 (cit. on p. 5).
- [MT11] D. S. Macintyre and S. Thoms: *Comparison of hydrogen silsesquioxane development methods for sub-10 nm electron beam lithography using accurate linewidth inspection*. Journal of Vacuum Science & Technology B, Nanotechnology and Microelectronics: Materials, Processing, Measurement, and Phenomena **29.6** (2011), 06F307. DOI: 10.1116/1.3634020 (cit. on p. 55).
- [Mak+16] K. Makise, H. Terai, Y. Tominari, S. Tanaka, and B. Shinozaki: *Duality picture of Superconductor-insulator transitions on Superconducting nanowire*. Scientific Reports **6.1** (2016), p. 27001. DOI: 10.1038/srep27001 (cit. on pp. 1, 32, 34, 95, 97, 121).
- [Mal+18] N. Maleeva, L. Grünhaupt, T. Klein, F. Levy-Bertrand, O. Dupre, M. Calvo, F. Valenti, P. Winkel, F. Friedrich, W. Wernsdorfer, A. V. Ustinov, H. Rotzinger, A. Monfardini, M. V. Fistul, and I. M. Pop: *Circuit quantum electrodynamics of granular aluminum resonators*. Nature Communications **9.1** (2018), p. 3889. DOI: 10.1038/s41467-018-06386-9 (cit. on p. 51).
- [MB58] D. C. Mattis and J. Bardeen: *Theory of the Anomalous Skin Effect in Normal and Superconducting Metals*. Phys. Rev. **111** (1958), pp. 412–417. DOI: 10.1103/PhysRev.111.412 (cit. on p. 14).
- [Mau18] P. D. Maukopf: *Transition Edge Sensors and Kinetic Inductance Detectors in Astronomical Instruments*. Publications of the Astronomical Society of the Pacific **130.990** (2018), p. 082001. DOI: 10.1088/1538-3873/aabaf0 (cit. on p. 14).
- [Max50] E. Maxwell: *Isotope Effect in the Superconductivity of Mercury*. Phys. Rev. **78** (1950), pp. 477–477. DOI: 10.1103/PhysRev.78.477 (cit. on p. 8).
- [McC68] D. E. McCumber: *Effect of ac Impedance on dc Voltage-Current Characteristics of Superconductor Weak-Link Junctions*. Journal of Applied Physics **39.7** (1968), pp. 3113–3118. DOI: 10.1063/1.1656743 (cit. on pp. 29, 30).
- [MH70] D. E. McCumber and B. I. Halperin: *Time Scale of Intrinsic Resistive Fluctuations in Thin Superconducting Wires*. Phys. Rev. B **1** (1970), pp. 1054–1070. DOI: 10.1103/PhysRevB.1.1054 (cit. on pp. 18, 20).

- [MOR07] D. Meidan, Y. Oreg, and G. Refael: *Sharp Superconductor-Insulator Transition in Short Wires*. Phys. Rev. Lett. **98** (2007), p. 187001. doi: 10.1103/PhysRevLett.98.187001 (cit. on p. 32).
- [Mei+11] D. Meidan, B. Rosenow, Y. Oreg, and G. Refael: *Gapless Excitations in Strongly Fluctuating Superconducting Wires*. Phys. Rev. Lett. **107** (2011), p. 227004. doi: 10.1103/PhysRevLett.107.227004 (cit. on p. 96).
- [MO33] W. Meissner and R. Ochsenfeld: *Ein neuer Effekt bei Eintritt der Supraleitfähigkeit*. Naturwissenschaften **21.44** (1933), pp. 787–788 (cit. on p. 5).
- [MN06] J. E. Mooij and Y. V. Nazarov: *Superconducting nanowires as quantum phase-slip junctions*. Nature Physics **2.3** (2006), pp. 169–172. doi: 10.1038/nphys234 (cit. on pp. 1, 18, 26, 28–30, 33, 38, 42, 82, 88).
- [Moo+15] J. E. Mooij, G. Schön, A. Shnirman, T. Fuse, C. J. P. M. Harmans, H. Rotzinger, and A. H. Verbruggen: *Superconductor–insulator transition in nanowires and nanowire arrays*. New Journal of Physics **17.3** (2015), p. 033006. doi: 10.1088/1367-2630/17/3/033006 (cit. on pp. 1, 2, 25, 31–33, 45, 81, 82, 87, 93–95, 99, 113, 121).
- [MH05] J. E. Mooij and C. J. P. M. Harmans: *Phase-slip flux qubits*. New Journal of Physics **7** (2005), p. 219 (cit. on p. 28).
- [MS85] J. E. Mooij and G. Schön: *Propagating plasma mode in thin superconducting filaments*. Phys. Rev. Lett. **55** (1985), pp. 114–117. doi: 10.1103/PhysRevLett.55.114 (cit. on p. 24).
- [Naz99] Y. V. Nazarov: *Coulomb Blockade without Tunnel Junctions*. Phys. Rev. Lett. **82** (1999), pp. 1245–1248. doi: 10.1103/PhysRevLett.82.1245 (cit. on p. 34).
- [Onn11] H. K. Onnes: *The resistance of pure mercury at helium temperatures*. Commun. Phys. Lab. Univ. Leiden **12** (1911), 120pp. (Cit. on pp. 1, 5).
- [Pop+12] I. M. Pop, B. Douçot, L. Ioffe, I. Protopopov, F. Lecocq, I. Matei, O. Buisson, and W. Guichard: *Experimental demonstration of Aharonov-Casher interference in a Josephson junction circuit*. Phys. Rev. B **85** (2012), p. 094503. doi: 10.1103/PhysRevB.85.094503 (cit. on p. 113).
- [RS20] A. Rogachev and B. Sacépé: *Deficiency of the scaling collapse as an indicator of a superconductor-insulator quantum phase transition*. Phys. Rev. B **101** (2020), p. 235164. doi: 10.1103/PhysRevB.101.235164 (cit. on p. 96).
- [Rom+13] M. Rommel, B. E. W. Nilsson, P. Jedrasik, V. Bonanni, A. Dmitriev, and J. Weis: *Sub-10nm resolution after lift-off using HSQ/PMMA double layer resist*. 2013 (cit. on p. 55).

- [Rot+16] H. Rotzinger, S. T. Skacel, M. Pfirrmann, J. N. Voss, J. Münzberg, S. Probst, P. Bushev, M. P. Weides, A. V. Ustinov, and J. E. Mooij: *Aluminium-oxide wires for superconducting high kinetic inductance circuits*. *Superconductor Science and Technology* **30.2** (2016), p. 025002. doi: 10.1088/0953-2048/30/2/025002 (cit. on pp. 51–54).
- [SFK20] B. Sacépé, M. Feigel'man, and T. M. Klapwijk: *Quantum breakdown of superconductivity in low-dimensional materials*. *Nature Physics* **16.7** (2020), pp. 734–746. doi: 10.1038/s41567-020-0905-x (cit. on p. 1).
- [Sch83] A. Schmid: *Diffusion and Localization in a Dissipative Quantum System*. *Phys. Rev. Lett.* **51** (1983), pp. 1506–1509. doi: 10.1103/PhysRevLett.51.1506 (cit. on p. 90).
- [Sch+97] V. Schmidt, V. Müller, V. Schmidt, P. Müller, I. Grigorieva, and A. Ustinov: *The Physics of Superconductors: Introduction to Fundamentals and Applications*. Springer, 1997. URL: [https://books.google.de/books?id=808svNo%5C\\_tWoC](https://books.google.de/books?id=808svNo%5C_tWoC) (cit. on pp. 6, 8, 13).
- [Sch+00] V. Schöllmann, J. Johansson, K. Andersson, and D. B. Haviland: *Coulomb blockade effects in anodically oxidized titanium wires*. *Journal of Applied Physics* **88.11** (2000), pp. 6549–6553. doi: 10.1063/1.1323522 (cit. on p. 101).
- [Sch21] Y. Schön: *Superconducting Nanowires in Coherent Quantum Circuits*. PhD thesis. Karlsruhe Institut für Technologie (KIT), 2021. 117 pp. doi: 10.5445/IR/1000130597 (cit. on pp. 54–56, 92).
- [Sch+20] Y. Schön, J. N. Voss, M. Wildermuth, A. Schneider, S. T. Skacel, M. P. Weides, J. H. Cole, H. Rotzinger, and A. V. Ustinov: *Rabi oscillations in a superconducting nanowire circuit*. *npj Quantum Materials* **5.1** (2020), p. 18. doi: 10.1038/s41535-020-0220-x (cit. on pp. 51, 92).
- [SA92] R. Smith and V. Ambegaokar: *Weak-localization correction to the number density of superconducting electrons*. *Physical review. B, Condensed matter* **45** (1992), pp. 2463–2473. doi: 10.1103/PhysRevB.45.2463 (cit. on p. 86).
- [Són+19] D. Sónora, C. Carballeira, J. J. Ponte, F. Vidal, T. Grenet, and J. Mosqueira: *Paraconductivity of granular Al films at high reduced temperatures and magnetic fields*. *Phys. Rev. B* **100** (2019), p. 104509. doi: 10.1103/PhysRevB.100.104509 (cit. on p. 52).
- [Ste68] W. C. Stewart: *CURRENT-VOLTAGE CHARACTERISTICS OF JOSEPHSON JUNCTIONS*. *Applied Physics Letters* **12.8** (1968), pp. 277–280. doi: 10.1063/1.1651991 (cit. on p. 29).

- [Tin04] M. Tinkham: *Introduction to Superconductivity*. 2nd ed. Dover Publications, 2004. URL: <http://www.worldcat.org/isbn/0486435032> (cit. on pp. 9, 13, 14, 52).
- [TA08] S. K. Tolpygo and D. Amparo: *Electrical stress effect on Josephson tunneling through ultrathin AlOx barrier in Nb/Al/AlOx/Nb junctions*. *Journal of Applied Physics* **104.6** (2008), p. 063904. DOI: 10.1063/1.2977725 (cit. on pp. 71–73).
- [Val+19] F. Valenti, F. Henriques, G. Catelani, N. Maleeva, L. Gruenhaupt, U. von LUEpke, S. T. Skacel, P. Winkel, A. Bilmes, A. V. Ustinov, J. Goupy, M. Calvo, A. Benoit, F. Levy-Bertrand, A. Monfardini, and I. M. Pop: *Interplay Between Kinetic Inductance, Nonlinearity, and Quasiparticle Dynamics in Granular Aluminum Microwave Kinetic Inductance Detectors*. *Phys. Rev. Applied* **11** (2019), p. 054087. DOI: 10.1103/PhysRevApplied.11.054087 (cit. on p. 51).
- [VCS16] N. Vogt, J. H. Cole, and A. Shnirman: *De-pinning of disordered bosonic chains*. *New Journal of Physics* **18.5** (2016), p. 053026. DOI: 10.1088/1367-2630/18/5/053026 (cit. on p. 89).
- [Vog+15] N. Vogt, R. Schäfer, H. Rotzinger, W. Cui, A. Fiebig, A. Shnirman, and A. V. Ustinov: *One-dimensional Josephson junction arrays: Lifting the Coulomb blockade by depinning*. *Phys. Rev. B* **92** (2015), p. 045435. DOI: 10.1103/PhysRevB.92.045435 (cit. on p. 89).
- [Vos17] J. N. Voss: “Nonlinear effects in superconducting granular aluminium oxide nanowires”. Master Thesis. 2017 (cit. on p. 53).
- [Vos19] J. N. Voss: “Patent pending: No. 102019106508.9”. German patent office. 2019 (cit. on p. 83).
- [Vos+21] J. N. Voss, Y. Schön, M. Wildermuth, D. Dorer, J. H. Cole, H. Rotzinger, and A. V. Ustinov: *Eliminating Quantum Phase Slips in Superconducting Nanowires*. *ACS Nano* **15.3** (2021). PMID: 33596045, pp. 4108–4114. DOI: 10.1021/acsnano.0c08721 (cit. on pp. 3, 42, 45, 52, 72, 74–76, 81, 84, 87, 88, 90, 92–94, 121).
- [Was+85] S. Washburn, R. A. Webb, R. F. Voss, and S. M. Faris: *Effects of Dissipation and Temperature on Macroscopic Quantum Tunneling*. *Phys. Rev. Lett.* **54** (1985), pp. 2712–2715. DOI: 10.1103/PhysRevLett.54.2712 (cit. on p. 22).

- [Web+13] C. H. Webster, J. C. Fenton, T. T. Hongisto, S. P. Giblin, A. B. Zorin, and P. A. Warburton: *NbSi nanowire quantum phase-slip circuits: dc supercurrent blockade, microwave measurements, and thermal analysis*. Phys. Rev. B **87** (2013), p. 144510. doi: 10.1103/PhysRevB.87.144510 (cit. on pp. 18, 49, 65, 98).
- [WHH66] N. R. Werthamer, E. Helfand, and P. C. Hohenberg: *Temperature and Purity Dependence of the Superconducting Critical Field,  $H_{c2}$ . III. Electron Spin and Spin-Orbit Effects*. Phys. Rev. **147** (1966), pp. 295–302. doi: 10.1103/PhysRev.147.295 (cit. on p. 52).
- [Wil22] M. Wildermuth: *Quantum tunneling of Josephson vortices in high-impedance long junctions*. PhD thesis. Karlsruher Institut für Technologie (KIT), 2022. 117 pp. doi: 10.5445/IR/1000130597 (cit. on p. 61).
- [Wil+22] M. Wildermuth, L. Powalla, J. N. Voss, Y. Schön, A. Schneider, M. V. Fistul, H. Rotzinger, and A. V. Ustinov: *Fluxons in high-impedance long Josephson junctions*. Applied Physics Letters **120**.11 (2022), p. 112601. doi: 10.1063/5.0082197 (cit. on p. 54).
- [Zai+97] A. D. Zaikin, D. S. Golubev, A. van Otterlo, and G. T. Zimányi: *Quantum Phase Slips and Transport in Ultrathin Superconducting Wires*. Phys. Rev. Lett. **78** (1997), pp. 1552–1555. doi: 10.1103/PhysRevLett.78.1552 (cit. on pp. 18, 23, 24, 81, 96, 99).
- [Zgi+08] M. Zgirski, K.-P. Riikonen, V. Touboltsev, P. Jalkanen, T. T. Hongisto, and K. Y. Arutyunov: *Ion beam shaping and downsizing of nanostructures*. Nanotechnology **19**.5 (2008), p. 055301. doi: 10.1088/0957-4484/19/05/055301 (cit. on p. 50).
- [Zgi+05] M. Zgirski, K.-P. Riikonen, V. Touboltsev, and K. Arutyunov: *Size Dependent Breakdown of Superconductivity in Ultranarrow Nanowires*. Nano Letters **5**.6 (2005), pp. 1029–1033. doi: 10.1021/nl1050321e (cit. on p. 18).



# List of publications

- [Bar+20] C. Barone, H. Rotzinger, **J. N. Voss**, C. Mauro, Y. Schön, A. Ustinov, and S. Pagano: *Current-Resistance Effects Inducing Nonlinear Fluctuation Mechanisms in Granular Aluminum Oxide Nanowires*. *Nanomaterials* **10** (2020), p. 524. DOI: 10.3390/nano10030524.
- [Bar+22] T. Bartolo, J. S. Smith, Y. Schoen, **J. N. Voss**, M. Cyster, A. V. Ustinov, H. Rotzinger, and J. H. Cole: *Microscopic quantum point contact formation as the electromigration mechanism in granular superconductor nanowires*. *New Journal of Physics* (2022). URL: <http://iopscience.iop.org/article/10.1088/1367-2630/ac7a58>.
- [Gol+19] I. Golovchanskiy, N. Abramov, M. Pfirrmann, T. Piskor, **J. N. Voss**, D. Baranov, R. Hovhannisyan, V. Stolyarov, C. Dubs, A. Golubov, V. Ryazanov, A. Ustinov, and M. Weides: *Interplay of Magnetization Dynamics with a Microwave Waveguide at Cryogenic Temperatures*. *Physical Review Applied* **11** (2019). DOI: 10.1103/PhysRevApplied.11.044076.
- [Rot+16] H. Rotzinger, S. T. Skacel, M. Pfirrmann, **J. N. Voss**, J. Münzberg, S. Probst, P. Bushev, M. P. Weides, A. V. Ustinov, and J. E. Mooij: *Aluminium-oxide wires for superconducting high kinetic inductance circuits*. *Superconductor Science and Technology* **30.2** (2016), p. 025002. DOI: 10.1088/0953-2048/30/2/025002.
- [Sch+20] Y. Schön, **J. N. Voss**, M. Wildermuth, A. Schneider, S. T. Skacel, M. P. Weides, J. H. Cole, H. Rotzinger, and A. V. Ustinov: *Rabi oscillations in a superconducting nanowire circuit*. *npj Quantum Materials* **5.1** (2020), p. 18. DOI: 10.1038/s41535-020-0220-x.
- [Vos+21] **J. N. Voss**, Y. Schön, M. Wildermuth, D. Dorer, J. H. Cole, H. Rotzinger, and A. V. Ustinov: *Eliminating Quantum Phase Slips in Superconducting Nanowires*. *ACS Nano* **15.3** (2021). PMID: 33596045, pp. 4108–4114. DOI: 10.1021/acsnano.0c08721.
- [Wil+22] M. Wildermuth, L. Powalla, **J. N. Voss**, Y. Schön, A. Schneider, M. V. Fistul, H. Rotzinger, and A. V. Ustinov: *Fluxons in high-impedance long Josephson junctions*. *Applied Physics Letters* **120.11** (2022), p. 112601. DOI: 10.1063/5.0082197.



# Appendix

## A Fabrication parameters

**Table 1: Resist application (first process)**  $v_r$  is the ramp speed,  $t_r$  is the ramp time,  $a$  is the acceleration of the spin coater,  $v_s$  is the maximum rotation speed,  $t_s$  is the time (at rotation),  $T_B$  is the bake temperature,  $t_B$  is the bake time.

resist	$a$ (rpm/s)	$v_r$ (rpm)	$t_r$ (s)	$v_s$ (rpm)	$t_s$ (s)	$T_B$ ( $^{\circ}\text{C}$ )	$t_B$ (s)
HSQ	7500	300	4	3500	60	150	120
PMMA	7500	300	10	4000	60	160	240
S1805	4500	500	5	4500	60	115	60
S1818	4500	-	-	4500	60	80	300

**Table 2: e-beam resist exposure (first process)** The resist was applied  $\sim 30$  min before the chip was installed in the 50 keV JEOL JBX-5500ZD electron-beam writer.

resist	base dose	base dose ( $\mu\text{C}/\text{cm}^2$ )	wire dose multiplier
HSQ		900	11

**Table 3: optical resist exposure (first process)**

resist	process	intensity ( $\text{mW}/\text{cm}^2$ )	duration (s)
S1805	positive	13	4

**Table 4: e-beam resist development (first process)**

resist	developer	duration (s)	stopbath
HSQ	MIF 726	60	water
S1805	MF 319	32	water

**Table 5: Etching (first process)**

system	p (mTorr)	gasses (sccm)	rf power (W)	ICP power (W)	time (s)
ICP	-	Ar/O <sub>x</sub> (15/15)	100	200	9
ICP	-	Ar/Cl (2/12)	100	200	80

**Table 6: Resist application (second process)**  $v_r$  is the ramp speed,  $t_r$  is the ramp time,  $a$  is the acceleration of the spin coater,  $v_s$  is the maximum rotation speed,  $t_s$  is the time (at rotation),  $T_B$  is the bake temperature,  $t_B$  is the bake time.

resist	$a$ (rpm/s)	$v_r$ (rpm)	$t_r$ (s)	$v_s$ (rpm)	$t_s$ (s)	$T_B$ (°C)	$t_B$ (s)
HSQ	7500	300	4	2000	60	150	120
AZ5214E	7500	500	5	6000	60	110	50
S1818	4500	-	-	4500	60	80	300

**Table 7: e-beam resist exposure (second process)** The resist was applied  $\sim 30$  min before the chip was installed in the 50 keV JEOL JBX-5500ZD electron-beam writer.

resist	base dose ( $\mu\text{C}/\text{cm}^2$ )	wire dose multiplier
HSQ	850	11

**Table 8: Optical resist exposure (second process)** The UV light wavelength is 365 nm at a lamp power of 500 W.

resist	process	intensity ( $\text{mW}/\text{cm}^2$ )	duration (s)
AZ5214E	positive	13	5

**Table 9: Optical resist development (second process)**

resist	developer	duration (s)	stopbath
AZ5214E	AZ Developer (+H <sub>2</sub> O 1:1)	33	water

**Table 10: e-beam resist development (second process)**

resist	developer	duration (s)	stopbath
HSQ	MIF 726	65	water
AZ5214E	AZ Developer (+H <sub>2</sub> O 1:1)	33	water

**Table 11: Etching (second process)**

system	p (mTorr)	gasses (sccm)	rf power (W)	ICP power (W)	time (s)
ICP	10	Ar/CL (2/12)	100	200	50
RIE	15	CF <sub>4</sub> (15)	40	-	4x15

# Acknowledgements

First of all, I would like to thank Prof. Dr. Alexey Ustinov for trusting me to do this work under his guidance in his wonderful research group. Throughout the whole time, I have always experienced a high level of scientific freedom, support and feedback. In addition, he allowed me to participate in numerous conferences, through which I was able to gain many valuable experiences and broaden my scientific horizon.

I am grateful to and thank Prof. Dr. Alexander Shnirman for taking the time to discuss experimental results with me and for agreeing to be the second reviewer of my PhD thesis.

Very special thanks go to Dr. Hannes Rotzinger with whom I had the pleasure to start my scientific journey with the bachelor thesis and who accompanied and supported me all the way through to the PhD degree. With you, I always found an open ear for problems, questions and ideas as well as an inspiring high degree of enthusiasm for physical questions and experiments. I will always remember the many wonderful moments in- and outside the lab. Thank you for everything!

Big thanks also go to Dr. Jürgen Lisenfeld, Dr. Gerda Fischer and Dr. Sascha Lukashenko who were important constants in the group and who always took the time to address any kind of concern and to share their expertise.

In most cases, scientific success is the result of teamwork. During my PhD studies, I was fortunate to work with great colleagues who not only supported me in my work, but also made this time very special for me.

In particular, I would like to take this opportunity to thank Micha Wildermuth who not only defended his PhD thesis on the same day as me but was also a great companion throughout the entire time. I will always remember the countless hours we spent in the lab and the many - sometimes more, sometimes less - scientific discussions and conversations. The exchange with you has always been very enriching and helpful for me!

Many thanks also to Maximilian Kristen with whom I had the pleasure of sharing an office and who always managed to lighten the mood with his positive manner,

even when not everything went according to plan. Many thanks also for your high level of helpfulness and support with the fabrication of the samples!

My thanks also go to Andre Schneider, with whom I always had a lot of fun during and after work. Without you and your commitment, there would certainly not have been such a good atmosphere within the working group. Accordingly, I can only agree with those colleagues who described you as the good soul of the group.

I also want to thank Yannick Schön who accompanied me at the beginning of my work in the first steps towards nanowire experiments. Especially at the beginning, we both had to practice frustration tolerance, and for me it was very uplifting to have someone with whom I could share my joys and sorrows.

Many thanks to my former office colleagues Tim Wolz, Alex Stehli and Jan Brehm for the great time, the unforgettable moments and their very special sense of humour.

I would also like to thank Sebastian Skacel, Steffen Schlör, Marco Pfirmann, Patrick Winkel, Alexander Bilmes and Jochen Braumüller for the many interesting and special discussions, the great time we had during our low temperature seminars and for all the fun evenings!

Big thanks also go to the following generation of PhD students, Andrés Di Giovanni, Alex Kreuzer, Hossam Tohamy, Konstantin Händel and Benedikt Berlitz for their constant helpfulness and many fun conversations.

I would also like to thank Lucas Radtke and Dr. Silvia Diewald for the great support in fabricating the samples and their constant willingness to discuss problems and share their expertise.

Many thanks also to all of the other current and former scientific employees of the institute who have contributed to creating such a positive and constructive working environment in which one can only be grateful to be allowed to work.

Extraordinary thanks also go to the institute secretariat with Steffi Baatz and Claudia Alaya who always find a solution to various problems and save the scientists a lot of paperwork.

Furthermore, I would like to thank the employees of the precision mechanics workshop and the electrical workshop. No matter if it was about sample holders, cables, other parts or questions, they always tried to implement ideas if possible or to help with problems!

I would also like to take the opportunity to thank the Helmholtz International Research School for Teratronics for their financial support.

Last but not least, I want to express my gratitude to my family, especially my parents and my sister. You have always supported me in everything and believed in me. In doing so, you have helped me develop personally and become who I am today. Thank you for accompanying me also on this scientific journey and for always having my back.

Karlsruhe, July 2022

M. Sc. Jan Nicolas Voss



